Synthetic Aperture Radar Tomography
Compressed Sensing Models and Algorithms

vorgelegt von
Dipl.-Ing.
Esteban Aguilera
aus Mendoza

von der Fakultät IV – Elektrotechnik und Informatik
der Technische Universität Berlin (TU Berlin)
zur Erlangung des akademischen Grades
Doktor-Ingenieurs (Dr.-Ing.)

genehmigte Dissertation

Promotionsausschuss:

Vorsitzender:	Prof. Dr.-Ing. Alexa
Gutachter:	Prof. Dr.-Ing. Hellwich
	Prof. Dr. Lombardini
	Prof. Dr. Tebaldini
	Priv.-Doz. Dr.-Ing. Reigber

Tag der wissenschaftlichen Aussprache: 26. September 2014

Berlin 2014

Abstract

A synthetic aperture radar (SAR) is an active microwave instrument capable of imaging the surface of the earth at specific wavelengths and polarizations in day/night and all-weather conditions. In its basic configuration, a small airborne/spaceborne antenna traveling along a straight-line trajectory is pointed perpendicular to the flight track in a side-looking fashion. This results in the synthesis of a virtual along-track antenna aperture that enables the formation of a high-resolution 2-D image of the illuminated area. Moreover, when multiple parallel trajectories—with cross-track and/or elevation displacements—are considered, the resulting sensing geometry enables the synthesis of two virtual antenna apertures that allow for 3-D backscatter profiling. This imaging modality is known as SAR tomography and is commonly approached by first obtaining multiple 2-D coregistered SAR images—such that each image corresponds with a parallel pass—followed by 1-D standard spectral estimation techniques. A typical application is the 3-D imaging of vegetated areas which, due to the high-penetration capabilities of radiation at long wavelengths, has proven to be of great value for the estimation of forest structure and, in turn, for the quantification of above ground biomass. In addition, with the anticipated advent of long-wavelength spaceborne radars, tomographic SAR techniques will become of considerable interest, as tomographic data sets will be available on a large scale. However, ideal sampling conditions are known to require a large number of dense regular acquisitions, which are not only limited and expensive but can also lead to temporal decorrelation.

This dissertation explores the possibility of reducing the number of passes required for 3-D SAR imaging of forested areas by formulating the problem in a sparsity-driven framework usually referred to as compressed sensing (CS). To this end, the aforementioned 1-D spectral estimation step—which basically yields a vertical backscatter profile—will be regarded as the process of singling out a solution to an underdetermined linear system. In this regard, the criterion will be based on choosing a backscat-

ter profile such that it can be sparsely represented in an alternative domain. In particular, the use of a wavelet basis will prove to be a suitable choice. The method will be formulated for both single-channel and polarimetric sensors and will be shown to be robust to nonideal acquisitions as well as to be able to ensure physical validity. Also, these sparsity-based techniques will be evaluated as a function of sensor-to-target distance, required *a priori* knowledge, and computation time. Furthermore, a convex optimization approach to separation of forest scattering mechanisms will be introduced. In essence, the method aims to pre-filter tomographic data sets so that canopy and ground contributions can be separately reconstructed. Finally, a thorough validation will be provided by using polarimetric L- and P-band data acquired by the Experimental SAR (E-SAR) sensor of the German Aerospace Center (DLR).

Zusammenfassung

Ein Radar mit synthetischer Apertur (SAR) ist ein aktiver Sensor, der es ermöglicht die Erdoberfläche in unterschiedlichen Wellenlängen und Polarisationen unabhängig von Helligkeits- und Wetterverhältnissen abzubilden. In der Basiskonfiguration ist eine kleine Radarantenne senkrecht zu der—idealisiert gesehen—geraden Flugtrajektorie der zugrundeliegenden Plattform montiert. Diese kann entweder ein Satellit oder ein Flugzeug sein und ist so um die Rollachse geneigt, dass das Radar seitlich auf das zu vermessende Areal blickt. Durch die wiederholte Datenaufnahme in Flugrichtung (engl. "along track") wird eine Along-Track-Apertur synthetisiert, wodurch sich hochaufgelöste 2-D Bilder generieren lassen. Liegen darüber hinaus mehrere parallele, quer zur Fluglinie versetzte Trajektorien vor, ergeben sich zwei synthetische Aperturen mit denen sich 3-D Rückstrahlprofile erstellen lassen. Diese zuletzt genannte Abbildungsmodalität bezeichnet man als SAR Tomographie. Sie wird üblicherweise realisiert, indem zunächst ein Stapel von zueinander registrierten 2-D SAR-Bildern erstellt wird, wovon jeweils ein Bild zu einem der parallelen Trajektorien gehört. Die dritte Dimension erhält man dann durch 1-D Standardspektralabschätzungsverfahren. Eine typische Anwendung ist die 3-D Abbildung von Vegetationsgebieten. Durch das hohe Durchdringungsvermögen der vergleichsweise langen Radarwellen hat sich SAR Tomographie als ein wertvolles Instrument für die Schätzung von Waldstrukturen und der Quantifizierung von Biomasse herausgestellt. In Hinblick auf geplante Satellitenmissionen mit langwelligen Radarsensoren und Ausrichtung auf eine globale Abdeckung der Erdoberfläche gewinnen tomographische SAR Verfahren zunehmend an Bedeutung. Ein Problem der klassischen idealen 3-D Abbildung anhand solcher Bildstapel ist die Anforderung einer hohen Anzahl dichter, regelmäßiger Datenaufnahmen, welche nicht nur begrenzt verfügbar und teuer sind, sondern auch signifikante zeitliche Dekorrelation mit sich bringen.

Diese Dissertation untersucht das Potential einer Verringerung der Anzahl von Auf-

nahmen für die 3-D SAR Abbildung von Waldgebieten durch die Formulierung des Problems mittels der auf dem Prinzip der Dünnbesetztheit (engl. “sparsity”) basierenden Theorie des “compressed sensing” (CS). Konkret wird der o.g. Schritt der 1-D Spektralabschätzung so modelliert, dass sich das zu bestimmende vertikale Rückstreuungsprofil als eine dünnbesetzte Lösung eines unterbestimmten linearen Gleichungssystem in einem alternativen Raum berechnen lässt. Waveletbasen stellen sich dabei als eine geeignete Wahl heraus. Die Formulierung der vorgeschlagenen Methode erfolgt sowohl für Einkanal- als auch polarimetrische Sensoren. Es wird dabei nicht nur die physikalische Gültigkeit des Modells, sondern auch dessen Robustheit gegenüber nichtidealen Aufnahmen gezeigt. Diese Verfahren werden anhand der Distanz zwischen Sensor und dem abzubildenden Ziel, notwendiger Vorkenntnisse, und benötigter Rechenzeit bewertet. Des Weiteren wird in dieser Dissertation ein auf konvexer Optimierung basierendes Verfahren zur Separation von Rückstreuklassen vorgeschlagen. Dieser Schritt dient als Vorfilter tomographischer Datensets und bewirkt eine Trennung der zwei Rückstreuungsanteile Schirm—also die Oberschicht des Waldes—und Boden, wonach sich diese Anteile separat rekonstruieren lassen. Abschließend wird das vorgestellte Gesamtkonzept anhand von vom Deutschen Zentrum für Luft- und Raumfahrt (DLR) zur Verfügung gestellten, durch den experimentellen SAR (E-SAR) Sensor aufgenommenen L- und P-Band Daten vollständig validiert.

Acknowledgements

If someone about to embark on her/his PhD were to ask me for advice, I would start with a perfectly obvious, yet often forgotten, habit: *to acknowledge other people's help, no matter how big or small*. Accordingly, I would like to express my gratitude to the people who have supported me, in one way or another, to bring my PhD to completion.

First and foremost, I would like to express my sincere gratitude to my supervisor, Andreas Reigber, for still being a PhD student at heart. I thank him for his thorough mentoring, absolute honesty, and infinite flexibility. Andreas gave me the freedom to diversify and branch out into new areas, which ultimately allowed me to find my PhD topic. I am grateful for his encouragement to present at international conferences and to enroll in additional courses, which not only helped me develop my professional career but also my personal life. Moreover, I am indebted to Matteo Nannini for his continuous optimism concerning my work and for all the hours spent firing ideas off one another. My PhD would not have been possible without his willingness to share his years of experience in SAR tomography. I would also like to thank Olaf Hellwich for welcoming me at the Technical University of Berlin. I am grateful for his valuable advice, feedback, and encouragement, especially during the cumbersome admission process.

I would like to show my gratitude to Pau Prats, Rolf Scheiber, and Alberto Moreira. This thesis would hardly have been completed without their encyclopedic knowledge of SAR. I thank them for their dedication, time, and patience. I also owe my deepest gratitude to Richard Bamler and Massimo Fornasier, from the Technical University of Munich, for giving me the possibility of expanding my knowledge on Estimation Theory and Sparse Reconstruction. Furthermore, this thesis would not have been possible without the work of Alessandra Budillon, Xiaoxang Zhu, Stefano Tebaldini, and Laurent Ferro-Famil. Their contributions to SAR tomography have been a great source

of inspiration for me. I am additionally grateful to my professors from the National Technological University of Mendoza who were always willing to put in a good word for me to boost my professional career: Alejandro Vazquez, Raúl Moralejo, Aníbal Mirasso, Carmen Cejudo, and Carlos Troglia. Also, I would like to acknowledge Igor Carron for the enormous impact his blog on Compressed Sensing (Nuit Blanche) had on my research.

It is a pleasure to thank my colleagues from the German Aerospace Center whose support made this thesis possible: Muriel Pinheiro, Octavio Ponce, Russel Que, Jagmal Singh, Jakub Bieniarz, Octavian Dimitru, Kevin Alonso, Janja Avbelj, Jens Fischer, Steffen Peter, Claas Grohnfeldt, Marc Jäger, Marc Rodríguez, Ralf Horn, Martin Keller, and Stefan Sauer. I also want to express my gratitude to my colleagues from the Technical University of Berlin: Olivier D'Hondt, Stéphane Guillaso, and Marion Dennert.

I would like to express my warmest gratitude to the friends who have always supported me: Juan Pablo del Peral, Javier Tassi, Ezequiel Castellanos, Gonzalo del Peral, Facundo Rodríguez, Carlos Rodríguez, Martín Ibáñez, José Martín, Daniel Alarcón, Carolina Luzón, Francisco Azcárate, Marco Briganti, Omar Moreno, José Muñiz, Gastón Gadea, Pablo de los Ríos, Fernando García, Jorgelina Zucchi, Jorge Zucchi, Juan Pablo Moldero, Aníbal Manzur, Pablo Rizzo, Osvaldo Peinado, Emmanuel Bardet, Sam Essa, Patrick Boelaars, Maud Boelaars, Ronald Hofkens, Stephan van Campen, Karl Schröter, Claudia Bertini, Santiago Arias, Luciano Belli, Lucio Pasolli, and Darío Álvarez. I also owe a great debt of gratitude to Arnold Bock for his tremendous support, parental mentoring, and eye-opening advice. Further, I wish to acknowledge Soledad Moreiras and Mónica Quiroga whose help allowed me to start working on my PhD.

I am deeply indebted to my family who has always nourished my hopes and dreams: my brother Jose Aguilera, my parents, my grandparents, the Olguín family, Claudio Andía, Alex and Yolande Hertzog, Javier Sancho, Ruud and Marijke Groeneweg, Jet Groeneweg, and Jaap Akerboom.

Finally, I would not be writing these acknowledgments if it were not for the unconditional support of my loving wife, Lotte Aguilera. She made sure I kept my feet on the ground during the trying PhD period. I really appreciate her joining me in my PhD endeavor, even when this decision came at great personal sacrifice.

Esteban Aguilera

Contents

List of Figures

List of Symbols

A	steering matrix
$a\left(x,\rho,\eta\right)$	reflectivity at (x,ρ,η)
$a\left(x,\rho\right)$	reflectivity at (x,ρ)
$\mathcal{B}$	unit L_1-ball
$b_i^{\perp}$	ith perpendicular baseline
C	polarimetric covariance matrix
C_{CN}	polarimetric covariance matrix for the CN phenomenon
C_{GB}	polarimetric covariance matrix for the GB phenomenon
C_{GC}	polarimetric covariance matrix for the GC phenomenon
C_{GT}	polarimetric covariance matrix for the GT phenomenon
C_{G}	polarimetric covariance matrix for the ground SM
C_{V}	polarimetric covariance matrix for the volume SM
c	speed of light
c_j	jth-scale scaling coefficients
d_j	jth-scale wavelet coefficients
$\boldsymbol{E}\left(\rho,t\right)$	electric field
$\boldsymbol{E}_x$	amplitude of electric field (x-axis)
$\boldsymbol{E}_\eta$	amplitude of electric field (η-axis)
$\boldsymbol{E}_x^{\text{R}}$	amplitude of received electric field (x-axis)
$\boldsymbol{E}_\eta^{\text{R}}$	amplitude of received electric field (η-axis)
$\boldsymbol{E}_x^{\text{T}}$	amplitude of transmitted electric field (x-axis)
$\boldsymbol{E}_\eta^{\text{T}}$	amplitude of transmitted electric field (η-axis)
$\boldsymbol{E}_{\text{R}}\left(t\right)$	received monochromatic wave
$\underline{\boldsymbol{E}}_{\text{R}}\left(t\right)$	received monochromatic wave (rotated)
$\boldsymbol{E}_{\text{T}}\left(t\right)$	transmitted monochromatic wave
$\underline{\boldsymbol{E}}_{\text{T}}\left(t\right)$	transmitted monochromatic wave (rotated)
e_i	ith eigenvector
f	discrete cross-range reflectivity
f_{HH}	discrete cross-range reflectivity (HH)

f_{VV}	discrete cross-range reflectivity (VV)
f_{HV}	discrete cross-range reflectivity (HV)
f_{pol}	discrete cross-range reflectivity (polarimetric)
g	multi-baseline measurements
g_0	wavelet filter
g_{HH}	multi-baseline measurements (HH)
g_{VV}	multi-baseline measurements (VV)
g_{HV}	multi-baseline measurements (HV)
g_{pol}	multi-baseline measurements (polarimetric)
$g_{\text{T}}(t)$	modulating waveform
H	FB or CB projection matrix
h_0	scaling filter
$h_{\text{2-D}}(x, \rho)$	azimuth-range impulse response
$h_x(x)$	azimuth impulse response
$h_\rho(\rho)$	range impulse response
K_0	covariance matrix
$\widehat{K}$	sample covariance matrix
K_{G}	covariance matrix for the ground SM
K_{V}	covariance matrix for the volume SM
$K_{\text{HH–HH}}$	HH–HH covariance matrix
$K_{\text{VV–HH}}$	VV–HH covariance matrix
$K_{\text{HV–HH}}$	HV–HH covariance matrix
$K_{\text{HH–VV}}$	HH–VV covariance matrix
$K_{\text{VV–VV}}$	VV–VV covariance matrix
$K_{\text{HV–VV}}$	HV–VV covariance matrix
$K_{\text{HH–HV}}$	HH–HV covariance matrix
$K_{\text{VV–HV}}$	VV–HV covariance matrix
$K_{\text{HV–HV}}$	HV–HV covariance matrix
K_{pol}	multi-baseline polarimetric covariance matrix
$\underline{K}_{\text{pol}}$	rearranged multi-baseline polarimetric covariance matrix
$\widehat{\underline{K}}_{\text{pol}}$	rearranged multi-baseline polarimetric sample covariance matrix
$\underline{K}^2_{\text{pol}}$	best rank-2 approximation of $\underline{K}_{\text{pol}}$
$k_{\text{HH–HH}}$	vectorized HH–HH covariance matrix
$k_{\text{VV–VV}}$	vectorized VV–VV covariance matrix
$k_{\text{HV–HV}}$	vectorized HV–HV covariance matrix
$\widehat{k}_{\text{HH–HH}}$	vectorized HH–HH sample covariance matrix
$\widehat{k}_{\text{VV–VV}}$	vectorized VV–VV sample covariance matrix

$\widehat{k}_{\text{HV–HV}}$	vectorized HV–HV sample covariance matrix
$\boldsymbol{k}_{\text{L}}$	lexicographic vector representation
$\boldsymbol{k}_{\text{P}}$	Pauli vector representation
L_{az}	physical azimuth antenna length
L_{sa}	along-track synthetic aperture
L_{tom}	tomographic aperture
$\mathcal{O}$	big O notation
$\underline{P}_{\text{pol}}$	matrix of polarimetric cross-range profiles
$\underline{P}_{\text{pol}_j}$	jth row of $\underline{P}_{\text{pol}}$ rearranged into a 3-by-3 matrix
p_{CB}	CB cross-range power
p_{FB}	FB cross-range power
p_{CN}	cross-range power distribution for the CN phenomenon
p_{GB}	cross-range power distribution for the GB phenomenon
p_{GC}	cross-range power distribution for the GC phenomenon
p_{GT}	cross-range power distribution for the GT phenomenon
p_{G}	cross-range power distribution for the ground SM
p_{V}	cross-range power distribution for the volume SM
$p_{\text{HH–HH}}$	HH–HH cross-range profile
$p_{\text{VV–HH}}$	VV–HH cross-range profile
$p_{\text{HV–HH}}$	HV–HH cross-range profile
$p_{\text{HH–VV}}$	HH–VV cross-range profile
$p_{\text{VV–VV}}$	VV–VV cross-range profile
$p_{\text{HV–VV}}$	HV–VV cross-range profile
$p_{\text{HH–HV}}$	HH–HV cross-range profile
$p_{\text{VV–HV}}$	VV–HV cross-range profile
$p_{\text{HV–HV}}$	HV–HV cross-range profile
Q_{A}	polarimetric anisotropy
Q_{E}	polarimetric entropy
q_i	eigenvalue probability
$R(\rho, \eta)$	closest radar-to-target distance
$R_i(\rho, \eta)$	closest radar-to-target distance for the ith pass
$r(x)$	radar-to-target distance
$\mathcal{S}$	translated null space
S	scattering matrix
S_ζ	rotated scattering matrix
S_{HH}	HH scattering coefficient

S_{VV}	VV scattering coefficient
S_{HV}	HV scattering coefficient
S_{VH}	VH scattering coefficient
$s\left(x,t\right)$	demodulated echo
$s_{RCM}\left(x,t\right)$	RCM-corrected echo
$\overline{s}_{RCM}\left(x,\rho\right)$	RCM-corrected echo as a function of range
$T\left(\zeta\right)$	rotation matrix
t	range time
$u\left(x,\rho\right)$	SAR image
V	orthonormal basis for polarimetric signatures
$\overline{V}_i$	ith basis vector for polarimetric signatures
v_i	ith right-singular vector
v_{m}	number of vanishing moments
W	bandwidth of transmitted waveform
$\overline{W}_i$	ith basis vector for structure matrices
w	angular frequency
w_i	ith left-singular vector
x	azimuth axis
y	ground-range axis
z	elevation axis
α_{max}	maximum alpha angle
α_{mean}	mean alpha angle
$\gamma\left(x,\rho,\eta\right)$	cross-range reflectivity
$\Delta\xi$	tomographic sampling interval
δ_K	RIP constant
δ_{NSP}	NSP constant
ε	upper bound on perturbation level
η	cross-range axis
θ	look angle
λ	wavelength
λ_i	ith eigenvalue
μ_0	coherence
$\hat{\mu}_i$	deramped ith SAR pixel
$\hat{\mu}_i\left(x,\rho\right)$	deramped ith SAR image
ξ_i	ith cross-range (spatial) frequency
ρ	range axis
ϱ_x	azimuth resolution

ϱ_η	cross-range resolution
ϱ_ρ	range resolution
ϱ_{real}	real-aperture azimuth resolution
σ_i	ith singular value
τ, τ_1, τ_2	penalty parameters
τ_{CB}	diagonal-loading factor for CB
Φ	cobaseline sensing matrix
ϕ	orientation angle of linearly polarized wave
$\varphi(\varsigma)$	basic scaling function
Ψ	sparsifying basis
$\psi(\varsigma)$	basic wavelet function
ψ_x	phase shift introduced by SM (x-axis)
ψ_η	phase shift introduced by SM (η-axis)
$\left\|\cdot\right\|_2$	L_2-norm
$\left\|\cdot\right\|_1$	L_1-norm
$\left\|\cdot\right\|_{2,1}$	mixed norm
$\left\|\cdot\right\|_{\text{F}}$	Frobenius matrix norm
$\left\|\cdot\right\|_{\text{TV}}$	total-variation norm
$(\cdot)^T$	transpose
$(\cdot)^\dagger$	conjugate transpose
$(\cdot)^{-1}$	inverse
$(\cdot)^c$	complement of a set
$\left\|\cdot\right\|$	absolute value
$\lceil\cdot\rceil$	smallest following integer
$E\{\cdot\}$	expectation
$\mathcal{N}(\cdot)$	null space
$\odot$	element-wise multiplication
$\otimes$	Kronecker product
$\star$	convolution
$\#$	cardinality of a set
$\text{col}(\cdot)$	column index corresponding to linear index of covariance matrix
$\text{conj}(\cdot)$	complex conjugate
$\text{diag}_1(\cdot)$	main diagonal of a matrix
$\text{diag}_2(\cdot)$	diagonal matrix with main diagonal given by the argument
$\max\{\cdot,\cdot\}$	largest value of a two-element set
$\text{row}(\cdot)$	row index corresponding to linear index of covariance matrix
$\text{vec}(\cdot)$	matrix to vector operation

List of Acronyms

1-D	One-Dimensional
2-D	Two-Dimensional
3-D	Three-Dimensional
CB	Capon Beamforming
CN	Canopy Backscattering
CS	Compressed Sensing
DLR	German Aerospace Center
DWT	Discrete Wavelet Transform
E-SAR	Experimental SAR Airborne Sensor
FB	Fourier Beamforming
GB	Ground Backscattering
GC	Double-Bounce Scattering From Ground–Canopy Interactions
GT	Double-Bounce Scattering From Ground–Trunk Interactions
LHS	Left-Hand Side
LS	Least Squares
NSP	Null Space Property
PRF	Pulse Repetition Frequency
RCM	Range Cell Migration
RHS	Right-Hand Side
RIP	Restricted Isometry Property
RMSE	Root Mean Square Error
SAR	Synthetic Aperture Radar
SKP	Sum of Kronecker Products
SM	Scatterer Mechanism
SNR	Signal-To-Noise Ratio
SVD	Singular-Value Decomposition
TV	Total Variation

1 Introduction

1.1 Motivation

A synthetic aperture radar (SAR) is a pulsed imaging system which is able to measure the electromagnetic response of an ensemble of scatterers by active microwave illumination. In its basic form, this is achieved by means of a coherent airborne/spaceborne radar pointing perpendicular to the direction of flight, which ideally follows a linear path [Curl 91, Cumm 05]. The resulting monostatic side-looking configuration, known as *stripmap* mode, and the corresponding antenna's illumination footprint, are illustrated in Figure 1.1. In order to characterize this sensing geometry, five axes are typically considered, as listed below:

x : azimuth (along-track direction)
y : ground-range
z : elevation
ρ : range (line-of-sight direction with look angle θ)
η : cross-range

These axes form the coordinate systems $x\,y\,z$ and $x\,\rho\,\eta$. Subsequent processing of the return echoes [Curl 91, Baml 92, Cumm 05, Elac 06, Wood 06] leads to the formation of a high-resolution 2-D complex-valued image, where each pixel corresponds to a patch of the illuminated area. A typical case is that of a bare surface, for which the electromagnetic response can be expressed—effectively—as a function of either azimuth–range (x, ρ) or azimuth–ground-range (x, y) coordinates, i.e., in two dimensions regardless of a scatterer's location along the η-axis [Clou 10]. As a result, the scattering process

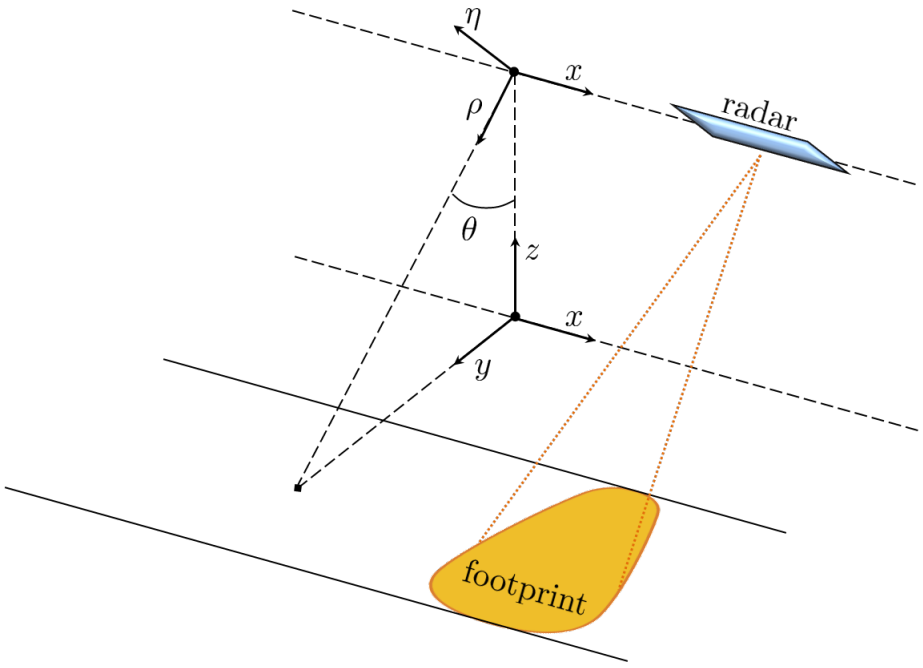

Figure 1.1: Side-looking acquisition geometry in stripmap mode.

can be fully characterized by a single 2-D azimuth–range SAR image, albeit with a level of detail determined by the resolution cell. Specifically, the azimuth ϱ_x and range ϱ_ρ resolutions can be shown to be given by:

$$\varrho_x = \frac{L_{\text{az}}}{2} \tag{1.1}$$

$$\varrho_\rho = \frac{c}{2W} \tag{1.2}$$

where L_{az} denotes the physical azimuth antenna length, c is the speed of light, and W is the bandwidth of the illuminating waveform [Curl 91, Cumm 05].

Very often, however, the region under consideration presents more complex structures. Cases in point are urban and forested areas, in which scattering processes are likely to spread along the cross-range η-axis. As a consequence, all dimensions (i.e., azimuth, range, *and* cross-range) are required for an unambiguous characterization of the electromagnetic response. In this respect, a single SAR image is of limited use, in that—by assuming a plane electromagnetic wave [Baml 98]—scatterers located at the same azimuth–range position (x, ρ), albeit at different cross-range coordinates η, are bound to be mapped to the same SAR pixel. More formally, let g_1 be a specific azimuth–range SAR pixel. Then, the mapping of n targets—distributed along η—into g_1 can be written

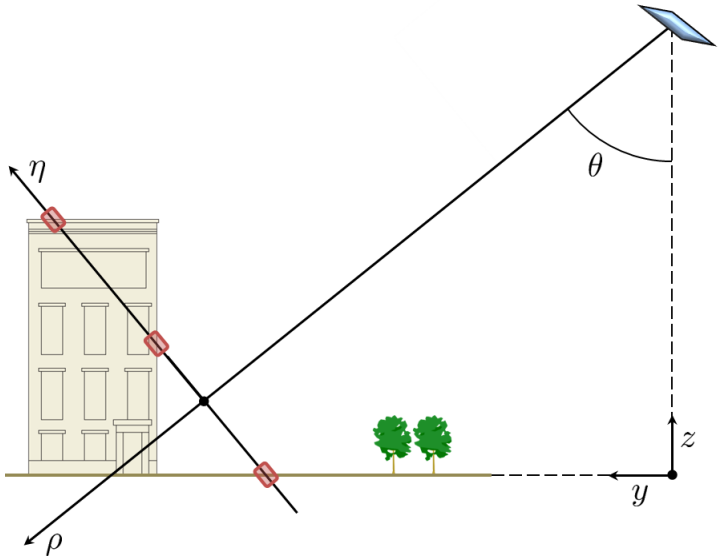

Figure 1.2: Simplified short-wavelength acquisition geometry for an urban area. Contributions from the roads, walls, and rooftops are indicated by the red boxes.

as:

$$g_1 = a_1 \sum_{l=1}^{n} f_l \tag{1.3}$$

where f_l is the electromagnetic reflectivity (and hence $|f_l|^2$ is the backscattered power) of the lth target and a_1 is a mapping coefficient that is related to the wavelength of the system and the range position of the scatterer [Baml 98]. From (1.3), it is clear that a single SAR pixel carries only aggregated information about the cross-range reflectivity and hence its spatial distribution cannot be resolved. This is depicted in Figures 1.2 and 1.3 for an urban and a forested region, respectively. Note that, since short wavelengths are usually preferred for urban areas [Lomb 09b, Zhu 10a, Zhu 10b], only a few targets are expected to contribute to the radar returns [Zhu 10a]. As illustrated in Figure 1.2, the main contributions along the η-axis will be mainly due to roads, walls, and rooftops. On the contrary, the analysis of vegetated areas is generally conducted at long wavelengths in order to exploit their high-penetration capabilities [Reig 00, Frey 08, Teba 09, Nann 11, Frey 11b, Teba 12, dAle 12]. Figure 1.3 illustrates the respective volumetric contributions along the η-axis, which can be assumed to originate from the ground and the canopies.

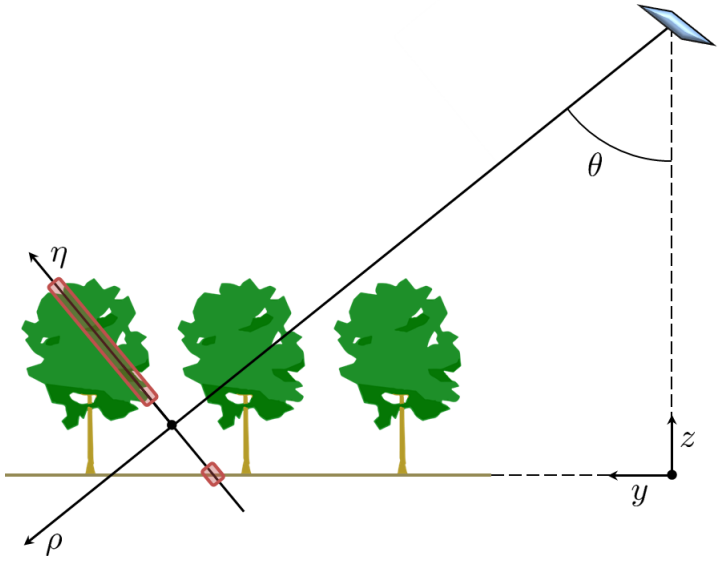

Figure 1.3: Simplified long-wavelength acquisition geometry for a forested area. Contributions from the ground and the canopies are indicated by the red boxes.

When multiple parallel acquisitions—with cross-track and/or elevation displacements—are available (see Figure 1.4), multiple 2-D SAR images can be obtained. By letting m be the number of acquisitions, it is possible to form an m-element vector g (i.e., a stack of m pixels) that corresponds to a specific azimuth–range position. Incidentally, this set of measurements can be shown to be related to the cross-range electromagnetic reflectivity by means of the following linear projection:

$$g = Af \tag{1.4}$$

where f is an n-element vector that represents the reflectivity along the η-axis (note that f may have zero-valued elements, thus being able to capture n scatterers at most); and A is an m-by-n partial Fourier matrix that depends on the operating wavelength and the closest radar-to-target distance for each parallel pass [Reig 00,Nann 11]. As a result, equation (1.4) provides a system of equations from which the unknown reflectivity f and, in turn, the cross-range spatial distribution can be estimated. Accordingly, the resolution cell is not only defined by ϱ_x and ϱ_ρ but also by the cross-range resolution ϱ_η which, assuming a linear inversion of (1.4) [Reig 00], is given by:

$$\varrho_\eta = \frac{\lambda\rho}{2L_{\text{tom}}} \tag{1.5}$$

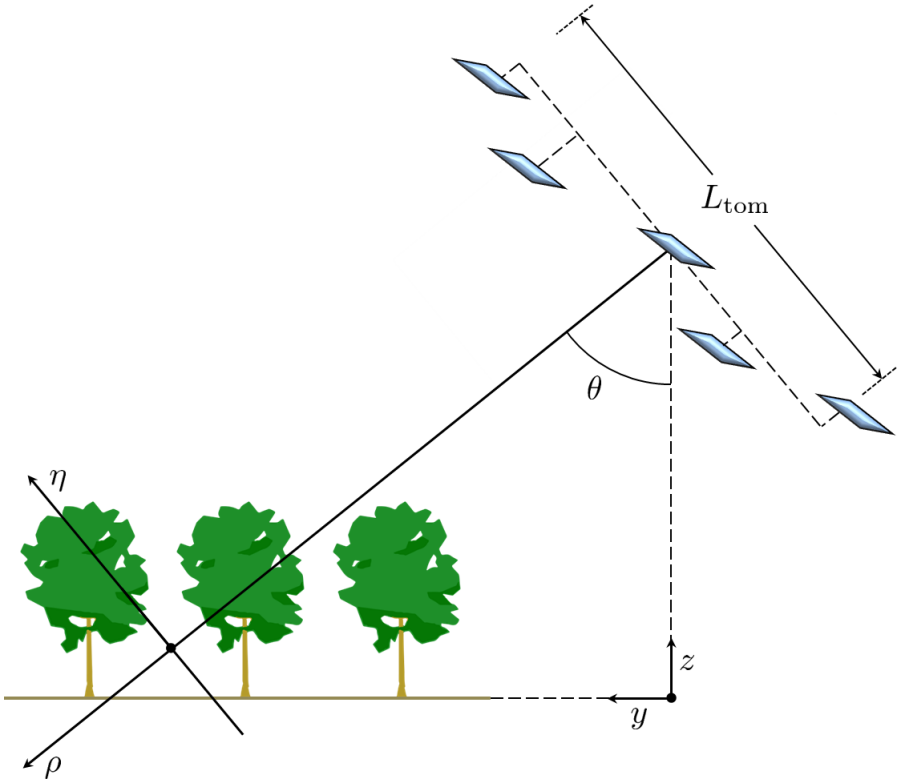

Figure 1.4: Multiple parallel acquisitions with cross-track and elevation displacements.

where λ is the operating wavelength, ρ is the range distance under consideration, and L_{tom} is the effective coverage achieved by the multiple parallel passes (see Figure 1.4). [Reig 00, Forn 03, Nann 11].

Note that the previously described imaging modality, which will be referred to as *SAR tomography*, is ruled by standard sampling conditions [Reig 00, Nann 11] and thus requires a large number of dense regular acquisitions—whereas a larger cross-track coverage L_{tom} provides a better cross-range resolution, a closer spacing between adjacent passes enlarges the unambiguous range of heights dictated by the Nyquist rate. Thus, a standard linear inversion of (1.4) is not only limited by the sensor's capacity but can also lead to temporal decorrelation [Zebk 92, Hans 01]. As a result, the ability to deal with sparse SAR constellations has become of increasing importance, especially with the anticipated advent of long-wavelength spaceborne radars, such as BIOMASS (P-band) [Toan 11] and Tandem-L (L-band) [More 11].

1.2 Previous Work

Subsequent to the first demonstration of SAR tomography [Pasq 95, Home 96, Reig 00], several extensions and alternatives have been put forward in order to attain low sidelobe and ambiguity levels with a reduced number of irregular passes. The use of adaptive spectral estimators was introduced in [Gini 02, Lomb 03, Lomb 09a, Lomb 09b] and further developed in [Saue 11, Frey 11a] (see also [Frey 11b]). In addition, subspace-based spectral estimators, such as the multiple signal classification (MUSIC) algorithm, have been recently employed [Guil 05, Nann 09, Frey 11a, Frey 11b, Huan 12, Lomb 13]. In [Forn 03], the authors formulated the tomographic inversion under the framework of linear inverse problems, thus exploiting the truncated singular-value decomposition (TSVD). Also, a maximum *a posteriori* estimator was developed in [Zhu 10b]. Other publications have addressed irregular geometries by means of interpolation techniques (see, for example, [Lomb 08a, dAle 12]). Alternatively, an extension of SAR interferometry [Baml 98] from a parametric perspective was proposed in [Teba 10a]. In a nutshell, this last work employs covariance matching estimation techniques in order to estimate the effective scattering center of different scattering mechanisms (SMs), along with their backscattered power (see also [Lomb 98a, Cors 99, Bess 00]). Moreover, the author in [Clou 06] introduced the concept of polarization coherence tomography (PCT). Basically, the method exploits the variation of the interferometric coherence with polarization to estimate ground topography and height of vegetation layers. Then, it uses these parameters to represent a backscatter profile as a Fourier–Legendre series. Finally, sparsity-based inversion techniques were introduced in [Budi 09, Zhu 10a, Budi 11, Zhu 12, Agui 12a]. In essence, the authors applied and further developed the relatively new compressed sensing (CS) theory to achieve super-resolution imaging of vertically-sparse targets.

Among the aforementioned tomographic methodologies, CS stands out for its ability to mitigate reconstruction artifacts due to unfavorable sampling conditions (i.e., nonideal acquisition geometries) by exploiting sparse representations. Nevertheless, much of the mainstream [Budi 09, Zhu 10a, Budi 11, Agui 11, Agui 12a, Zhu 12, Schm 13] has focused on spatially-sparse profiles since, as previously pointed out and illustrated in Figure 1.2, this is a reasonable assumption for urban areas, where cross-range profiles generally include only 1–4 targets [Zhu 12]. Accordingly, a common approach is to

formulate the CS inversion of (1.4) as follows [Zhu 10a, Budi 11] (see also [Zhu 12]):

$$\boxed{\begin{aligned} &\text{find the sparsest } \widetilde{f} \\ &\qquad \text{subject to: } \; g = A\widetilde{f} \end{aligned}} \tag{1.6}$$

In other words, this method singles out a solution $\widetilde{f}$ with the least number of nonzero elements from among the infinitely many solutions to the system of equations $g = A\widetilde{f}$, which is hence assumed to be underdetermined (i.e., $m < n$). Interestingly, under suitable assumptions on the matrix A, (1.6) allows for perfect reconstruction of f [Budi 09, Zhu 10a, Budi 11, Agui 13c]. In addition, the authors in [Agui 11, Agui 12a] extended this standard CS technique so as to exploit the structural homogeneity commonly exhibited by neighboring cross-range profiles [Agui 11, Agui 12a, Schm 13]. In order to address this case, let L be an arbitrary number of adjacent azimuth–range positions and $f\,(i)$ be the ith profile to be recovered from $g\,(i)$, with $1 \leq i \leq L$. Then, the joint CS formulation can be written as [Agui 11, Agui 12a]:

$$\boxed{\begin{aligned} &\text{find the sparsest } \widetilde{f}\,(i) \;\text{ for all } 1 \leq i \leq L \\ &\qquad \text{subject to: } \; g\,(i) = A\widetilde{f}\,(i) \\ &\qquad \text{such that: } \; \text{the ensemble } \widetilde{f}\,(i) \text{ exhibits common support} \end{aligned}} \tag{1.7}$$

Thus, this method singles out an ensemble of solutions such that all vectors $\widetilde{f}\,(i)$ have a common set of few nonzero entries. As a result of exploiting this specific joint-sparsity pattern, this approach has been shown to perform better than L independent instances of (1.6) [Elda 09, Elda 10, Agui 12a].

1.3 Contribution

This section summarizes the main contributions of this thesis, which are the result of the doctoral research conducted at the Microwaves and Radar Institute (HR), German Aerospace Center (DLR). The aforementioned assumption of sparsity is reconsidered

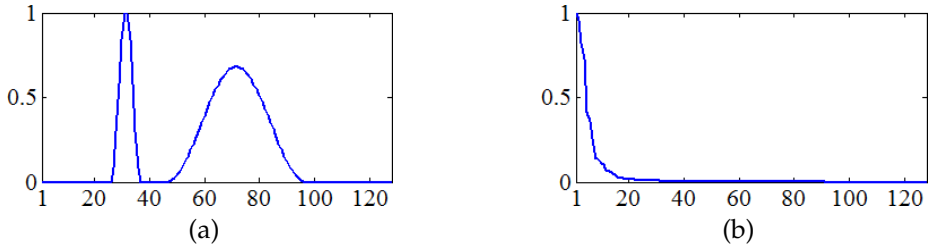

Figure 1.5: (a) Power (as a function of height with $n = 128$) of a typical cross-range profile encountered over forested terrain. (b) Sorted magnitudes of the transform coefficients using a Daubechies Symmlet wavelet with 4 vanishing moments and 3 levels of decomposition.

first, followed by simple mathematical formulations of the tomographic methodologies proposed in this work. Furthermore, a quick preview of the achieved results is provided. For this purpose, high-quality L- and P-band tomographic datasets have been considered, which were obtained by the Experimental SAR (E-SAR) airborne sensor of DLR near Dornstetten, Germany, in 2006 [Nann 09, Nann 11], and near Umeå, Sweden, in 2008 [Hajn 09], respectively.

From Figure 1.3, it is easy to see that the presence of canopies of moderate extent are bound to render the assumption of sparsity invalid. In fact, to all intents and purposes, cross-range sparsity is rarely the case when it comes to vegetated areas [Agui 13c]. By way of illustration, Figure 1.5(a) shows a typical backscattered-power profile over forested terrain where two components can be readily identified. Whereas the right-hand side component accounts for the canopy, the left-hand side one accounts for contributions located at ground level. Incidentally, their respective power distributions are considerably regular [Agui 13c], which suggests the existence of a basis in which these components can be sparsely represented [Mall 09]. In light of previous work in the context of SAR [Bhat 08, Sama 09, Pott 10, Wu 11] and other fields (see, for example, [Lust 07, Lori 07]), this thesis explores the tomographic problem in the context of wavelet bases [Daub 88, Daub 92, Mall 09]. As a motivating example, Figure 1.5(b) shows the rapid decay of the sorted magnitudes of the transform coefficients corresponding to Figure 1.5(a), obtained using a Daubechies Symmlet wavelet with 4 vanishing moments and 3 levels of decomposition [Mall 09]. Thus, it might seem as if sparse-reconstruction techniques could be similarly applied for forested areas. In effect, while equation (1.4) provides an underdetermined system of equations, the assumption of sparsity in the wavelet domain provides a means of singling out the right solution. There is, however, a glitch: the linear model given by (1.4) is formulated in terms of the (complex-valued) reflectivity f and not in terms of its (nonnegative real-

valued) intensity/power, hereinafter denoted by p. Interestingly, as will be elaborated on in subsequent chapters, it is also possible to obtain a system of equations based on p, which can be formulated as follows:

$$k = \Phi p \tag{1.8}$$

where k is an m^2-element vector estimated from an ensemble of observations $g\,(i)$ of arbitrary size as previously considered; and Φ is an m^2-by-n matrix constructed from A in (1.4). Accordingly, the tomographic reconstruction can be written as [Agui 13c]:

$$\boxed{\begin{array}{c}\text{find the sparsest } \widetilde{p} \text{ in the wavelet domain} \\ \text{subject to: } \; k = \Phi\widetilde{p} \\ \text{such that: } \; \widetilde{p} \text{ is physically valid}\end{array}} \tag{1.9}$$

where the constraint of physical validity can be simply ensured by enforcing nonnegativity of $\widetilde{p}$. In order to demonstrate the potential of this wavelet-based approach, Figure 1.6 shows a comparison of tomographic slices along azimuth as a function of height. The reconstruction has been carried out using widely-used nonparametric methods, namely, the Fourier (FB) and Capon (CB) beamformers [Lomb 03, Saue 11], which will be reviewed in Section 2.4. Figure 1.6(a) has been obtained by FB with 21 regular acquisitions and will therefore be considered as a reference. The approximately horizontal line at the bottom of each image corresponds to the terrain (relative height $\cong 10$ m). Most of the vertical canopy distribution lies between 20–33 m. Additionally, Figures 1.6(b)–(d) present FB, CB, and CS slices, respectively, corresponding to 6 irregular parallel passes. Unlike FB and CB, the CS reconstruction bears comparison with the 21-pass FB one and thus shows its robustness to nonideal acquisition geometries. In this respect, detailed comparisons will be reported toward the end of this work.

Note that the previously outlined wavelet-based methodology can also be extended so as to exploit wave polarization. As will be developed in the chapters to come, fully-polarimetric acquisitions result in nine n-element vectors of unknowns to be estimated. By arranging these vectors side-by-side, it is possible to form an n-by-9 matrix as fol-

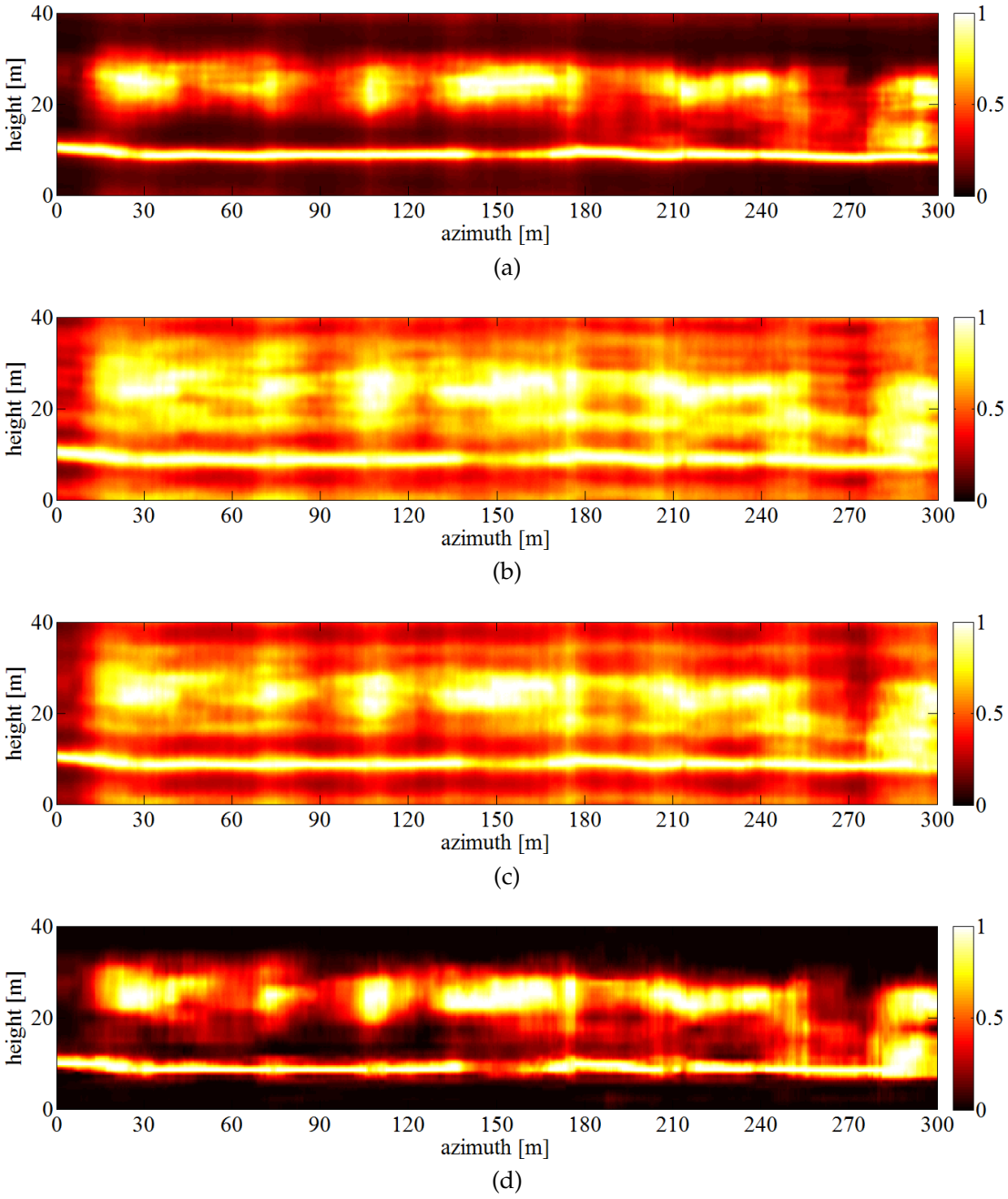

Figure 1.6: Tomographic slices at L-band (normalized at every position) obtained as a function of azimuth and height (300 m by 40 m). (a) FB reconstruction with 21 passes. (b) FB reconstruction with 6 passes (c) CB reconstruction with 6 passes. (d) CS reconstruction with 6 passes. Range distance: 4816.30 m.

lows:

$$\underline{P}_{\text{pol}} = \begin{bmatrix} p_1 & p_2 & \cdots & p_9 \end{bmatrix} \tag{1.10}$$

Consequently, the corresponding nine systems of equations can be compactly written as:

$$\underline{K}_{\text{pol}} = \Phi \underline{P}_{\text{pol}} \tag{1.11}$$

where Φ is the same m^2-by-n matrix given in (1.8); and $\underline{K}_{\text{pol}}$ is an m^2-by-9 matrix. Since the ensemble p_i, with $1 \leq i \leq 9$, is expected to have common support in the wavelet domain [Agui 13a], (1.7) and (1.9) can be combined to formulate the tomographic reconstruction as follows:

$$\begin{array}{|rl|}\hline \text{find the sparsest } \widetilde{p}_i \text{ in the wavelet domain for all } 1 \leq i \leq 9 & \\ \text{subject to:} & \underline{K}_{\text{pol}} = \Phi \widetilde{\underline{P}}_{\text{pol}} \\ \text{such that:} & \text{the ensemble } \widetilde{p}_i \text{ exhibits common support in} \\ & \text{the wavelet domain and is physically valid} \\ \hline \end{array} \tag{1.12}$$

where the property of physical validity can be enforced by constraining each row of $\widetilde{\underline{P}}_{\text{pol}}$ (when rearranged in a 3-by-3 matrix) to be positive-semidefinite [Agui 13a]. As a consequence, this approach enables a complete 3-D electromagnetic characterization, which is an essential input to various applications, such as image segmentation, classification [Lee 09], and soil moisture estimation [Lee 09, Reig 13, Jagd 13].

An additional contribution of this dissertation is the development of a methodology for separation of SMs. Figure 1.7(a) illustrates an alternative example of the power distributions of the two SMs previously mentioned and illustrated in Figure 1.5. The ground-level contributions appear in red, while the canopy or volume component is shown in green. As originally devised in [Teba 09], it is possible to use multiple acquisitions and wave polarization to filter these two SMs—prior to tomographic processing—by exploiting their uncorrelated polarimetric responses. As a result, techniques such as FB, CB, and/or CS can be eventually applied on these components separately. In this regard, this thesis introduces an optimization-based technique to accomplish this filtering/separation. As presented by Figure 1.7(b), this separation has been achieved and subsequently used for recovering two independent tomographic slices by means of CB with 9 passes. Again, the ground-level contributions appear in red, while the volume contributions are depicted in green. Note that some volume

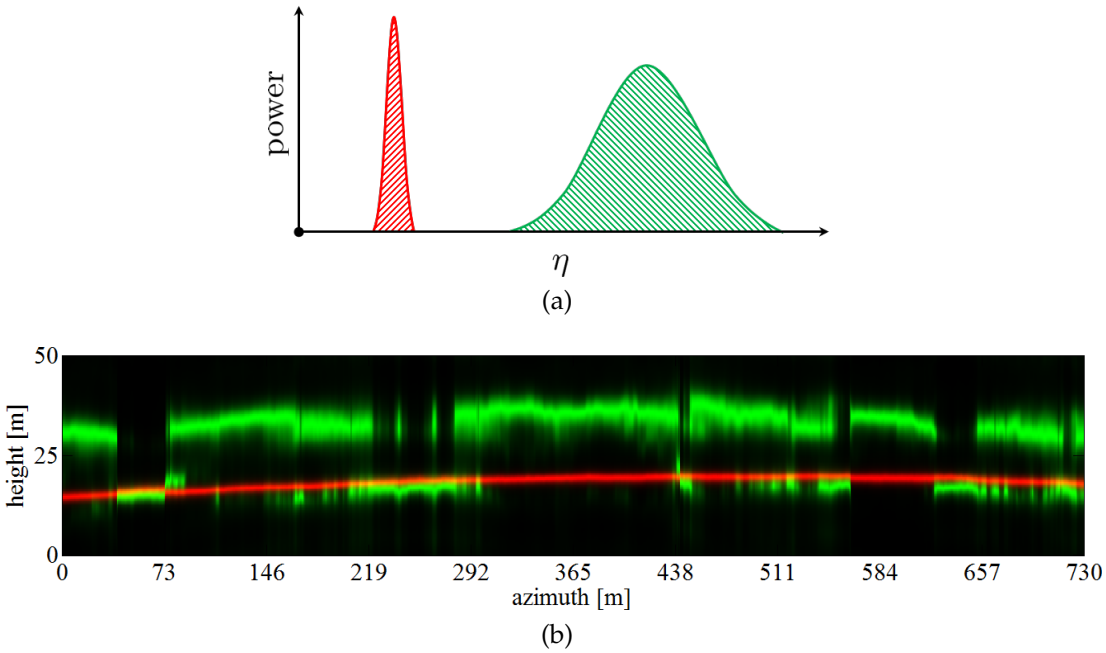

Figure 1.7: Two SMs (red: ground-level SM; green: volume SM). (a) Illustration of power distributions for a specific azimuth–range position. (b) Tomographic slice at P-band obtained by CB using 9 passes.

components also manifest at ground level, thus suggesting the presence of understory or ground–canopy interactions [Teba 12].

1.4 Synopsis

The primary objective of this work is to explore new directions for the development of SAR tomography for natural distributed scenes in the context of sparse reconstruction and optimization. With this in mind, emphasis is placed on the mathematical formulation of the proposed techniques. As a result, once the formal definition of a specific problem is covered, the reader is expected to proceed from a digital signal processing perspective. The remainder of this thesis can be summarized as follows:

– Chapter 2 provides a detailed introduction to the fundamentals of SAR and SAR tomography. The tomographic sensing operator and standard sampling requirements are derived first, followed by a review of two well-known tomographic techniques for forested areas, namely, FB and CB.

– Chapter 3 forms the basis for subsequent chapters by introducing the basics of radar polarimetry and widely-used covariance matrix models for forest scattering. In essence, these models are able to relate the second-order statistics of radar observables to structural and electromagnetic properties of forested areas. In addition, eigendecomposition-based polarimetric parameters are defined.

– Chapter 4 revisits the concept of sparse recovery by providing a review of CS sampling strategies and reconstruction guarantees. In addition, the case of multiple jointly-sparse signals is reviewed. Then, the tomographic problem is regarded as an instance of CS—by considering both single-channel and polarimetric measurements—with additional physical constraints. Finally, an introduction to wavelets is provided together with the motivation for their application to SAR tomography.

– Chapter 5 reviews the concept of algebraic separation of ground and volume SMs and introduces a convex optimization approach to achieving such separation.

– Chapter 6 introduces a set of sufficient, but not necessary, conditions for ensuring convexity of optimization problems. Then, it breaks down all the relevant tomographic-related optimizations so as to show how these conditions are verified.

– Chapter 7 presents experimental results obtained using polarimetric L- and P-band data acquired by the E-SAR sensor of DLR. First, the methods proposed in this work are evaluated in terms of range distance, acquisition geometry, required *a priori* knowledge, and computation time. Subsequently, polarimetric analyses are carried out for assessing the physical validity of the tomographic reconstructions. Finally, various tomographic slices demonstrating the algebraic separation of SMs are presented.

– Lastly, Chapter 8 provides some final considerations and concludes this thesis.

2 SAR Tomography Fundamentals

Airborne/spaceborne SAR sensors are microwave instruments capable of producing high-resolution 2-D reflectivity maps by synthesizing a very large virtual antenna. In essence, this is accomplished by illuminating an area while physically moving a small antenna, followed by a processing step that coherently combines the received echoes. As will be shown, a key aspect is that the achieved resolution does not depend on the radar-to-target distance or operating wavelength, but rather on the system bandwidth and the real antenna size. In addition, when multiple parallel trajectories are considered, a further combination of the resulting set of 2-D images allows for 3-D backscatter profiling with a vertical resolution that depends on the cross-track/elevation coverage. This chapter presents a detailed review of this 3-D image formation process. First, the single-pass 2-D impulse response is derived. Then, multiple SAR-image pixels corresponding to parallel acquisitions are shown to be related to the 3-D reflectivity via a Fourier transform. Finally, standard Nyquist conditions are reviewed along with widely-used tomographic techniques for forested areas.

2.1 SAR Basics

The first step in the SAR imaging process consists of scanning an area, such as a forest or a city, by means of a side-looking airborne/spaceborne radar. As the platform moves along its—ideally straight—path, microwave pulses are transmitted at equispaced along-track positions according to the system's pulse repetition frequency (PRF) [Curl 91, Cumm 05]. Each pulse transmission is followed by a receive window during which return echoes are recorded. Figure 2.1 depicts a typical imaging configuration, referred to as *stripmap* mode [Baml 98, Cumm 05, More 13], where the radar is assumed to point perpendicular to the direction of flight. Two coordinate systems

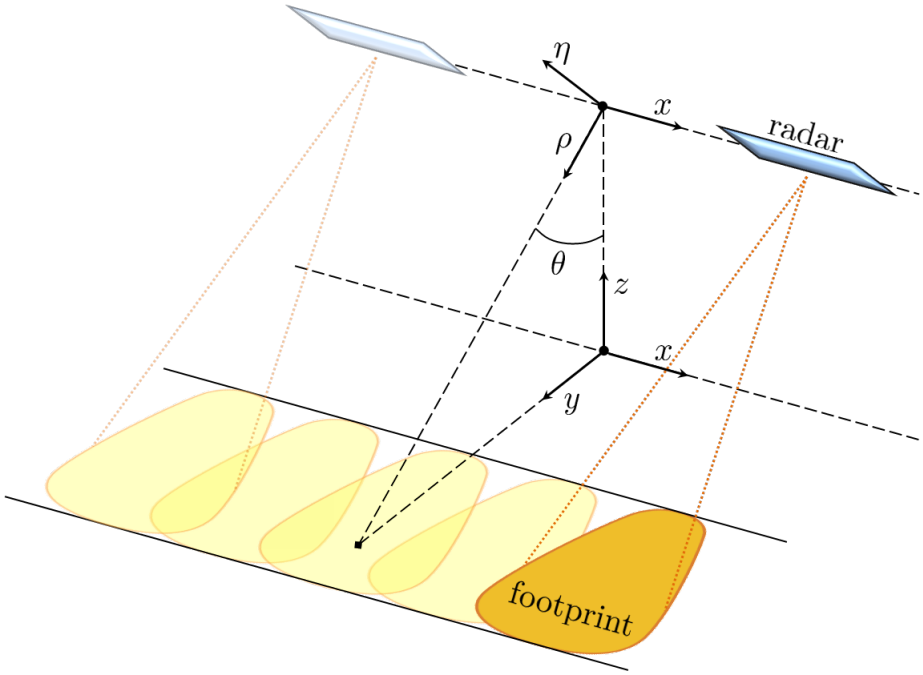

Figure 2.1: 3-D side-looking acquisition geometry in stripmap mode.

have been considered, namely, $x\,y\,z$ and $x\,\rho\,\eta$, which originate from the following axes:

x : azimuth (along-track direction)
y : ground-range
z : elevation
ρ : range (line-of-sight direction with look angle θ)
η : cross-range

Due to the inherent cylindrical symmetry of monostatic acquisitions, and under the assumption of a plane electromagnetic wave [Baml 98], the dependence on the η coordinate is usually made implicit, as illustrated in Figure 2.2. In order to further describe this data acquisition step, the response of a single point scatterer will be considered. Let $a\left(x',\rho'\right)$ be the complex-valued reflectivity of a stationary scatterer located at (x',ρ'). Then, after quadrature demodulation, the received signal can be modeled as [Baml 98, More 13]:

$$s\left(x,t\right)=\begin{cases} a\left(x',\rho'\right)\times\exp\left(-j\frac{4\pi}{\lambda}r\left(x\right)\right)\times g\left(t-\frac{2r\left(x\right)}{c}\right) & \text{if } \left|x-x'\right|\leq L_{\text{sa}}/2 \\ 0 & \text{otherwise} \end{cases} \tag{2.1}$$

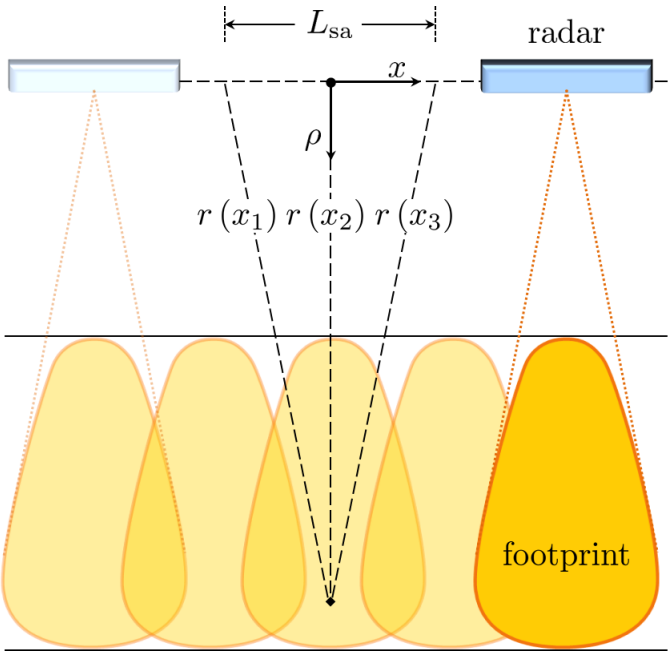

Figure 2.2: 2-D geometry obtained by making the dependence on the η coordinate implicit.

where $r(x)$ is the distance from the scatterer to the radar at azimuth position x; λ is the pulse carrier wavelength; $L_{sa} = \lambda\rho'/L_{az}$ is the so-called *synthetic aperture* (see Figure 2.2), where L_{az} denotes the physical azimuth antenna length; and $g_T(t)$ represents the modulating waveform, assumed to be given by:

$$g_T(t) = \text{sinc}(tW) \quad \text{with} \quad \text{sinc}(\varsigma) = \frac{\sin \pi\varsigma}{\pi\varsigma} \tag{2.2}$$

where t is the range time and W is the signal bandwidth [1].

The next step is that of SAR image formation or *focusing* [Curl 91, Baml 92, Cumm 05, Elac 06, Wood 06] and will be assumed to be comprised of two parts, namely, a time-shift correction and the application of a matched filter [Klau 60, Curl 91]. Thus, first note that, as is clear from the rightmost factor in equation (2.1), the varying distance $r(x)$ introduces a time shift $2r(x)/c$. The resulting deviation, which is referred to as *range cell migration* (RCM) [Brow 69, Leit 73], is given by $2(r(x) - \rho')/c$. Once this effect

[1] Note that chirp signals are used in practice [Klau 60, Curl 91, Cumm 05].

has been corrected [Curl 91, More 13], the scatterer's response can be written as:

$$s_{RCM}(x,t) = a(x',\rho') \times \exp\left(-j\frac{4\pi}{\lambda}r(x)\right) \times g_{\mathrm{T}}\left(t - \frac{2\rho'}{c}\right) \tag{2.3}$$

where the dependence on the illumination footprint has been, and will hereinafter be, made implicit. For the sake of interpretation, an equivalent expression as a function of azimuth and range can be found as follows:

$$\begin{aligned}
\overline{s}_{RCM}(x,\rho) &= s_{RCM}\left(x, \frac{2\rho}{c}\right) && (2.4)\\
&= a(x',\rho') \times \exp\left(-j\frac{4\pi}{\lambda}r(x)\right) \times g_{\mathrm{T}}\left(\frac{2\rho}{c} - \frac{2\rho'}{c}\right) && (2.5)\\
&= a(x',\rho') \times \exp\left(-j\frac{4\pi}{\lambda}r(x)\right) \times g_{\mathrm{T}}\left(\frac{2}{c}(\rho - \rho')\right) && (2.6)
\end{aligned}$$

which, by letting

$$\begin{aligned}
h_{\rho}(\rho) &= g_{\mathrm{T}}\left(\frac{2\rho}{c}\right) && (2.7)\\
&= \mathrm{sinc}\left(\frac{2\rho}{c}W\right) && (2.8)
\end{aligned}$$

denote the range impulse response, leads to:

$$\overline{s}_{RCM}(x,\rho) = a(x',\rho') \times \exp\left(-j\frac{4\pi}{\lambda}r(x)\right) \times h_{\rho}(\rho - \rho') \tag{2.9}$$

Also, note that it follows from Figure 2.2 that the varying radar-to-target distance is given by:

$$r(x) = \sqrt{\rho'^2 + (x - x')^2} \tag{2.10}$$

which, provided $(x - x')/\rho' \ll 1$, can be approximated as follows:

$$r(x) \cong \rho' + \frac{(x - x')^2}{2\rho'} \tag{2.11}$$

Consequently, (2.9) can be written as:

$$\overline{s}_{RCM}(x,\rho) = a(x',\rho') \times \exp\left(-j\frac{4\pi}{\lambda}\rho'\right) \times \exp\left(-j\frac{4\pi}{\lambda}\frac{(x-x')^2}{2\rho'}\right) \times h_\rho(\rho-\rho') \quad (2.12)$$

$$= a(x',\rho') \times \exp\left(-j\frac{4\pi}{\lambda}\rho'\right) \times \exp\left(-j\pi\frac{2}{\lambda\rho'}(x-x')^2\right) \times h_\rho(\rho-\rho') \quad (2.13)$$

where the third factor gives rise to a chirp signal along azimuth with chirp rate $2/(\lambda\rho')$ [Klau 60]. The second part of the focusing step is then to exploit this azimuth-dependent phase history by applying a matched filter [Klau 60,Curl 91]. Specifically, the final SAR image $u(x,\rho)$ is obtained as follows:

$$u(x,\rho) = \overline{s}_{RCM}(x,\rho) \star \exp\left(j\pi\frac{2}{\lambda\rho'}x^2\right) \quad (2.14)$$

$$= a(x',\rho') \times \exp\left(-j\frac{4\pi}{\lambda}\rho'\right) \times h_x(x-x') \times h_\rho(\rho-\rho') \quad (2.15)$$

where $\star$ denotes the convolution operator; the filter kernel is assumed to be zero outside the interval $[-L_{\text{sa}}/2, +L_{\text{sa}}/2]$; and $h_x(x)$ is the azimuth impulse response given by (omitting constant factors):

$$h_x(x) = \text{sinc}\left(x\frac{2L_{\text{sa}}}{\lambda\rho'}\right) \quad (2.16)$$

Furthermore, by considering $h_\rho(\rho)$ in (2.8) and $h_x(x)$ in (2.16), the 2-D azimuth–range impulse response can be written as (see Figure 2.3):

$$h_{\text{2-D}}(x,\rho) = h_x(x) \times h_\rho(\rho) \quad (2.17)$$

and hence $u(x,\rho)$ simplifies to:

$$u(x,\rho) = a(x',\rho') \times \exp\left(-j\frac{4\pi}{\lambda}\rho'\right) \times h_{\text{2-D}}(x-x',\rho-\rho') \quad (2.18)$$

As an example of what $u(x,\rho)$ typically looks like, Figure 2.4 shows the amplitude of an X-band SAR image of Traunstein, Germany, which has been projected onto the ground-range y-axis.

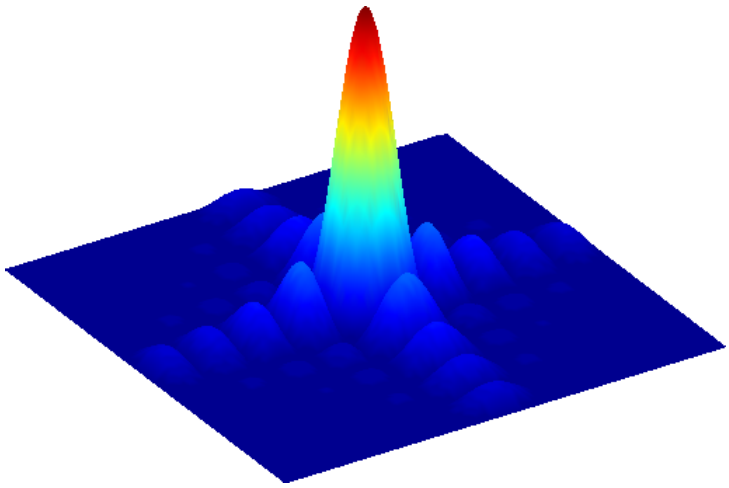

Figure 2.3: Illustration of the 2-D impulse response.

Finally, by considering the distance from the peak to the first null for $h_x(x)$ and $h_\rho(\rho)$, it is possible to define the maximum achievable azimuth and range resolutions as follows [Curl 91]:

$$\varrho_x = \frac{\lambda}{2L_{\text{sa}}}\rho' \tag{2.19}$$

$$\varrho_\rho = \frac{c}{2W} \tag{2.20}$$

In this respect, it is important to note that, while the azimuth resolution of a real-aperture system would be given by $\varrho_{\text{real}} = \lambda\rho'/L_{\text{az}}$ [Huyg 90], the previously outlined focusing step allows for *synthesizing* an azimuth resolution equivalent to that provided by a real aperture of $2L_{\text{sa}}$—and hence the name SAR [Curl 91]. In addition, since $L_{\text{sa}} = \lambda\rho'/L_{\text{az}}$, it follows that:

$$\varrho_x = \frac{\lambda}{2\lambda\rho'/L_{\text{az}}}\rho' \tag{2.21}$$

$$= \frac{L_{\text{az}}}{2} \tag{2.22}$$

which shows its invariance with respect to wavelength and range distance. Consequently, the space-invariant 2-D impulse response is more conveniently formulated as follows [Forn 03]:

$$h_{\text{2-D}}(x,\rho) = \text{sinc}\left(\frac{x}{\varrho_x}\right) \times \text{sinc}\left(\frac{\rho}{\varrho_\rho}\right) \tag{2.23}$$

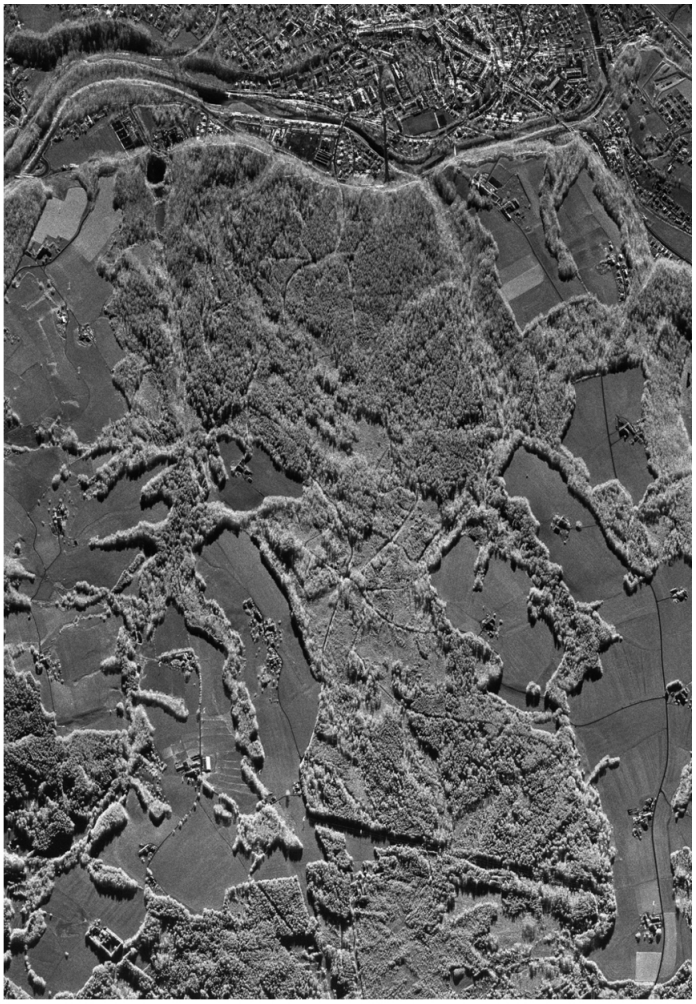

Figure 2.4: Amplitude of SAR image (X-Band / HH channel) of Traunstein, Germany. Range projected to ground-range.

2.2 SAR Tomography

As a result of the previous derivations, it is possible to model the SAR image of a general complex reflectivity $a(x, \rho)$ as follows [Baml 98, Forn 03, Teba 10a]:

$$u(x, \rho) = \iint a(x', \rho') \times \exp\left(-j\frac{4\pi}{\lambda}\rho'\right) \times h_{2\text{-D}}(x - x', \rho - \rho')\, dx' d\rho' \tag{2.24}$$

That is, as the result of applying a low-pass filter $h_{2\text{-D}}(x, \rho)$ to $a(x, \rho)$. Nonetheless, in the presence of complex structures—targets distributed along the η-axis—it is helpful to expand equation (2.24) so as to explicitly account for the cross-range distribution of

the scene. Since, due to cylindrical symmetry, it had been assumed that:

$$a\left(x,\rho\right)=\int a\left(x,\rho,\eta'\right)d\eta' \tag{2.25}$$

where $a\left(x,\rho,\eta\right)$ represents the reflectivity of a scatterer located at (x,ρ,η), it follows that the SAR image can also be expressed as [Baml 98, Forn 03, Teba 10a]:

$$u\left(x,\rho\right)=\iiint a\left(x',\rho',\eta'\right)\times\exp\left(-j\frac{4\pi}{\lambda}\rho'\right)\times h_{\text{2-D}}\left(x-x',\rho-\rho'\right)dx'd\rho'd\eta' \tag{2.26}$$

which, in turn, gives:

$$u\left(x,\rho\right)=\iiint a\left(x',\rho',\eta'\right)\times\exp\left(-j\frac{4\pi}{\lambda}R\left(\rho',\eta'\right)\right)\times h_{\text{2-D}}\left(x-x',\rho-\rho'\right)dx'd\rho'd\eta' \tag{2.27}$$

where $R\left(\rho,\eta\right)$ is the closest distance from the scatterer to the radar. As is clear from equation (2.26), targets distributed along the cross-range axis cannot be resolved.

When multiple parallel acquisitions—with cross-track and/or elevation displacements referred to as *baselines*—are available (see Figure 2.5), a stack of 2-D SAR images can be obtained and subsequently coregistered [2] with respect to a reference coordinate system $x\,\rho\,\eta$ [Reig 00, Forn 03, Teba 10a]. Since the closest radar-to-target distance varies as a function of baseline extent, the resulting ith SAR image can be modeled as follows:

$$\begin{aligned}
&u_i\left(x,\rho\right)\\
&\quad=\iiint a\left(x',\rho',\eta'\right)\times\exp\left(-j\frac{4\pi}{\lambda}R_i\left(\rho',\eta'\right)\right)\times h_{\text{2-D}}\left(x-x',\rho-\rho'\right)dx'd\rho'd\eta' &(2.28)\\
&\quad\cong\iiint a\left(x',\rho',\eta'\right)\times\exp\left(-j\frac{4\pi}{\lambda}R_i\left(\rho,\eta'\right)\right)\times h_{\text{2-D}}\left(x-x',\rho-\rho'\right)dx'd\rho'd\eta' &(2.29)\\
&\quad=\int\left(\iint a\left(x',\rho',\eta'\right)\times h_{\text{2-D}}\left(x-x',\rho-\rho'\right)dx'd\rho'\right)\times\exp\left(-j\frac{4\pi}{\lambda}R_i\left(\rho,\eta'\right)\right)d\eta' &(2.30)
\end{aligned}$$

[2] Note that, in the case of large baselines and/or high range resolution, a height-dependent coregistration could be required (see, for example, [Nann 07]).

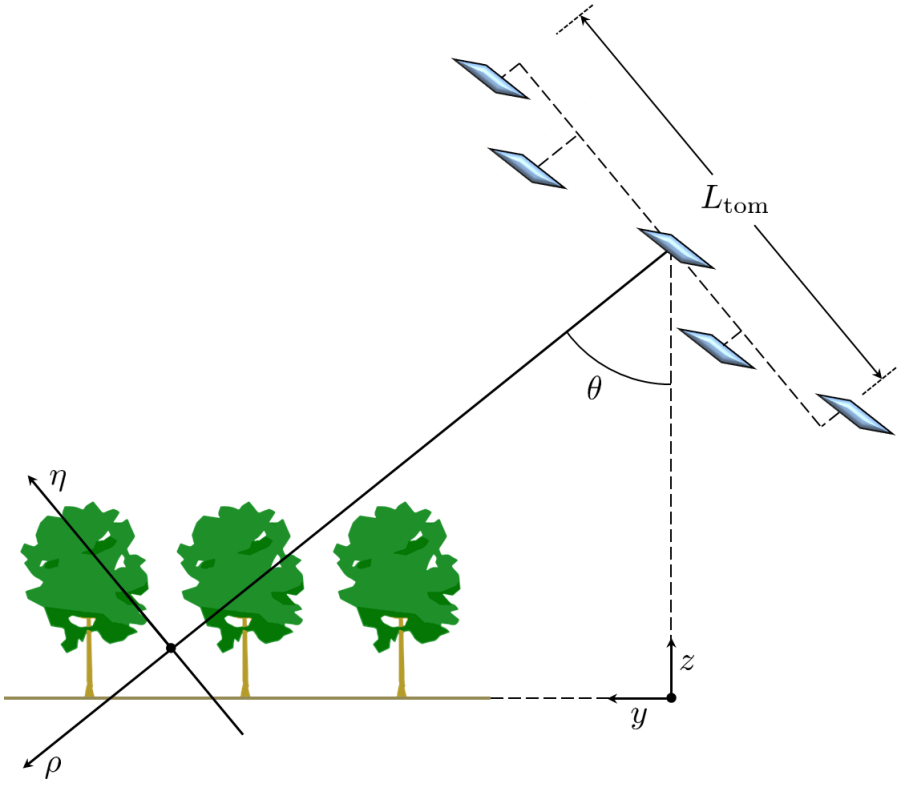

Figure 2.5: Multi-baseline acquisition geometry.

where $R_i(\rho, \eta)$ denotes the closest radar-to-target distance for the ith pass. By letting

$$\gamma(x, \rho, \eta') = \iint a(x', \rho', \eta') \times h_{\text{2-D}}(x - x', \rho - \rho')\, dx' d\rho' \tag{2.31}$$

it is possible to define

$$\hat{u}_i(x, \rho) = \int \gamma(x, \rho, \eta') \times \exp\left(-j\frac{4\pi}{\lambda} R_i(\rho, \eta')\right) d\eta' \tag{2.32}$$

and phase-rotate it with respect to $\eta = 0$ as follows [Reig 00]:

$$\mu_i(x, \rho) = \hat{u}_i(x, \rho) \times \exp\left(j\frac{4\pi}{\lambda} R_i(\rho, \eta = 0)\right) \tag{2.33}$$

which, in turn, can be written as:

$$\mu_i(x,\rho) \cong \int \gamma(x,\rho,\eta') \times \exp\left(j\frac{4\pi}{\lambda\rho}b_i^{\perp}\eta'\right) d\eta' \tag{2.34}$$

$$= \int \gamma(x,\rho,({}^{z'}/_{\sin(\theta)})) \times \exp\left(j\frac{4\pi}{\lambda\rho}b_i^{\perp}({}^{z'}/_{\sin(\theta)})\right) dz' = \hat{\mu}_i(x,\rho) \tag{2.35}$$

where θ is the look angle formed by the reference coordinate system; and $b_i^{\perp}$ denotes the effective baseline, which is defined as the perpendicular component of the baseline with respect to ρ. Thus, by making the azimuth–range dependence implicit, the ith pixel can be expressed as:

$$\hat{\mu}_i = \int \gamma(\eta') \times \exp(j2\pi\xi_i\eta')\, d\eta' \tag{2.36}$$

with

$$\xi_i = \frac{2b_i^{\perp}}{\lambda\rho} \tag{2.37}$$

which shows that $\hat{\mu}_i$ and $\gamma(\eta)$ form a Fourier transform pair and hence, assuming a suitable sampling rate—one that satisfies the Nyquist criterion—it is possible to compute either one from the other [Reig 00, Nann 11]. In accordance with the previous considerations, tomographic SAR imaging can be achieved from a set of 2-D images by solving a 1-D spectral estimation problem (along the η-axis) at every azimuth–range position.

2.3 Standard Sampling Considerations

As it follows from equations (2.36) and (2.37), the tomographic sampling interval is given by:

$$\Delta\xi = \frac{2d}{\lambda\rho} \tag{2.38}$$

where d is the effective separation between adjacent passes. Hence, a sufficient condition (i.e., the Nyquist criterion) to recover a cross-range signal γ of vertical extent Z (i.e., extent along the z-axis) is [Reig 00, Forn 03, Nann 11]:

$$\frac{Z}{\sin(\theta)} \leq \frac{1}{\Delta\xi} \tag{2.39}$$

or equivalently

$$\Delta\xi \leq \frac{\sin(\theta)}{Z} \tag{2.40}$$

or

$$d \leq \frac{\lambda\rho\sin(\theta)}{2Z} \tag{2.41}$$

Nevertheless, since only a limited number of acquisitions are generally available, unambiguous recovery entails a reduced tomographic aperture L_{tom} (see Figure 2.5). As a result, the cross-range and vertical resolutions are given by [Reig 00, Forn 03, Nann 11]:

$$\varrho_\eta = \frac{\lambda}{2L_{\text{tom}}}\rho \tag{2.42}$$

$$\varrho_z = \varrho_\eta \sin(\theta) \tag{2.43}$$

Consequently, for a specific extent Z and a desired vertical resolution ϱ_z, the required number of regular passes is:

$$m = \left\lceil \frac{Z}{\varrho_z} \right\rceil + 1 \tag{2.44}$$

where $\lceil\cdot\rceil$ indicates the smallest following integer. Note, however, that (2.44) does not mean that the desired Z and ϱ_z can be achieved throughout the swath. In fact, this will depend on the range distance and the baseline distribution, as captured by equations (2.41), (2.42), and (2.43).

2.4 Tomographic SAR Techniques

This section revisits two widely-used cross-range power estimators, namely, the Fourier and Capon beamformers [Gini 02, Lomb 03, Jako 05, Saue 11], which will be extensively used for comparison purposes in subsequent sections. To this end, the model described by (2.36) will be henceforth approximated by its discrete counterpart:

$$g = Af \tag{2.45}$$

where $g \in \mathbb{C}^m$ is a stack of m pixels, $A \in \mathbb{C}^{m \times n}$ is a partial Fourier matrix usually referred to as the *steering matrix*, and $f \in \mathbb{C}^n$ denotes a cross-range signal of limited extent. The data vector g is assumed to follow a zero-mean complex circular Gaussian distribution with covariance matrix

$$K_0 = E\left\{gg^\dagger\right\} = AE\left\{ff^\dagger\right\}A^\dagger \tag{2.46}$$

where $K_0 \in \mathbb{C}^{m \times m}$, $E\{\cdot\}$ is the expectation operator, and $(\cdot)^\dagger$ denotes the conjugate transpose [Baml 98]. Accordingly, under the assumption of ergodicity, the corresponding maximum likelihood estimate is found by replacing the expectation operator with spatial averaging as follows:

$$\widehat{K} = \frac{1}{L}\sum_{l=1}^{L} g\left(l\right) g^\dagger\left(l\right) \tag{2.47}$$

where $\widehat{K}$ is the sample covariance matrix and L is the number of independent pixels (or *looks*) being averaged [Baml 98, Saue 11].

Note that the tomographic methods covered below are based on the multi-look sample covariance matrix $\widehat{K}$ rather than g. As a result, not only is the effective azimuth–range resolution inevitably reduced, but also the focus is shifted from the estimation of f to the estimation of its expected power, i.e., the main diagonal of $E\left\{ff^\dagger\right\}$ in (2.46).

2.4.1 Fourier Beamforming

Fourier beamforming (FB) is a linear reconstruction method whose resolving power and ambiguity rejection capabilities are dictated by standard sampling considerations as outlined in Section 2.3 [Stoi 97]. The FB multi-look cross-range power estimate $p_{\text{FB}} \in \mathbb{R}^n_{\geq 0}$ is obtained from:

$$p_{\text{FB}} = \text{diag}_1 \left(H^\dagger \widehat{K} H \right) \tag{2.48}$$

where $\text{diag}_1(\cdot)$ denotes the main diagonal of a matrix and the ith column of H is found by solving the following minimization problem:

$$\boxed{\min_{H^i} \ \left(H^i\right)^\dagger H^i \ \text{subject to} \ \left(H^i\right)^\dagger A^i = 1} \tag{2.49}$$

where A^i is the ith column of A, usually referred to as the ith *steering vector*. The solution to (2.49) can be shown to be [Stoi 97]:

$$H^i = \frac{A^i}{m} \tag{2.50}$$

This estimator has the advantage of being both radiometrically correct and computationally efficient. In practice, however, the artifacts caused by irregular sampling together with the limited resolving power can reduce the applicability of this approach [Teba 12]. Also, note that from equations (2.48) and (2.50), it follows that the FB estimate is obtained by means of a projection matrix H which is independent of the scattering process actually being measured.

2.4.2 Capon Beamforming

Unlike FB, Capon beamforming (CB) is a nonlinear algorithm based on a data-adaptive projection matrix H. The CB multi-look cross-range power estimate $p_{\text{CB}} \in \mathbb{R}^n_{\geq 0}$ is given

by:

$$p_{\text{CB}} = \text{diag}_1\left(H^\dagger \widehat{K} H\right) \tag{2.51}$$

where the ith column of H is the solution to the following minimization problem:

$$\boxed{\min_{H^i} \ \left(H^i\right)^\dagger \widehat{K} H^i \ \text{ subject to } \ \left(H^i\right)^\dagger A^i = 1} \tag{2.52}$$

which can be shown to be [Capo 69, Stoi 97]:

$$H^i = \frac{\widehat{K}^{-1} A^i}{\left(A^i\right)^\dagger \widehat{K}^{-1} A^i} \tag{2.53}$$

and thus CB requires $\widehat{K}$ be an invertible matrix. Very often, however, a limited number of looks causes this matrix to be rank deficient. In such cases, it is a common practice to make $\widehat{K}$ full rank by diagonal loading it [Lomb 03]. Interestingly, employing the CB algorithm based on a diagonal-loaded covariance matrix can be interpreted as a regularized version of CB. In particular, letting τ_{CB} be a loading factor, it follows from (2.52) that H is constructed by solving:

$$\boxed{\min_{H^i} \ \left(H^i\right)^\dagger (\widehat{K} + \tau_{\text{CB}} I_m) H^i \ \text{ subject to } \ \left(H^i\right)^\dagger A^i = 1} \tag{2.54}$$

where I_m is an m-by-m identity matrix. Since equation (2.54) is equivalent to:

$$\boxed{\min_{H^i} \ \left(H^i\right)^\dagger \widehat{K} H^i + \tau_{\text{CB}} \left(H^i\right)^\dagger H^i \ \text{ subject to } \ \left(H^i\right)^\dagger A^i = 1} \tag{2.55}$$

it follows from (2.49) that (2.55) is a regularized version of (2.52) which behaves like FB as $\tau_{\text{CB}} \to \infty$ [Lore 05].

In addition to its moderate computational complexity, the advantages of CB are its

super-resolution and interference rejection capabilities. However, this estimator is known to be sensitive to imprecise steering vectors [Stoi 02] and can exhibit poor radiometric accuracy [Teba 12].

3 Polarimetric Forest Scattering

Natural distributed scenes are characterized by a SAR resolution cell composed of a large number of random scatterers. This leads to the assumption of a zero-mean complex circular Gaussian distribution which is usually exploited by characterizing a scattering process by means of its second-order statistics [Clou 96, Baml 98]. This chapter provides a short introduction to radar polarimetry and introduces widely-used covariance matrix models for forested areas, which will be the basis for developing sparsity-based tomographic techniques in the chapters to come. In addition, basic eigendecomposition-based polarimetric parameters are formulated. Note that, for simplicity of explanation, possible noise contributions as well as any other source of decorrelation [Zebk 92, Baml 98, Hans 01] will be intentionally neglected in this chapter. Also, the estimation of covariance matrices will be henceforth assumed to be carried out by spatial averaging in a form analogous to (2.47).

3.1 Polarimetric SAR

By considering the coordinate system $x\,\rho\,\eta$ introduced in Section 2.1, the monochromatic space-time electric field corresponding to a linearly-polarized planar wave can be written as [Lee 09, Clou 10]:

$$\boldsymbol{E}(\rho,t) = \sqrt{\boldsymbol{E}_x^2+\boldsymbol{E}_\eta^2}\begin{bmatrix}\cos(\phi)\\ \sin(\phi)\end{bmatrix}\exp\left(j\left(wt-\frac{2\pi}{\lambda}\rho\right)\right) \tag{3.1}$$

$$= \begin{bmatrix}\boldsymbol{E}_x\\ \boldsymbol{E}_\eta\end{bmatrix}\exp\left(j\left(wt-\frac{2\pi}{\lambda}\rho\right)\right) \tag{3.2}$$

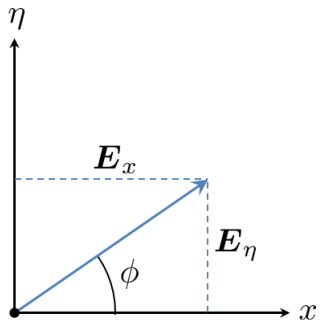

Figure 3.1: Linear polarization with amplitude $\sqrt{\boldsymbol{E}_x^2 + \boldsymbol{E}_\eta^2}$ and orientation angle ϕ.

where $\boldsymbol{E}_x$ and $\boldsymbol{E}_\eta$ are the amplitude components for the x- and η-axes, respectively; ϕ is the orientation angle (see Figure 3.1); w is the angular frequency; and λ denotes the wavelength. It then follows that, for a specific target at range distance r_0 from the radar, the transmitted $\boldsymbol{E}_{\mathrm{T}}(t)$ and received $\boldsymbol{E}_{\mathrm{R}}(t)$ waves can be described by:

$$\boldsymbol{E}_{\mathrm{T}}(t) = \begin{bmatrix} \boldsymbol{E}_x^{\mathrm{T}} \\ \boldsymbol{E}_\eta^{\mathrm{T}} \end{bmatrix} \exp(jwt) \tag{3.3}$$

$$\boldsymbol{E}_{\mathrm{R}}(t) = S\,\boldsymbol{E}_{\mathrm{T}}(t) \exp\left(-j\frac{4\pi}{\lambda} r_0\right) \tag{3.4}$$

$$= S \begin{bmatrix} \boldsymbol{E}_x^{\mathrm{T}} \\ \boldsymbol{E}_\eta^{\mathrm{T}} \end{bmatrix} \exp(jwt) \times \exp\left(-j\frac{4\pi}{\lambda} r_0\right) \tag{3.5}$$

$$= S \begin{bmatrix} \boldsymbol{E}_x^{\mathrm{T}} \\ \boldsymbol{E}_\eta^{\mathrm{T}} \end{bmatrix} \exp\left(j\left(wt - \frac{4\pi}{\lambda} r_0\right)\right) \tag{3.6}$$

$$= \begin{bmatrix} \boldsymbol{E}_x^{\mathrm{R}} \exp(j\psi_x) \\ \boldsymbol{E}_\eta^{\mathrm{R}} \exp(j\psi_\eta) \end{bmatrix} \exp\left(j\left(wt - \frac{4\pi}{\lambda} r_0\right)\right) \tag{3.7}$$

where ψ_x and ψ_η are phase shifts introduced by the SM; and the matrix $S \in \mathbb{C}^{2\times 2}$ accounts for the interaction of the wave with the target and is usually referred to as the *scattering matrix* [Krog 90]. By referring to the horizontal (x-directed) and the vertical (η-directed) components of the wave with H and V, respectively, the scattering matrix S can be written as:

$$S = \begin{bmatrix} S_{\mathrm{HH}} & S_{\mathrm{HV}} \\ S_{\mathrm{VH}} & S_{\mathrm{VV}} \end{bmatrix} \tag{3.8}$$

Note that the transmitted and received waves with respect to $x\,\eta$ can be expressed with respect to any counterclockwise-rotated coordinate system $\overline{x}\,\overline{\eta}$ as follows:

$$\underline{\boldsymbol{E}}_{\mathrm{T}}(t) = T(\zeta)\,\boldsymbol{E}_{\mathrm{T}}(t) \tag{3.9}$$

$$\underline{\boldsymbol{E}}_{\mathrm{R}}(t) = T(\zeta)\,\boldsymbol{E}_{\mathrm{R}}(t) \tag{3.10}$$

with

$$T(\zeta) = \begin{bmatrix} \cos(\zeta) & \sin(\zeta) \\ -\sin(\zeta) & \cos(\zeta) \end{bmatrix} \tag{3.11}$$

where ζ is the rotation angle. Consequently, replacing $\boldsymbol{E}_{\mathrm{R}}(t)$ in equation (3.10) according to (3.4) results in:

$$\underline{\boldsymbol{E}}_{\mathrm{R}}(t) = T(\zeta)\,S\,\boldsymbol{E}_{\mathrm{T}}(t)\exp\left(-j\frac{4\pi}{\lambda}r_0\right) \tag{3.12}$$

which, after replacing $\boldsymbol{E}_{\mathrm{T}}(t)$ according to (3.9), gives:

$$\underline{\boldsymbol{E}}_{\mathrm{R}}(t) = T(\zeta)\,S\,T^{-1}(\zeta)\,\underline{\boldsymbol{E}}_{\mathrm{T}}(t)\exp\left(-j\frac{4\pi}{\lambda}r_0\right) \tag{3.13}$$

$$= S_{\zeta}\underline{\boldsymbol{E}}_{\mathrm{T}}(t)\exp\left(-j\frac{4\pi}{\lambda}r_0\right) \tag{3.14}$$

and hence $S_{\zeta} = T(\zeta)\,S\,T^{-1}(\zeta)$ is a *synthesized* scattering matrix with respect to the rotated coordinate system [Lee 09].

In practice, many radars are designed to transmit/receive with either horizontal or vertical polarization [Clou 96,More 13]. Thus, the scattering coefficients S_{HH}, S_{VV}, S_{HV}, and S_{VH} are measured, respectively, by means of four transmit–receive polarization pairs, often referred to as *polarimetric channels*: HH, VV, HV, and VH. This mode of operation results in four SAR images per acquisition, which may be modeled by equations (2.27) and (2.28) by simply substituting the complex reflectivity a for a_{HH}, a_{VV}, a_{HV}, or a_{VH}, as appropriate.

Finally, note that a monostatic configuration has been assumed so far, which implies $S_{\mathrm{HV}} = S_{\mathrm{VH}}$ [Boer 98]. The lexicographic $\boldsymbol{k}_{\mathrm{L}}$ and Pauli $\boldsymbol{k}_{\mathrm{P}}$ vector representations of the

scattering matrix are therefore given by:

$$\boldsymbol{k}_{\mathrm{L}} = \begin{bmatrix} S_{\mathrm{HH}} \\ \sqrt{2}S_{\mathrm{HV}} \\ S_{\mathrm{VV}} \end{bmatrix} \qquad \boldsymbol{k}_{\mathrm{P}} = \frac{1}{\sqrt{2}} \begin{bmatrix} S_{\mathrm{HH}} + S_{\mathrm{VV}} \\ S_{\mathrm{HH}} - S_{\mathrm{VV}} \\ 2S_{\mathrm{HV}} \end{bmatrix} \tag{3.15}$$

whose norms equal the so-called *span*, i.e., $\|\boldsymbol{k}_{\mathrm{L}}\|_2^2 = \|\boldsymbol{k}_{\mathrm{P}}\|_2^2$ [Boer 81, Kost 86, Clou 86, Borg 87, Borg 89]. Figure 3.2 shows a polarimetric SAR image corresponding to the lexicographic basis.

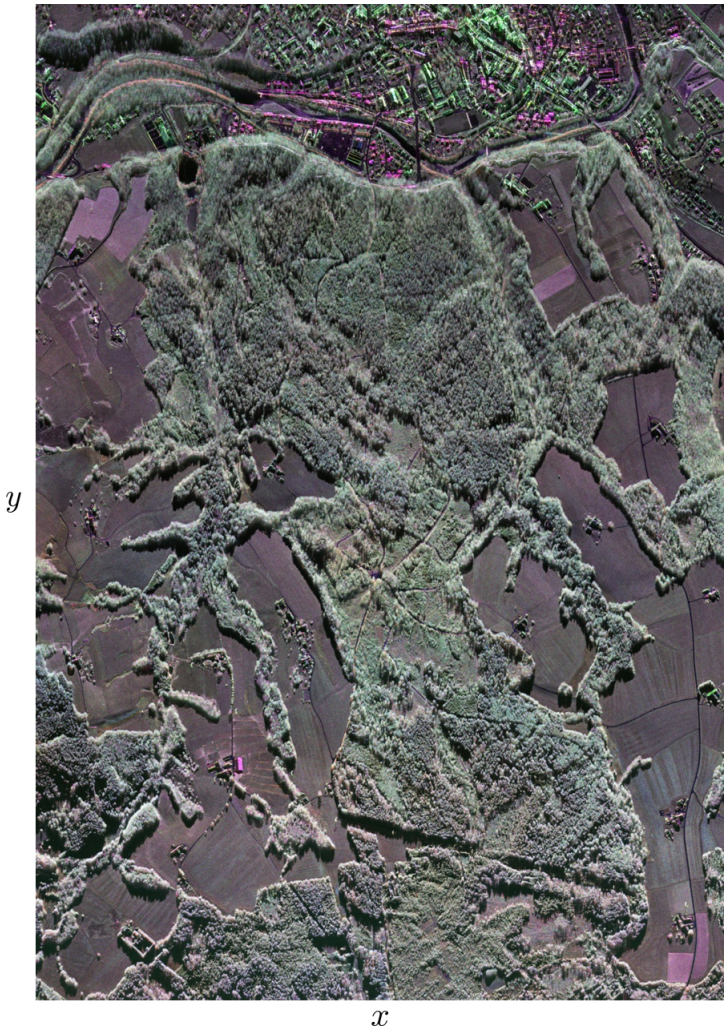

Figure 3.2: Polarimetric SAR image (X-Band / Red: HH; Green: HV; Blue: VV) of Traunstein, Germany. Range projected to ground-range.

3.2 Forest Scattering Model

Due to the high-penetration capabilities of radiation at long wavelengths, such as those within the L- or P-band, forested areas give rise to complex scattering processes which are generally described in terms of the responses and interactions of its constituent targets. Specifically, return echoes are usually assumed to originate from an ensemble of leaves and branches (i.e., the canopy), as well as from the underlying trunks and terrain. With this in mind, the analysis can be restricted to four nonnegligible physical phenomena, namely: ground backscattering, double-bounce scattering from ground–trunk interactions, double-bounce scattering from ground–canopy interactions, and canopy backscattering [Teba 10a]. As illustrated in Figure 3.3, these four phenomena give rise to two effective SMs along cross-range: a ground-locked SM that includes ground-only, ground–trunk, and ground–canopy components; and a volume SM that includes a canopy-only component [Teba 09, Teba 10a, Teba 12]. Alternatively, the volume SM is often assumed to exhibit contributions at ground level either due to the presence of understory or by letting the volume SM (instead of the ground-locked SM) capture the ground–canopy interactions [Teba 09, Teba 10a, Teba 12]. Note that, in light of equation (2.31), while ground–trunk interactions can be modeled as a single point target—and hence are invariant to the look angle θ—the spatial distribution of the remaining three phenomena spreads along cross-range with an extent that is bound to decrease with increasing look angle (see Figure 3.3) [Teba 10a]. More formally, let $\boldsymbol{k}$ be any polarimetric vector representation, as defined by (3.15), for a specific azimuth–range position corresponding to a single SAR acquisition. Under the hypothesis that the underlying physical phenomena are uncorrelated, the *polarimetric covariance matrix* $C \in \mathbb{C}^{3\times 3}$ can be written as [Boer 81, Clou 92]:

$$C = E\left\{\boldsymbol{k}\boldsymbol{k}^{\dagger}\right\} = C_{\mathrm{GB}} + C_{\mathrm{GT}} + C_{\mathrm{GC}} + C_{\mathrm{CN}} \tag{3.16}$$

where GB, GT, GC, and CN denote, respectively, ground backscattering, double-bounce scattering from ground–trunk interactions, double-bounce scattering from ground–canopy interactions, and canopy backscattering. Thus, by letting

$$C_{\mathrm{G}} = C_{\mathrm{GB}} + C_{\mathrm{GT}} + C_{\mathrm{GC}} \tag{3.17}$$

$$C_{\mathrm{V}} = C_{\mathrm{CN}} \tag{3.18}$$

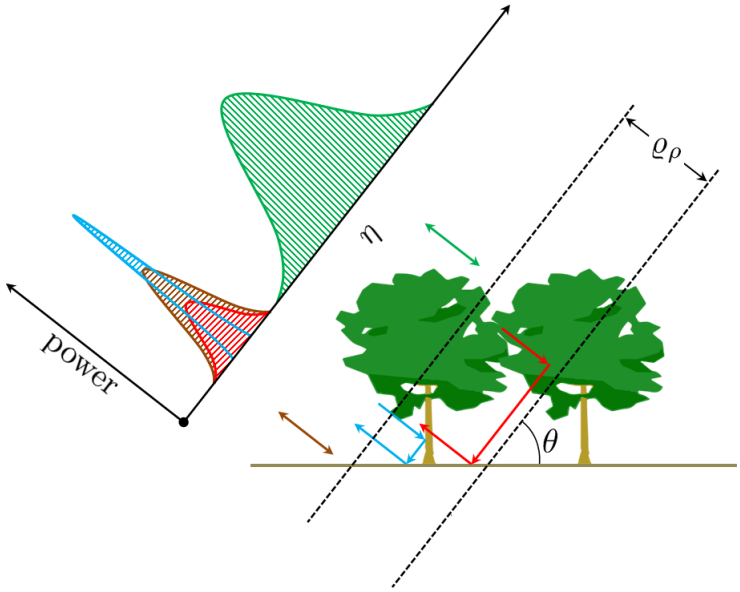

Figure 3.3: Illustration of forest phenomena giving rise to two effective SMs (adapted from [Teba 10a]). Ground-locked SM: (Brown) Ground backscattering. (Light blue) Double-bounce scattering from ground–trunk interactions. (Red) Double-bounce scattering from ground–canopy interactions. Volume SM: (Green) Canopy backscattering.

it is then possible to associate C with two effective SMs:

$$C = E\left\{\boldsymbol{k}\boldsymbol{k}^{\dagger}\right\} = C_{\mathrm{G}} + C_{\mathrm{V}} \tag{3.19}$$

where C_{G} and C_{V} are, respectively, the polarimetric covariance matrices for ground and volume SMs [Teba 09]. The retrieval of such matrices is of considerable interest in its own right, as they allow for a physical characterization of SMs and thus find application in different areas, such as image segmentation, classification, and soil moisture estimation [Lee 09, Reig 13, Jagd 13].

When multi-baseline data are available, the resulting second-order statistics are not only related to the polarimetric response of the scatterers, but also to their cross-range spatial distribution [Papa 01, Teba 09]. This can be understood by first extending the discrete model described by equation (1.4) so as to consider all polarimetric channels. Without loss of generality, consider the lexicographic polarimetric representation and let i denote either HH, VV, or HV. Then, the corresponding stack of m pixels can be written as:

$$g_i = Af_i \tag{3.20}$$

which can be jointly expressed as:

$$g_{\text{pol}} = (I_3 \otimes A)\, f_{\text{pol}} \tag{3.21}$$

where $g_{\text{pol}} = [\ g_{\text{HH}}^{\text{T}} \quad g_{\text{VV}}^{\text{T}} \quad g_{\text{HV}}^{\text{T}}\ ]^{\text{T}} \in \mathbb{C}^{3m}$; $f_{\text{pol}} = [\ f_{\text{HH}}^{\text{T}} \quad f_{\text{VV}}^{\text{T}} \quad f_{\text{HV}}^{\text{T}}\ ]^{\text{T}} \in \mathbb{C}^{3n}$; I_3 is a 3-by-3 identity matrix; and $\otimes$ denotes the Kronecker product, which implies that $(I_3 \otimes A) \in \mathbb{C}^{3m\times 3n}$. The corresponding *multi-baseline polarimetric covariance matrix* $K_{\text{pol}} \in \mathbb{C}^{3m\times 3m}$ can be modeled as [Treu 02, Clou 06, Lomb 08b, Teba 10b]:

$$K_{\text{pol}} = E\left\{g_{\text{pol}} g_{\text{pol}}^{\dagger}\right\} = (I_3 \otimes A)\, E\left\{f_{\text{pol}} f_{\text{pol}}^{\dagger}\right\} \left(I_3 \otimes A^{\dagger}\right) \tag{3.22}$$

with

$$E\left\{f_{\text{pol}} f_{\text{pol}}^{\dagger}\right\} = \begin{bmatrix} \text{diag}_2\left(p_{\text{HH–HH}}\right) & \text{diag}_2\left(p_{\text{HH–VV}}\right) & \text{diag}_2\left(p_{\text{HH–HV}}\right) \\ \text{diag}_2\left(p_{\text{VV–HH}}\right) & \text{diag}_2\left(p_{\text{VV–VV}}\right) & \text{diag}_2\left(p_{\text{VV–HV}}\right) \\ \text{diag}_2\left(p_{\text{HV–HH}}\right) & \text{diag}_2\left(p_{\text{HV–VV}}\right) & \text{diag}_2\left(p_{\text{HV–HV}}\right) \end{bmatrix} \tag{3.23}$$

where, in this context, $\text{diag}_2(\cdot)$ represents a diagonal matrix with its main diagonal given by the argument. Note that $p_{\text{HH–HH}}$, $p_{\text{VV–VV}}$, and $p_{\text{HV–HV}} \in \mathbb{R}^n_{\geq 0}$ correspond to the cross-range powers for the HH, VV, and HV channels, respectively; and that

$$p_{\text{VV–HH}} = \text{conj}\left(p_{\text{HH–VV}}\right) \in \mathbb{C}^n \tag{3.24}$$

$$p_{\text{HV–HH}} = \text{conj}\left(p_{\text{HH–HV}}\right) \in \mathbb{C}^n \tag{3.25}$$

$$p_{\text{HV–VV}} = \text{conj}\left(p_{\text{VV–HV}}\right) \in \mathbb{C}^n \tag{3.26}$$

where $\text{conj}(\cdot)$ indicates complex conjugation.

For the sake of simplicity, (3.22) will be rearranged as follows. Let K_{pol} be represented by a partition matrix of nine m-by-m blocks such that

$$K_{\text{pol}} = \begin{bmatrix} K_{\text{HH–HH}} & K_{\text{HH–VV}} & K_{\text{HH–HV}} \\ K_{\text{VV–HH}} & K_{\text{VV–VV}} & K_{\text{VV–HV}} \\ K_{\text{HV–HH}} & K_{\text{HV–VV}} & K_{\text{HV–HV}} \end{bmatrix} \tag{3.27}$$

and form

$$\underline{K}_{\text{pol}} = \left[\begin{array}{cccc} \text{vec}\left(K_{\text{HH–HH}}\right) & \text{vec}\left(K_{\text{VV–HH}}\right) & \cdots & \text{vec}\left(K_{\text{HV–HV}}\right) \end{array} \right] \tag{3.28}$$

and

$$\underline{P}_{\text{pol}} = \left[\begin{array}{cccc} p_{\text{HH–HH}} & p_{\text{VV–HH}} & \cdots & p_{\text{HV–HV}} \end{array} \right] \tag{3.29}$$

where $\underline{K}_{\text{pol}} \in \mathbb{C}^{m^2 \times 9}$, $\underline{P}_{\text{pol}} \in \mathbb{C}^{n \times 9}$, and $\text{vec}\left(\cdot\right)$ is the matrix to vector operation. Next, construct $\Phi \in \mathbb{C}^{m^2 \times n}$ as follows. Define the functions $\text{row}\left(\cdot\right)$ and $\text{col}\left(\cdot\right)$, which take a linear index corresponding to any vectorized block of $\underline{K}_{\text{pol}}$ as an argument and return the row and column indices corresponding to the original block, respectively. Then, the ℓth row of Φ is given by:

$$\Phi_\ell = A_{\text{row}(\ell)} \odot \text{conj}\left(A_{\text{col}(\ell)}\right) \tag{3.30}$$

where the subscripts indicate a specific row and $\odot$ denotes element-wise multiplication. It then follows that (3.22) is equivalent to:

$$\underline{K}_{\text{pol}} = \Phi \underline{P}_{\text{pol}} \tag{3.31}$$

Note that equations (2.36) and (2.37) imply that, just as every row of A is directly related to a specific baseline, every row Φ_ℓ is related to the difference between baselines $\text{row}\left(\ell\right)$ and $\text{col}\left(\ell\right)$. For this reason, this difference will be hereinafter referred to as *cobaseline*. As will be shown in Section 7.1.1, in order to avoid redundant entries in $\underline{K}_{\text{pol}}$, additional emphasis should be placed on these waveforms. For details on this concept, known in the literature as *minimum redundancy arrays*, the reader is referred to [Line 93, Nann 10].

Under the additional hypotheses that the cross-range spatial distributions of the GB, GT, GC, and CN phenomena are invariant with respect to the choice of polarimetric channel; and that the GB, GT, GC, and CN polarimetric covariance matrices are invariant with respect to the choice of track; $\underline{P}_{\text{pol}}$ can be modeled as [Teba 09, Agui 13a]:

$$\underline{P}_{\text{pol}} = p_{\text{GB}}\text{vec}\left(C_{\text{GB}}\right)^T + p_{\text{GT}}\text{vec}\left(C_{\text{GT}}\right)^T + p_{\text{GC}}\text{vec}\left(C_{\text{GC}}\right)^T + p_{\text{CN}}\text{vec}\left(C_{\text{CN}}\right)^T \tag{3.32}$$

where p_{GB}, p_{GT}, p_{GC}, and $p_{\text{CN}} \in \mathbb{R}^n_{\geq 0}$ will be referred to as, respectively, the *cross-range power distributions* of the GB, GT, GC, and CN phenomena. Likewise, C_{GB}, C_{GT}, C_{GC}, and C_{C}—which correspond to the covariance matrices given by (3.17) and (3.18)—will be referred to as the GB, GT, GC, and CN *polarimetric signatures*, respectively. Also, note that, provided that there is a suitably-high range resolution and assuming an approximately flat terrain, it can be shown that [Teba 09]:

$$p_{\text{GB}} \cong p_{\text{GT}} \cong p_{\text{GC}} \tag{3.33}$$

Finally, it follows from (3.17) and (3.18) that, by letting p_{G} approximate any of the power distributions for GB, GT, and GC; and $p_{\text{CN}} = p_{\text{V}}$, equation (3.32) may be simplified to:

$$\underline{P}_{\text{pol}} = p_{\text{G}}\text{vec}\left(C_{\text{G}}\right)^T + p_{\text{V}}\text{vec}\left(C_{\text{V}}\right)^T \tag{3.34}$$

where p_{G} and p_{V} are, respectively, the cross-range power distributions of the ground and volume SMs; and C_{G} and C_{V} are their respective ground and volume polarimetric signatures.

3.3 Analysis of Polarimetric Signatures

A common approach to analyzing polarimetric signatures is to decompose their respective 3-by-3 covariance matrices by means of an eigendecomposition. Note that this method is applicable to any polarimetric signature, i.e., the input 3-by-3 covariance matrix can correspond to either C_{G} or C_{V}, as well as to either their sum C [see (3.19)] or any rearranged row of $\underline{P}_{\text{pol}}$. For this reason, this section will focus on C only. However, all definitions will be based on the assumption that the Pauli vector representation has been considered.

The eigendecomposition of C provides a description of the underlying SM by means of a sum of covariance matrices corresponding to 3 independent targets. This expansion can be written as follows:

$$C = \lambda_1 e_1 e_1^\dagger + \lambda_2 e_2 e_2^\dagger + \lambda_3 e_3 e_3^\dagger \tag{3.35}$$

where $\lambda_1 \geq \lambda_2 \geq \lambda_3$ are nonnegative eigenvalues; and e_1, e_2, and e_3 are the respective eigenvectors. From this decomposition, five rotation-invariant [see (3.11)] parameters can be derived [Clou 96, Clou 97], as listed below:

1) Eigenvalue probability $q_i \in [0, 1]$:

$$q_i = \frac{\lambda_i}{\lambda_1 + \lambda_2 + \lambda_3} \tag{3.36}$$

with $1 \leq i \leq 3$. This parameter measures the relative importance of each eigenvalue and so $q_1 + q_2 + q_3 = 1$.

2) Polarimetric entropy $Q_{\mathrm{E}} \in [0, 1]$:

$$Q_{\mathrm{E}} = -\sum_{i=1}^{3} q_i \log_3 q_i \tag{3.37}$$

If $Q_{\mathrm{E}} = 0$, the rank of C equals 1, which indicates a deterministic SM. If $Q_{\mathrm{E}} = 1$, the eigenvalues are equal, thus corresponding to a completely random SM.

3) Polarimetric anisotropy $Q_{\mathrm{A}} \in [0, 1]$:

$$Q_{\mathrm{A}} = \begin{cases} (\lambda_2 - \lambda_3) \,/\, (\lambda_2 + \lambda_3) & \text{if } Q_{\mathrm{E}} > 0 \\ 0 & \text{if } Q_{\mathrm{E}} = 0 \end{cases} \tag{3.38}$$

This parameter characterizes the difference between the second and third eigenvalues. Thus, it is able to discriminate high-entropy SMs.

4) Mean alpha angle $\alpha_{\text{mean}} \in [0, \pi/2]$:

$$\alpha_{\text{mean}} = \sum_{i=1}^{3} q_i \arccos |e_{i1}| \tag{3.39}$$

where e_{i1} denotes the first element of the ith eigenvector. The reference values are $\alpha_{\text{mean}} = 0$, $\alpha_{\text{mean}} = \pi/4$, and $\alpha_{\text{mean}} = \pi/2$; which indicate scattering from an isotropic surface (i.e., a single bounce), an oriented dipole, and an isotropic dihedral (i.e., a double bounce), respectively.

5) Maximum alpha angle $\alpha_{\text{max}} \in [0, \pi/2]$:

$$\alpha_{\text{max}} = \arccos |e_{11}| \tag{3.40}$$

This parameter is analyzed just like α_{mean}, only the dominant target is considered.

4 Sparsity-Based SAR Tomography

Image compression algorithms are able to convert large digital datasets into significantly smaller ones by applying an appropriate change of basis [Mall 09]. Once a sparsifying domain has been found, only the nonzero expansion coefficients are coded and stored. Since the original data are generally discarded, this raises the question of whether it is at all possible to directly sample in a compressed form—thus effectively reducing the sampling rate. In effect, this is of particular interest for imaging techniques such as SAR tomography, for which the number of measurements are limited and expensive. This chapter first reviews the conditions under which compressible signals can be measured and reconstructed from a reduced set of observations. Then, it thoroughly explores their application to SAR tomography of forested areas for both single-channel and polarimetric sensors. Since the goal is to develop estimators that allow for an accurate electromagnetic characterization of natural distributed scenes, much of the emphasis is placed on ensuring physical validity. Finally, a motivation for the use of sparsifying wavelet systems is provided.

4.1 Compressed Sensing

4.1.1 Single-Signal CS

Compressed Sensing (CS) is a sampling paradigm that allows for capturing a signal—at a rate significantly below the Nyquist one—by exploiting *sparse* representations [Cand 06a, Cand 06b, Dono 06, Bara 07]. In particular, a signal $f_0 \in \mathbb{C}^N$ is said to be K-sparse in an orthonormal basis $\Psi \in \mathbb{C}^{N\times N}$ if its projection $\alpha = \Psi f_0 \in \mathbb{C}^N$ has, at most, K nonzero elements. In turn, $f_0 = \Psi^\dagger \alpha$. Thus, CS proposes measuring such a signal f_0 by

collecting M linear measurements of the form $b_0 = A_0 f_0 + y_0$ or $b_0 = A_0 \Psi^\dagger \alpha + y_0 \in \mathbb{C}^M$, where $A_0 \in \mathbb{C}^{M \times N}$ is a sensing matrix with M much smaller than N, and $y_0 \in \mathbb{C}^M$ is a perturbation term. Also, the matrix $\Theta_0 = A_0 \Psi^\dagger \in \mathbb{C}^{M \times N}$, such that $b_0 = \Theta_0 \alpha + y_0$, is said to obey the *restricted isometry property* (RIP) of order K if there exists a constant $\delta_K \in (0, 1)$ such that

$$(1 - \delta_K) \|\alpha\|_2^2 \leq \|\Theta_0 \alpha\|_2^2 \leq (1 + \delta_K) \|\alpha\|_2^2 \tag{4.1}$$

holds for all K-sparse signals α. This property essentially requires that every set of, at most, K columns approximately behaves like an orthonormal system [Cand 05, Cand 06d]. As developed in [Cand 06c, Cand 08], if Θ_0 satisfies the RIP of order $2K$ with $\delta_{2K} < \sqrt{2} - 1$, then it is possible to recover α from the measurements b_0 by L_1-norm minimization:

$$\boxed{\min_{\widetilde{\alpha}} \|\widetilde{\alpha}\|_1 \text{ subject to } \|\Theta_0 \widetilde{\alpha} - b_0\|_2 \leq \varepsilon} \tag{4.2}$$

and the solution $\widetilde{\alpha}$ obeys:

$$\|\widetilde{\alpha} - \alpha\|_2 \leq C_0 \left\|\alpha - \alpha^K\right\|_1 / \sqrt{K} + C_1 \varepsilon \tag{4.3}$$

for some constant C_0 and C_1, where α^K is the signal α with all but the K largest components set to zero and $\varepsilon \geq \|y_0\|_2$ is an upper bound on the perturbation level. In other words, this means that the K largest nonzero elements are recovered in their correct location and that the error is proportional to the rest of the nonzero elements and the perturbation level. Finally, $\widetilde{f}_0$ is recovered by computing $\widetilde{f}_0 = \Psi^\dagger \widetilde{\alpha}$.

As a result of the previous discussion, emphasis should be placed on designing a matrix A_0 for a given Ψ such that $\Theta_0 = A_0 \Psi^\dagger$ satisfies the RIP with $\delta_{2K} < \sqrt{2} - 1$. To that end, let $\Upsilon \in \mathbb{C}^{N \times N}$ be an orthonormal matrix and $\mathcal{F} = \Upsilon \Psi^\dagger \in \mathbb{C}^{N \times N}$. Also, let the *coherence* of $\mathcal{F}$ be given by:

$$\mu_0(\mathcal{F}) = \sqrt{N} \max_{i,j} |\mathcal{F}_{i,j}| \in \left[1, \sqrt{N}\right] \tag{4.4}$$

which basically measures the largest correlation between the rows of Υ and Ψ [Cand 07].

Then, it can be shown [Cand 06d, Rude 08] that, if A_0 is constructed by taking

$$M = \mathcal{O}\left(\mu_0^2\left(\mathcal{F}\right) K \log^4 N\right) \tag{4.5}$$

sensing waveforms (i.e., rows) of Υ uniformly at random and renormalizing the columns so that they are unit-normed, then $\delta_{2K} < \sqrt{2} - 1$ holds with large probability.

4.1.2 L_1 Minimization in Action

This section aims to provide instructive insight as to why the L_1-norm is a suitable proxy for sparsity. For this purpose, an intuitive geometrical explanation will be given by means of a simple (noiseless) example. Also, it will be shown that it is possible to generalize this reasoning whereby a recovery guarantee—in the form of (4.3)—can be found.

Let $\Theta_0' \in \mathbb{R}^{2\times 3}$ be given by:

$$\Theta_0' = \begin{bmatrix} 0 & 1 & -1 \\ 1 & -1 & 0 \end{bmatrix} \tag{4.6}$$

with its null space defined as $\mathcal{N}\left(\Theta_0'\right) = \{h' \in \mathbb{R}^3 : \Theta_0' h' = 0\}$ and hence comprises scaled versions of the vector $[\ 1 \quad 1 \quad 1\ ]$. Then, take noiseless measurements of the form $b_0' = \Theta_0'\alpha'$, where α' is a 1-sparse signal in $\mathbb{R}^3$, e.g., $\alpha' = [\ 1 \quad 0 \quad 0\ ]$. Since it is then also true that $b_0' = \Theta_0'(h' + \alpha')$, there are infinitely many solutions corresponding to $\mathcal{S} = \mathcal{N}\left(\Theta_0'\right) + \alpha'$. This is commonly referred to as the *translated null space* $\mathcal{S}$ and has been indicated by the red line in Figure 4.1. Note, however, that only one solution lies on the vertical axis, which corresponds to the 1-sparse vector α'. Noticeably, due to the pointiness of the L_1-ball $\mathcal{B} = \{x_0 \in \mathbb{R}^3 : \|x_0\|_1 \leq 1\}$ (visualized as an octahedron in Figure 4.1), this coincides with the solution with the minimum L_1-norm, which can be found by:

$$\boxed{\min_{\widetilde{\alpha}'} \|\widetilde{\alpha}'\|_1 \text{ subject to } \Theta_0'\widetilde{\alpha}' = b_0'} \tag{4.7}$$

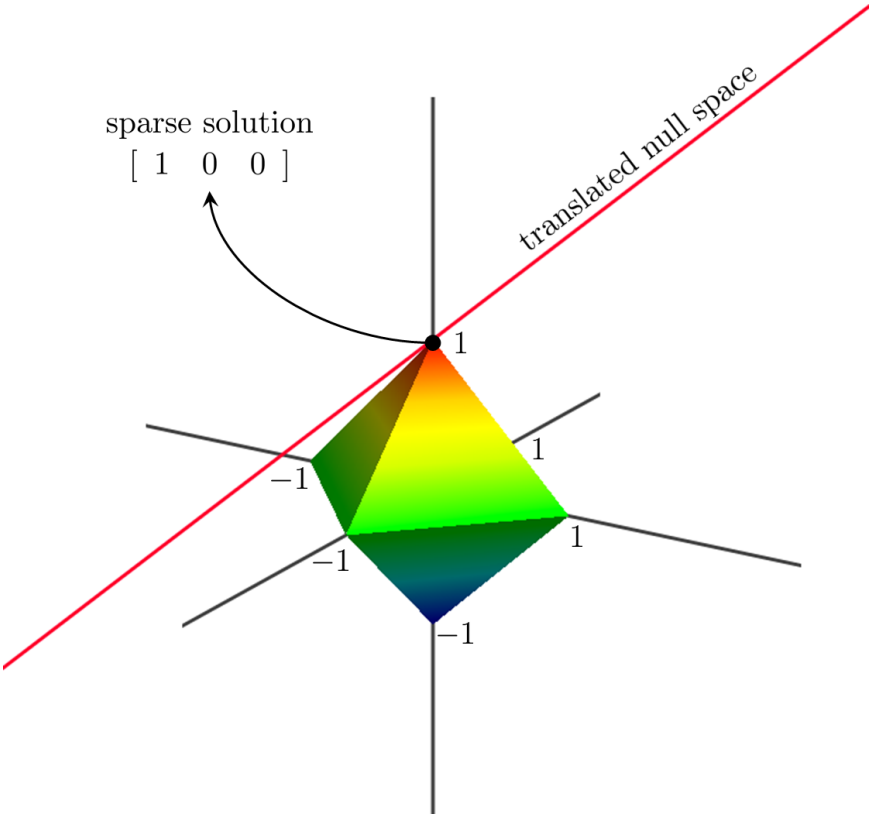

Figure 4.1: Visualization of L_1-norm minimization. The red line depicts the translated null space while the L_1-ball is visualized as an octahedron. The intersection coincides with the sparsest solution.

As is clear from Figure 4.1, the orientation of the null space (and hence the orientation of the red line) plays a crucial role in the process of singling out the right solution. In effect, provided the null space is not parallel to any of the faces or edges of the octahedron, a unique 1-sparse solution to (4.7) can be guaranteed. In particular, let h'_i represent the ith element of any vector h' in $\mathcal{N}\left(\Theta'_0\right)$ (excluding the zero vector). It then follows that the desired orientation can be achieved provided that [Forn 11]:

$$|h'_1| < |h'_2| + |h'_3| \tag{4.8}$$
$$|h'_2| < |h'_1| + |h'_3| \tag{4.9}$$
$$|h'_3| < |h'_1| + |h'_2| \tag{4.10}$$

which is clearly satisfied by Θ'_0 since, as previously pointed out, its null space is spanned by the vector $[\ 1 \quad 1 \quad 1\ ]$.

The previous considerations can be generalized and extended as follows. Consider noiseless measurements of the form $b_0 = \Theta_0\alpha$, where $b_0 \in \mathbb{C}^M$, $\alpha \in \mathbb{C}^N$, and $\Theta_0 \in \mathbb{C}^{M\times N}$. The matrix Θ_0 will be said to obey the *null space property* (NSP) of order K with constant $\delta_{\text{NSP}} \in (0,1)$ if

$$\|h_\Lambda\|_1 \leq \delta_{\text{NSP}} \|h_{\Lambda^c}\|_1 \tag{4.11}$$

where Λ is an arbitrary index subset of $\{1,2,\ldots,N\}$ such that $\#\Lambda \leq K$, i.e., the cardinality of Λ is less than or equal to K; Λ^c indicates the complement of Λ; $h \in \mathbb{C}^N$ is any vector in the null space of Θ_0; and h_Λ and h_{Λ^c} are vectors in $\mathbb{C}^N$ that coincide with h for the indices given by Λ and Λ^c, respectively, and are zero otherwise [Forn 11]. Moreover, let Θ_0 satisfy the NSP of order K and $\widetilde{\alpha} \in \mathbb{C}^N$ be the solution to (4.7). Then, $\widetilde{\alpha}$ obeys:

$$\|\alpha - \widetilde{\alpha}\|_1 \leq \frac{2\,(1+\delta_{\text{NSP}})}{1-\delta_{\text{NSP}}} \left\|\alpha - \alpha^K\right\|_1 \tag{4.12}$$

which is yet another recovery guarantee analogous to (4.3) [Forn 11]. The following proof adopts the strategy followed in [Forn 11] and is intended to provide further insight.

Proof. Since

$$\Theta\alpha - \Theta\widetilde{\alpha} = 0 = \Theta\,(\alpha - \widetilde{\alpha}) \tag{4.13}$$

it follows that $h = \alpha - \widetilde{\alpha}$ is in the null space of Θ. Also, because $\widetilde{\alpha}$ is found by (4.7), it must be true that:

$$\|\widetilde{\alpha}\|_1 \leq \|\alpha\|_1 \tag{4.14}$$

$$\|\widetilde{\alpha}_\Lambda\|_1 + \|\widetilde{\alpha}_{\Lambda^c}\|_1 \leq \|\alpha_\Lambda\|_1 + \|\alpha_{\Lambda^c}\|_1 \tag{4.15}$$

which, by the fact that $\widetilde{\alpha} = \alpha - h$, leads to the following inequalities:

$$\begin{aligned} \|\alpha_\Lambda - h_\Lambda\|_1 + \|\alpha_{\Lambda^c} - h_{\Lambda^c}\|_1 &\leq \|\alpha_\Lambda\|_1 + \|\alpha_{\Lambda^c}\|_1 && (4.16)\\ \|\alpha_\Lambda - h_\Lambda\|_1 + \|-\alpha_{\Lambda^c} + h_{\Lambda^c}\|_1 &\leq \|\alpha_\Lambda\|_1 + \|\alpha_{\Lambda^c}\|_1 && (4.17)\\ \|\alpha_\Lambda\|_1 - \|h_\Lambda\|_1 - \|\alpha_{\Lambda^c}\|_1 + \|h_{\Lambda^c}\|_1 &\leq \|\alpha_\Lambda\|_1 + \|\alpha_{\Lambda^c}\|_1 && (4.18) \end{aligned}$$

where the last inequality follows from the reverse triangle inequality. Hence,

$$\|h_{\Lambda^c}\|_1 \leq \|h_\Lambda\|_1 + 2\,\|\alpha_{\Lambda^c}\|_1 \tag{4.19}$$

which, by the NSP, gives:

$$\begin{aligned} \|h_{\Lambda^c}\|_1 &\leq \delta_{\text{NSP}}\,\|h_{\Lambda^c}\|_1 + 2\,\|\alpha_{\Lambda^c}\|_1 && (4.20)\\ \|h_{\Lambda^c}\|_1 &\leq \frac{2}{1-\delta_{\text{NSP}}}\,\|\alpha_{\Lambda^c}\|_1 && (4.21) \end{aligned}$$

Finally, since

$$\|\alpha - \widetilde{\alpha}\|_1 = \|h\|_1 = \|h_\Lambda\|_1 + \|h_{\Lambda^c}\|_1 \tag{4.22}$$

and, by the NSP,

$$\begin{aligned} \|h_\Lambda\|_1 + \|h_{\Lambda^c}\|_1 &\leq \delta_{\text{NSP}}\,\|h_{\Lambda^c}\|_1 + \|h_{\Lambda^c}\|_1 && (4.23)\\ \|h_\Lambda\|_1 + \|h_{\Lambda^c}\|_1 &\leq (1+\delta_{\text{NSP}})\,\|h_{\Lambda^c}\|_1 && (4.24) \end{aligned}$$

it follows from (4.21) that:

$$\|h_\Lambda\|_1 + \|h_{\Lambda^c}\|_1 \leq \frac{2\,(1+\delta_{\text{NSP}})}{1-\delta_{\text{NSP}}}\,\|\alpha_{\Lambda^c}\|_1 \tag{4.25}$$

and hence, from (4.22),

$$\|\alpha - \widetilde{\alpha}\|_1 \leq \frac{2\,(1+\delta_{\text{NSP}})}{1-\delta_{\text{NSP}}}\,\|\alpha_{\Lambda^c}\|_1 \tag{4.26}$$

which completes the proof.

4.1.3 Multi-Signal CS

Multi-signal CS enables the joint recovery of signal ensembles by exploiting inter-signal structural correlations. It generalizes the concept of a signal being sparse to the concept of an ensemble of signals being *jointly sparse* [Baro 09, Elda 10]. In particular, it proposes taking linear measurements of the form $B = A_0 X + Y$, where $X \in \mathbb{C}^{N \times L}$ indicates L sparse signals that exhibit common support (i.e., X is row-sparse), $A_0 \in \mathbb{C}^{M \times N}$ is a sensing matrix with $M < N$, and $Y \in \mathbb{C}^{M \times L}$ is an unknown perturbation term. The corresponding reconstruction is achieved by the following convex optimization—which is the multi-signal analog of (4.2):

$$\boxed{\min_{\widetilde{X}} \left\| \widetilde{X} \right\|_{2,1} \text{ subject to } \left\| A_0 \widetilde{X} - B \right\|_{\mathrm{F}} \leq \varepsilon} \tag{4.27}$$

where ε is an upper bound on the perturbation level, $\|\cdot\|_{\mathrm{F}}$ is the Frobenius matrix norm, and $\|\cdot\|_{2,1}$ is a mixed norm (sum of the L_2-norms of the rows of a matrix) that promotes row-sparsity.

In general, the reconstruction approach given by (4.27) is known to perform better than L independent instances of (4.2) (see, for example, [Elda 09, Elda 10, Agui 12a]). Nonetheless, in order to provide a joint treatment of sensing considerations for the single- and multi-signal cases, the sampling requirements will be henceforth assumed to be determined as if each of the signals were to be reconstructed separately.

4.2 CS for SAR Tomography

4.2.1 Single-Channel CS

SAR sensors that operate using a single polarimetric channel allow for the estimation of only one of the main diagonal blocks in (3.27), i.e., either $K_{\text{HH–HH}}$, $K_{\text{VV–VV}}$, or $K_{\text{HV–HV}}$. As a result, the corresponding reduced covariance matrix model is given by considering either the 1st, 5th, or 9th column of $\underline{K}_{\text{pol}}$ and $\underline{P}_{\text{pol}}$ in (3.31). From (3.28) and (3.29),

this model can be written as:

$$\mathrm{vec}\,(K_i) = \Phi p_i \tag{4.28}$$

or

$$k_i = \Phi p_i \tag{4.29}$$

where i corresponds to either HH–HH, VV–VV, or HV–HV.

By considering equations (4.29) and (4.2) together, the cross-range power estimation can be readily recast as an instance of CS. Once an appropriate sparsifying basis $\Psi \in \mathbb{R}^{n\times n}$ has been chosen, the reconstruction of p_i can be formulated as the following convex optimization:

$$\boxed{\min_{\widetilde{p}_i} \|\Psi\,\widetilde{p}_i\|_1 \text{ subject to } \left\|\Phi\widetilde{p}_i - \widehat{k}_i\right\|_2 \leq \varepsilon} \tag{4.30}$$

where $\widehat{k}_i$ is the rearranged sample covariance matrix and ε can be used to control the trade-off between sparsity in Ψ and model mismatch. In accordance with the definition of p_i, the optimization has to be carried out over the set of nonnegative real numbers [Agui 13c]. As will be demonstrated in Chapter 7.1, this approach has considerable ambiguity-rejection capabilities and has the ability to recover the complete cross-range power with few highly irregular passes. Also, it will be noted that, unlike FB and CB, CS requires an appropriate definition of the cross-range extent inherently modeled by p_i.

Since, by construction, Φ behaves like a partial Fourier matrix [see (3.30)], the coherence of $\mathcal{F} = \Upsilon\Psi^\dagger$, as defined by (4.4), ought to be computed by letting Υ be a Fourier matrix. In addition, note that (4.30) implies a nonlinear reconstruction. Therefore, radiometric accuracy might be incurred which, as denoted by (4.3), will be bounded by both ε and the sparsity level. Thus, whereas the former is directly related to any source of decorrelation [Baml 98, Hans 01] as well as to the number of looks that were used to compute the rearranged sample covariance matrix $\widehat{k}_i$, the latter translates into the number of effective unknowns, i.e., the coefficients that sparsely represent p_i.

Finally, note that it is common to use (4.30) in penalized form, along with an additional total-variation (TV) norm regularization [Yang 10], which results in [Agui 13c]:

$$\min_{\widetilde{p}_i} \; \|\Psi\,\widetilde{p}_i\|_1 + \tau_1 \left\|\Phi\widetilde{p}_i - \widehat{k}_i\right\|_2^2 + \tau_2 \|\widetilde{p}_i\|_{\text{TV}} \tag{4.31}$$

with

$$\|\widetilde{p}_i\|_{\text{TV}} = \sum_{r=2}^{n} |\widetilde{p}_i\,[r] - \widetilde{p}_i\,[r-1]| \tag{4.32}$$

where $|\cdot|$ denotes the absolute value; and the parameters τ_1 and τ_2 control the trade-off between sparsity in Ψ, model mismatch, and TV. Essentially, $\|\cdot\|_{\text{TV}}$ enables the introduction of prior knowledge about the fact that the nonzero elements of p_i tend to appear in groups (see Section 4.3.2), thereby exploiting the ordering of the features in p_i [Tibs 05].

4.2.2 Polarimetric CS

As observed in Section 3.2, forested areas are generally dominated by two effective SMs. Thus, if there exists a sparsifying basis $\Psi \in \mathbb{R}^{n\times n}$ for p_{G} and p_{V} in (3.34), it follows that $\underline{P}_{\text{pol}}$ can be represented by a row-sparse matrix $\Theta \in \mathbb{C}^{n\times 9}$, such that $\underline{P}_{\text{pol}} = \Psi^{\text{T}}\Theta$. Consequently, the reconstruction of Θ can be directly cast as an instance of (4.27) as follows:

$$\min_{\widetilde{\Theta}} \left\|\widetilde{\Theta}\right\|_{2,1} \text{ subject to } \left\|\Phi\Psi^{\text{T}}\widetilde{\Theta} - \underline{\widehat{K}}_{\text{pol}}\right\|_{\text{F}} \leq \varepsilon \tag{4.33}$$

where $\underline{\widehat{K}}_{\text{pol}}$ is the sample version of $\underline{K}_{\text{pol}}$ and ε is an upper bound on the model mismatch that potentially captures any source of decorrelation as well as an insufficient level of multi-looking. In turn, this would yield $\underline{\widetilde{P}}_{\text{pol}} = \Psi^{\text{T}}\widetilde{\Theta}$. Although intuitive and simple, this approach falls short of ideal, in that it ignores the inherent properties and low dimensionality of the subspace of the polarimetric signatures C_{G} and C_{V}.

As a stepping-stone toward a robust formulation note that, under the assumptions introduced in Section 3.2, (3.31) and (3.34) imply that the rank of $\underline{K}_{\text{pol}}$ should be less than or equal to 2. In practice, however, the hypothesis of invariance of the power distribution with respect to the choice of polarimetric channel might not hold. As a result, the rank of $\underline{K}_{\text{pol}}$ could turn out to be greater than 2 [Teba 10a]. Incidentally, the required dimensionality, and hence the number of effective SMs, can be readily enforced by computing the best rank-2 approximation of $\underline{K}_{\text{pol}}$. This approximation, which can be obtained by means of a singular-value decomposition (SVD) [Teba 09], will be denoted with $\underline{K}^2_{\text{pol}}$. Of equal importance is the fact that the outer-product structure of (3.34) implies that the adjoint of the corresponding right-singular vectors defines an orthonormal basis for the unknown polarimetric signatures C_{G} and C_{V} [Teba 09] (see also [Bijm 05, Merc 09]). As a result, if $\underline{K}^2_{\text{pol}}$ is considered, it follows that every row of $\underline{P}_{\text{pol}}$ will be bound to lie in a 2-D subspace. Thus, once the right-singular vectors v_1 and $v_2 \in \mathbb{C}^9$—whose conjugates span the polarimetric space—have been obtained and a matrix $V \in \mathbb{C}^{2\times 9}$

$$V = \begin{bmatrix} v_1^\dagger \\ v_2^\dagger \end{bmatrix} \tag{4.34}$$

has been formed, a data-adaptive reconstruction can be formulated as follows:

$$\boxed{\min_{\widetilde{\Omega}} \left\| \widetilde{\Omega} \right\|_{2,1} \text{ subject to } \left\| \Phi \Psi^{\text{T}} \widetilde{\Omega} V - \widehat{\underline{K}}^2_{\text{pol}} \right\|_{\text{F}} \leq \varepsilon} \tag{4.35}$$

where $\widetilde{\Omega} \in \mathbb{R}^{n\times 2}$, which stems from the fact that hermitian matrices form a vector space only over the real numbers. Just as in (4.33), ε is an upper bound on the model mismatch. Then, $\widetilde{\underline{P}}_{\text{pol}} = \Psi^{\text{T}} \widetilde{\Omega} V$. In order to ensure physical validity, proper constraints must be set so that every row of $\widetilde{\underline{P}}_{\text{pol}}$ (when rearranged in a 3-by-3 matrix) results in a positive-semidefinite matrix. To this end, let $V_i \in \mathbb{C}^{3\times 3}$ and $\widetilde{\underline{P}}_{\text{pol}_j} \in \mathbb{C}^{3\times 3}$ be the result of rearranging $v_i^\dagger$ and $\widetilde{p}_{\text{pol}_j} \in \mathbb{C}^9$ (a vector corresponding to the jth row of $\widetilde{\underline{P}}_{\text{pol}}$) into 3-by-3 matrices, respectively. Since it is possible to find a matrix G that jointly diagonalizes V_1 and V_2 (see, for example, [Teba 09]), it follows that $G^\dagger \widetilde{\underline{P}}_{\text{pol}_j} G$ is certain to be diagonal. Furthermore, the corresponding main diagonal entries can be alternatively computed by $\dot{M} \widetilde{p}_{\text{pol}_j}$, where $\dot{M} \in \mathbb{C}^{3\times 9}$ is formed from $G^\dagger$ and G. Then, the required positive semidefiniteness can be enforced by adding a constraint of the form

$\dot{M}(\Psi^{\mathrm{T}}\widetilde{\Omega}V)^{\mathrm{T}} \succeq 0$ [Agui 13a], which ensures element-wise nonnegativity.

Interestingly, this approach can be understood from a slightly different, yet instructive, viewpoint. Specifically, rather than considering $\underline{P}_{\mathrm{pol}}$ to be composed of nine 1-D signals (column vectors), it can be thought of as *one* 2-D signal. As a result, $\underline{P}_{\mathrm{pol}}$ can be represented in a 2-D basis, readily formed by computing the outer product of all 1-D basis vectors for Ψ and all 1-D polarimetric signature basis vectors, i.e., a Kronecker basis. Thus, just as the former allows for a sparse expansion of the cross-range backscattered power, the latter provides a sparse expansion of the polarimetric signature. However, since only two SMs are considered, the support of the polarimetric signature transform coefficients is known *a priori*. Consequently, if $\ell \ll n$ is the size of the union of the supports of the two cross-range power distributions p_{G} and p_{V} (in the Ψ domain), then the number of nonzero (real-valued) transform coefficients reduces to 2ℓ. Also note that, from this perspective, Φ is bound to take *partitioned measurements*, in that only one column is measured at a time. For further details on this kind of distributed sensing setting, the reader is referred to [Duar 12].

For the sake of completeness, the possibility of the existence of more than two independent SMs (i.e., SMs with both linearly independent power distributions and linearly independent polarimetric signatures) will be considered. To this end, first assume that all the hypotheses thus far considered hold true. It then follows from the outer-product structure of (3.34) that relying on the best rank-2 approximation of $\underline{K}_{\mathrm{pol}}$ will limit the analysis to only two SMs [Teba 09]. Hence, a full-rank formulation is of interest. However, were the condition of power-distribution invariance not to hold, such a full-rank approach would be unable to enforce this condition *a priori*. Consequently, this violation must be captured in the form of an additive perturbation. With this in mind, a full-rank reconstruction can be accomplished via the following convex optimization:

$$\begin{aligned} \min_{\widetilde{\underline{P}}_{\mathrm{pol}}} \left\| \Psi \widetilde{\underline{P}}_{\mathrm{pol}} \right\|_{2,1} \quad & \text{subject to} \\ & \left\| \Phi \widetilde{\underline{P}}_{\mathrm{pol}} - \widehat{\underline{K}}_{\mathrm{pol}} \right\|_{\mathrm{F}} \leq \varepsilon \\ & \text{and} \\ & \widetilde{\underline{P}}_{\mathrm{pol}_j} \in \mathbb{H}^3_+ \quad \text{for all} \quad 1 \leq j \leq n \end{aligned} \tag{4.36}$$

where $\underline{\widetilde{P}}_{\text{pol}_j} \in \mathbb{C}^{3\times 3}$ is the result of rearranging the jth row of $\underline{\widetilde{P}}_{\text{pol}}$ into a 3-by-3 matrix, $\mathbb{H}^3_+$ denotes the cone of hermitian positive-semidefinite 3-by-3 matrices [Boyd 04], and ε is an upper bound on the perturbation size. The resulting penalized form is given by:

$$\min_{\underline{\widetilde{P}}_{\text{pol}}} \tau \left\| \Psi \underline{\widetilde{P}}_{\text{pol}} \right\|_{2,1} + \left\| \Phi \underline{\widetilde{P}}_{\text{pol}} - \underline{\widehat{K}}_{\text{pol}} \right\|_{\text{F}}^2 \text{ subject to } \underline{\widetilde{P}}_{\text{pol}_j} \in \mathbb{H}^3_+ \text{ for all } 1 \leq j \leq n \tag{4.37}$$

where τ trades row-sparsity for data mismatch.

4.3 Sparse Representations for Forested Areas

4.3.1 Wavelet Systems

An orthogonal wavelet system is generally regarded as a set of functions used for uniquely representing a signal. When formulated from a multi-resolution perspective, these functions can be divided into two classes, namely, scaling and wavelet functions, that represent coarse and fine information, respectively. Thus, the discrete wavelet transform (DWT) of a signal $\vartheta(\varsigma)$ for a given integer scale j_0 computes the coefficients c_{j_0} and d_j—at k integer shifts—as follows [Burr 98]:

$$c_{j_0}(k) = \int \vartheta(\varsigma)\, \varphi_{j_0,k}(\varsigma)\, d\varsigma \tag{4.38}$$

$$d_j(k) = \int \vartheta(\varsigma)\, \psi_{j,k}(\varsigma)\, d\varsigma \tag{4.39}$$

where $j \in [j_0, +\infty)$; $k \in (-\infty, +\infty)$; and $\varphi_{j_0,k}(\varsigma)$ and $\psi_{j,k}(\varsigma)$ are the family of functions given by:

$$\varphi_{j_0,k}(\varsigma) = 2^{j_0/2} \varphi\left(2^{j_0}\varsigma - k\right) \tag{4.40}$$

$$\psi_{j,k}(\varsigma) = 2^{j/2} \psi\left(2^{j}\varsigma - k\right) \tag{4.41}$$

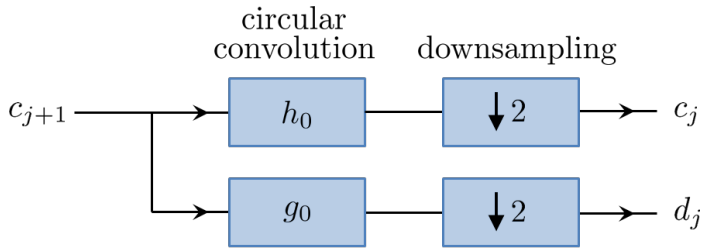

Figure 4.2: Block diagram of the computation of the wavelet coefficients d_j and the scaling coefficients c_j from the scaling coefficients c_{j+1}. The blocks corresponding to h_0 and g_0 are assumed to implement the required time-reversal.

where $\varphi(\varsigma)$ and $\psi(\varsigma)$ are, respectively, basic scaling and wavelet functions of choice [Burr 98, Mall 09]. Then, $\vartheta(\varsigma)$ can be recovered from:

$$\vartheta(\varsigma) = \sum_k c_{j_0}(k)\,\varphi_{j_0,k}(\varsigma) + \sum_k \sum_{j=j_0}^{+\infty} d_j(k)\,\psi_{j,k}(\varsigma) \tag{4.42}$$

Incidentally, expansion coefficients at a given scale can be shown to define those at a lower scale as follows [Burr 98, Mall 09]:

$$c_j(k) = \sum_m h_0(m-2k)\,c_{j+1}(m) \tag{4.43}$$

$$d_j(k) = \sum_m g_0(m-2k)\,c_{j+1}(m) \tag{4.44}$$

where h_0 and g_0 are known as the (low-pass) scaling and the (high-pass) wavelet filters, respectively. This leads to the common practice of interpreting the samples $\vartheta(n)$, with $1 \leq n \leq N$, of a signal $\vartheta(\varsigma)$ as scaling coefficients at an arbitrary scale $j+1$ such that $\vartheta(n) = c_{j+1}(n)$. Thus, (4.43) and (4.44) can be used to compute the wavelet coefficients d_j and the scaling coefficients c_j. Figure 4.2 shows a block diagram of the resulting filtering and downsampling operation, where $\vartheta(n)$ has been assumed to be a periodic signal with period N—and hence the circular convolution. Also, note that the blocks corresponding to h_0 and g_0 are assumed to implement the required time-reversal.

When these steps are applied ℓ times in a cascaded fashion, the resulting operation is said to compute the DWT with ℓ *levels of decomposition*. From an operational standpoint, if $\vartheta(n)$ represents scaling coefficients at scale $j+1$, then computing an ℓ-level DWT

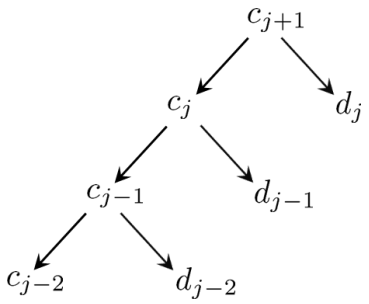

Figure 4.3: Expansion coefficients resulting from 3 levels of decomposition. The leaves of the tree provide the 3-level DWT.

will yield scaling coefficients at scale $j + 1 - \ell$ and wavelet coefficients from scale $j + 1 - \ell$ up to j. Figure 4.3 illustrates the intermediate and final expansion coefficients for $\ell = 3$, where the leaves of the tree provide the 3-level DWT. Also, note that, from the assumption of periodicity, it follows that an ℓ-level DWT can be implemented as an orthonormal transform defined by an N-by-N matrix Ψ, whose inverse is readily found by its transpose [Mall 09].

Finally, a wavelet is said to have v_{m} vanishing moments if it is orthogonal to polynomials of degree $v_{\mathrm{m}} - 1$ [Mall 09]. Hence, if $\vartheta(\varsigma)$ exhibits such a polynomial behavior, all its wavelet coefficients $d_j\,(k)$ will be zero which, in turn, implies that $\vartheta\,(\varsigma)$ will be fully captured by the scaling coefficients $c_{j_0}\,(k)$. As a result, if $\vartheta\,(\varsigma)$ has few isolated singularities and is very regular, a wavelet with many vanishing moments should be chosen in order to achieve a sparse expansion. On the contrary, if the number of singularities increases—which results in high-amplitude coefficients due to the overlap between the chosen wavelets and these singularities—the size of the wavelet support should be decreased. Unfortunately, this is achieved at the expense of reducing the number of vanishing moments. That being said, there is a trade-off between the number of vanishing moments and the support size [Mall 09].

4.3.2 Wavelets for SAR Tomography

As a consequence of equation (4.5), the choice of an orthonormal basis Ψ requires some special consideration. First, Ψ should generate a sparse expansion. Second, the coherence between the measurement basis Υ and the sparsity basis Ψ should be as small as possible. This section proposes a sparsifying basis that is in line with these two requirements [Agui 13c].

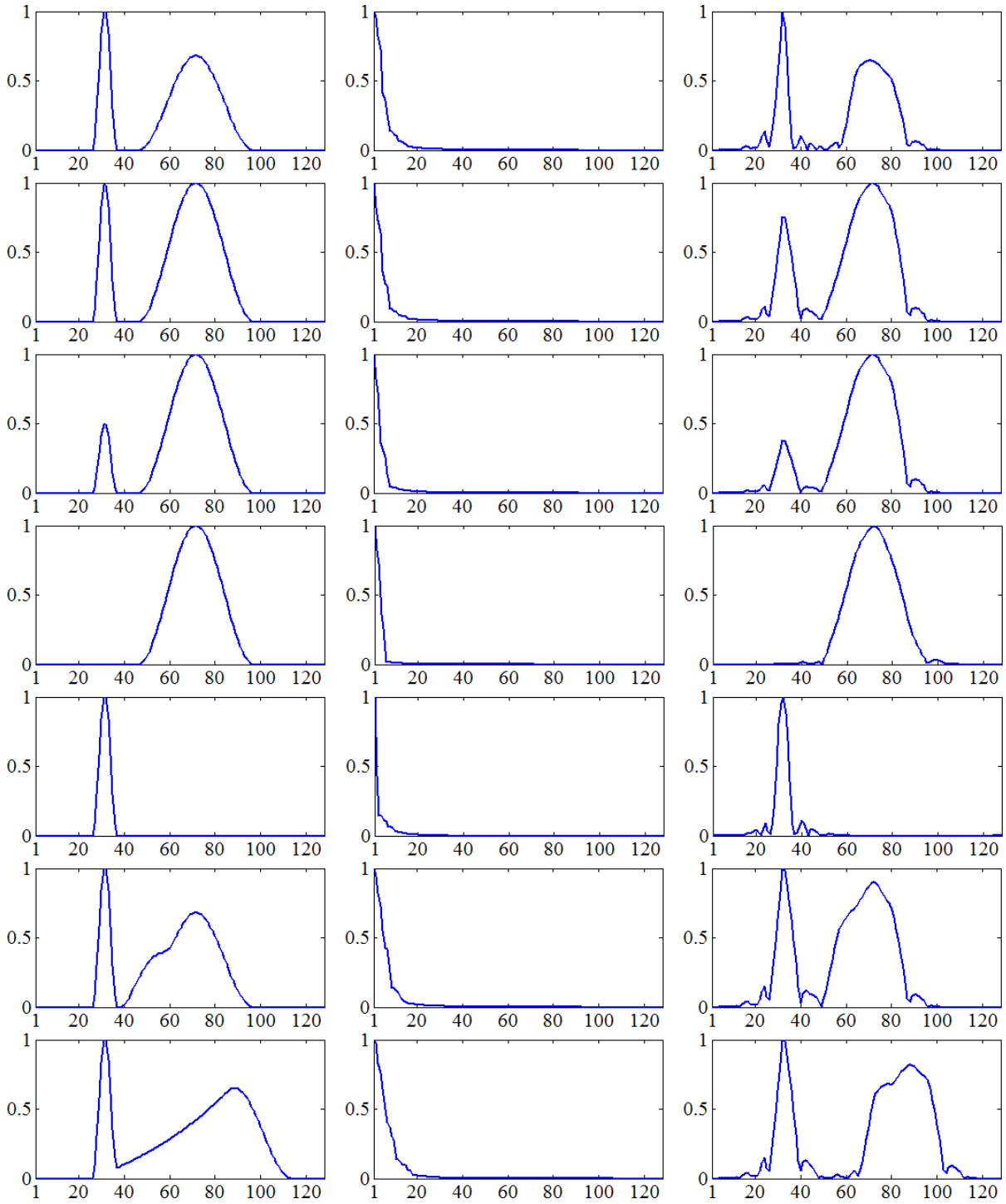

Figure 4.4: Sparsity in the wavelet domain. (Left column) Power distribution (as a function of height with $n = 128$) of typical cross-range profiles encountered over forested terrain. (Middle column) Sorted magnitudes of the transform coefficients using a Daubechies Symmlet wavelet with 4 vanishing moments and 3 levels of decomposition. (Right column) Magnitude of the inverse DWT after zeroing out all but the 5 largest coefficients. All plots have been normalized.

As developed in Section 3.2, cross-range profiles over forested terrain follow, in general, a very simple two-component structure. Specifically, one of these components accounts for a ground SM whereas the other accounts for a volume SM. Interestingly, their respective power distributions are quite regular, thereby giving rise to sparse representations in the wavelet domain [Agui 13c]. By way of illustration, the left column of the plots in Figure 4.4 shows several commonly-encountered power distributions [Teba 12, Agui 13c]. In addition, the middle column displays the rapid decay of the sorted magnitudes of the corresponding transform coefficients, which were computed using Daubechies Symmlet wavelets with 4 vanishing moments and 3 levels of decomposition. Finally, the right column presents the magnitude of the inverse DWT, after zeroing out all but the 5 largest transform coefficients. Clearly, the profiles are very well approximated. In this respect, the choice of Symmlets can be justified by noting that, besides yielding good results in practice, they are optimal in the sense that they have minimum support for a given number of vanishing moments [Burr 98, Mall 09].

Lastly, in order to generate the maximum number of small wavelet coefficients, it might seem tempting to use a Ψ that computes many levels of decomposition. However, more levels of decomposition lead to a higher coherence. For example, 4 levels result in $\mu_0 = 4.0$, 3 levels result in $\mu_0 = 2.8284$, while 2 levels in $\mu_0 = 2.0$.

5 Separation of SMs via Convex Optimization

This chapter develops the fundamentals of algebraic SM separation—originally introduced in [Teba 09]—and proposes a convex optimization approach to achieving such separation. The basic idea is to filter out the cross-range power distributions and polarimetric signatures of the ground and volume SMs (see Section 3.2) so that they can be subsequently evaluated separately. Specifically, while their spatial distributions can then be determined via tomographic techniques such as FB, CB, and/or CS, their polarimetric signatures can be analyzed in terms of eigendecomposition-based parameters (see Section 3.3). The difficulty, however, lies in the fact that the filtering procedure is required to ensure positive semidefiniteness of the resulting matrices, i.e., physical validity. As will be developed, this can be accomplished by restricting the analysis to the cone of hermitian positive-semidefinite matrices [Boyd 04].

The outer-product model outlined in Section 3.2 will serve as a starting point. First, note that, as follows from (3.31) and (3.34), $\underline{K}_{\text{pol}}$ can be written as:

$$\begin{aligned} \underline{K}_{\text{pol}} &= \Phi p_{\text{G}} \text{vec}\,(C_{\text{G}})^T + \Phi p_{\text{V}} \text{vec}\,(C_{\text{V}})^T && (5.1)\\ &= k_{\text{G}} \text{vec}\,(C_{\text{G}})^T + k_{\text{V}} \text{vec}\,(C_{\text{V}})^T && (5.2)\\ &= \text{vec}\,(K_{\text{G}})\,\text{vec}\,(C_{\text{G}})^T + \text{vec}\,(K_{\text{V}})\,\text{vec}\,(C_{\text{V}})^T && (5.3) \end{aligned}$$

where K_{G} and $K_{\text{V}} \in \mathbb{C}^{m\times m}$ are ground and volume covariance matrices (usually referred to as *structure matrices* [Teba 09]), respectively, which can be exploited by the

tomographic techniques introduced in Sections 2.4 and 4.2.1[1]. Then, the SVD of $\underline{K}_{\text{pol}}$ must be given by:

$$\underline{K}_{\text{pol}} = \left[\begin{array}{cc} w_1 & w_2 \end{array} \right] \left[\begin{array}{c} \sigma_1 v_1^{\dagger} \\ \sigma_2 v_2^{\dagger} \end{array} \right] \tag{5.4}$$

where $\sigma_1 \geq \sigma_2$ are nonnegative singular values; w_1 and $w_2 \in \mathbb{C}^{m^2}$ are, respectively, the first and second left-singular vectors; and v_1 and $v_2 \in \mathbb{C}^9$ are, respectively, the first and second right-singular vectors. Next, given an invertible matrix

$$A_{\text{SMs}} = \left[\begin{array}{cc} \dot{a} & \dot{b} \\ \dot{c} & \dot{d} \end{array} \right] \in \mathbb{R}^{2\times 2} \tag{5.5}$$

it follows that:

$$\underline{K}_{\text{pol}} = \left[\begin{array}{cc} w_1 & w_2 \end{array} \right] A_{\text{SMs}} A_{\text{SMs}}^{-1} \left[\begin{array}{c} \sigma_1 v_1^{\dagger} \\ \sigma_2 v_2^{\dagger} \end{array} \right] \tag{5.6}$$

which, by considering (5.3), leads to:

$$\text{vec}\,(K_{\text{G}}) = \dot{a} w_1 + \dot{c} w_2 \tag{5.7}$$

$$\text{vec}\,(K_{\text{V}}) = \dot{b} w_1 + \dot{d} w_2 \tag{5.8}$$

Note, however, that the interpretation of the elements of K_{G} and K_{V} as correlation coefficients [Baml 98, Hans 01] requires that the respective diagonal elements be equal to 1. Incidentally, this can be readily enforced by letting

$$\overline{w}_1 = w_1 / w_{11} \tag{5.9}$$

$$\overline{w}_2 = w_2 / w_{21} \tag{5.10}$$

[1] Observe that (5.3) is equivalent to the well-known sum of Kronecker products (SKP) given by [Teba 09]:

$$K_{\text{pol}} = C_{\text{G}} \otimes K_{\text{G}} + C_{\text{V}} \otimes K_{\text{V}}$$

and

$$\dot{c} = 1 - \dot{a} \tag{5.11}$$
$$\dot{d} = 1 - \dot{b} \tag{5.12}$$

where w_{i1} denotes the first element of the ith left-singular vector. This, in turn, results in:

$$\text{vec}\,(K_{\text{G}}) = \dot{a}\overline{w}_1 + (1-\dot{a})\overline{w}_2 \tag{5.13}$$
$$\text{vec}\,(K_{\text{V}}) = \dot{b}\overline{w}_1 + (1-\dot{b})\overline{w}_2 \tag{5.14}$$

Accordingly, vec (C_{G}) and vec (C_{V}) must be given by:

$$\text{vec}\,(C_{\text{G}}) = \frac{1}{\dot{a}-\dot{b}}\Big((1-\dot{b})\overline{v}_1 - \dot{b}\overline{v}_2\Big) \tag{5.15}$$
$$\text{vec}\,(C_{\text{V}}) = \frac{1}{\dot{a}-\dot{b}}\Big(-(1-\dot{a})\overline{v}_1 + \dot{a}\overline{v}_2\Big) \tag{5.16}$$

with

$$\overline{v}_1 = w_{11}\sigma_1 \text{conj}\,(v_1) \tag{5.17}$$
$$\overline{v}_2 = w_{21}\sigma_2 \text{conj}\,(v_2) \tag{5.18}$$

Thus, the aforementioned considerations can be equivalently summarized into the following expression:

$$K_{\text{G}} = \dot{a}\overline{W}_1 + (1-\dot{a})\overline{W}_2 \tag{5.19}$$
$$K_{\text{V}} = \dot{b}\overline{W}_1 + (1-\dot{b})\overline{W}_2 \tag{5.20}$$
$$C_{\text{G}} = \frac{1}{\dot{a}-\dot{b}}\Big((1-\dot{b})\overline{V}_1 - \dot{b}\overline{V}_2\Big) \tag{5.21}$$
$$C_{\text{V}} = \frac{1}{\dot{a}-\dot{b}}\Big(-(1-\dot{a})\overline{V}_1 + \dot{a}\overline{V}_2\Big) \tag{5.22}$$

where $\overline{W}_1$ and $\overline{W}_2 \in \mathbb{C}^{m\times m}$ are the rearranged versions of $\overline{w}_1$ and $\overline{w}_2$, respectively. Likewise, $\overline{V}_1$ and $\overline{V}_2 \in \mathbb{C}^{3\times 3}$ are the rearranged versions of $\overline{v}_1$ and $\overline{v}_2$, respectively.

As a result of the previous derivations, the problem of SM separation is equivalent to the problem of finding two real numbers $\dot{a}$ and $\dot{b}$ subject to the constraint of positive semidefiniteness, i.e., physical validity. A detailed discussion on the possible choices of these parameters can be found in [Teba 12], where the authors show the robustness of this approach for estimating ground and treetop elevations [Teba 12]. While the methodology originally proposed in [Teba 09] resorts to joint-diagonalization techniques, this dissertation takes a convex optimization approach that enables a direct computation of $\dot{a}$ and $\dot{b}$. Specifically, the minimum allowed values for $\dot{a}$ and $\dot{b}$ will be retrieved by:

$$\begin{aligned}
&\min_{\widetilde{a},\widetilde{b}} \ \widetilde{a}+\widetilde{b} \ \text{ subject to} \\
&\qquad \widetilde{a}\overline{W}_1+(1-\widetilde{a})\overline{W}_2 \quad \in \ \mathbb{H}_+^m \\
&\qquad \widetilde{b}\overline{W}_1+(1-\widetilde{b})\overline{W}_2 \quad \in \ \mathbb{H}_+^m \\
&\qquad (1-\widetilde{b})\overline{V}_1-\widetilde{b}\overline{V}_2 \quad \in \ \mathbb{H}_+^3 \\
&\qquad -(1-\widetilde{a})\overline{V}_1+\widetilde{a}\overline{V}_2 \quad \in \ \mathbb{H}_+^3
\end{aligned} \tag{5.23}$$

where $\mathbb{H}_+^m$ and $\mathbb{H}_+^3$ denote the cones of hermitian positive-semidefinite m-by-m and 3-by-3 matrices, respectively [Boyd 04]. Analogously, the maximum allowed values are given by:

$$\begin{aligned}
&\max_{\widetilde{a},\widetilde{b}} \ \widetilde{a}+\widetilde{b} \ \text{ subject to} \\
&\qquad \widetilde{a}\overline{W}_1+(1-\widetilde{a})\overline{W}_2 \quad \in \ \mathbb{H}_+^m \\
&\qquad \widetilde{b}\overline{W}_1+(1-\widetilde{b})\overline{W}_2 \quad \in \ \mathbb{H}_+^m \\
&\qquad (1-\widetilde{b})\overline{V}_1-\widetilde{b}\overline{V}_2 \quad \in \ \mathbb{H}_+^3 \\
&\qquad -(1-\widetilde{a})\overline{V}_1+\widetilde{a}\overline{V}_2 \quad \in \ \mathbb{H}_+^3
\end{aligned} \tag{5.24}$$

Finally, note that, in practice, $\underline{K}_{\text{pol}}$ must be estimated from multi-look data. As thor-

oughly discussed in [Teba 09], this can be efficiently accomplished by computing the best rank-2 approximation of $\underline{\widehat{K}}_{\text{pol}}$.

6 Convexity Properties of Tomographic Techniques

Thus far, the optimization problems formulated in Sections 4 and 5 have been regarded as *convex* and, as such, their local optima have been assumed to be global. This chapter verifies that these problems satisfy a reduced set of sufficient conditions, which are a subset of a well-established ruleset for ensuring convexity. In particular, an optimization problem will be said to be convex if it can be described by the following building blocks [Libe 06, Blon 08]:

1) An objective function that consists of the minimization (maximization) of a convex (concave) expression.

2) Zero or more constraints that are either a less-than inequality (i.e., $\leq$), such that the left-hand side (LHS) is a convex expression and the right-hand side (RHS) is a nonnegative constant; or a set membership relation (i.e., $\in$), such that the LHS is an affine expression and the RHS is a convex set.

In order to form valid expressions, it is important to note that [Blon 08]:

– The product of a convex expression and a nonnegative constant is a convex expression.

– The sum of convex expressions is a convex expression.

– The sum or difference of affine expressions is an affine expression.

– An affine expression is both a convex and a concave expression.

In addition, the following composition rules will be considered [Blon 08]:

– The composition of a convex function with an affine function is convex.

– The composition of a nondecreasing convex function with a convex function is convex.

Note that the $(\cdot)^2$ function will be assumed to be given by $\max\{\cdot, 0\}^2$ where the argument is real. Consequently, $(\cdot)^2$ is convex and nondecreasing and, for nonnegative arguments, it coincides with its standard definition.

In what follows, every tomographic problem will be restated first, followed by a detailed description of its ruleset-compliant building blocks. For a review of the complete ruleset, the reader is referred to [Libe 06, Blon 08] and the references therein.

6.1 Single-Channel CS

Nonpenalized Formulation

The nonpenalized single-channel CS optimization problem given by (4.30) is:

$$\begin{aligned} \min_{\widetilde{p}_i} \ & \|\Psi\,\widetilde{p}_i\|_1 \ \text{ subject to} \\ & \left\|\Phi\widetilde{p}_i - \widehat{k}_i\right\|_2 \leq \varepsilon \\ & \text{and} \\ & \widetilde{p}_i \in \mathbb{R}^n_{\geq 0} \end{aligned} \tag{6.1}$$

where $\Phi \in \mathbb{C}^{m^2 \times n}$, $\widetilde{p}_i \in \mathbb{R}^n$, $\widehat{k}_i \in \mathbb{C}^{m^2}$, $\Psi \in \mathbb{R}^{n \times n}$, and $\varepsilon \geq 0$. The objective function $\|\Psi\,\widetilde{p}_i\|_1$ corresponds to a convex expression, since it is the L_1-norm (convex function) of an affine expression. The first constraint is an inequality with a nonnegative constant ε as RHS and a convex LHS $\left\|\Phi\widetilde{p}_i - \widehat{k}_i\right\|_2$, which follows from the fact that it is the L_2-norm

(convex function) of an affine expression. The second constraint is a set membership relation with an affine LHS $\widetilde{p}_i$ and the convex set $\mathbb{R}^n_{\geq 0}$ as RHS.

Penalized Formulation

The penalized single-channel CS counterpart [see (4.31) and (4.32)] is given by:

$$\min_{\widetilde{p}_i} \ \|\Psi\,\widetilde{p}_i\|_1 + \tau_1 \left\|\Phi\widetilde{p}_i - \widehat{k}_i\right\|_2^2 + \tau_2 \|\widetilde{p}_i\|_{\text{TV}} \ \text{ subject to } \ \widetilde{p}_i \in \mathbb{R}^n_{\geq 0} \tag{6.2}$$

where $\Phi \in \mathbb{C}^{m^2 \times n}$, $\widetilde{p}_i \in \mathbb{R}^n$, $\widehat{k}_i \in \mathbb{C}^{m^2}$, $\Psi \in \mathbb{R}^{n \times n}$, $\tau_1 \geq 0$, and $\tau_2 \geq 0$. The objective function is a convex expression, since it is the sum of three convex expressions, namely, the L_1-norm (convex function) of the affine expression $\Psi\,\widetilde{p}_i$; the product of a nonnegative constant τ_1 and the square (which is, as previously defined, a nondecreasing convex function) of the L_2-norm (convex function) of the affine expression $\Phi\widetilde{p}_i - \widehat{k}_i$; and the product of a nonnegative constant τ_2 and the L_1-norm (convex function) of an affine expression [see (4.32)]. The only constraint is a set membership relation with an affine LHS $\widetilde{p}_i$ and the convex set $\mathbb{R}^n_{\geq 0}$ as RHS.

6.2 Polarimetric CS

Nonpenalized Formulation (Two SMs)

The nonpenalized polarimetric CS optimization problem restricted to two SMs [see

(4.35)] is defined by:

$$\boxed{\begin{aligned} \min_{\widetilde{\Omega}} \left\| \widetilde{\Omega} \right\|_{2,1} \quad & \text{subject to} \\ & \left\| \Phi \Psi^{\mathrm{T}} \widetilde{\Omega} V - \underline{\widehat{K}}_{\mathrm{pol}}^{2} \right\|_{\mathrm{F}} \leq \varepsilon \\ & \text{and} \\ & \dot{M} (\Psi^{\mathrm{T}} \widetilde{\Omega} V)^{\mathrm{T}} \in \mathbb{R}_{\geq 0}^{3 \times n} \end{aligned}} \tag{6.3}$$

where $\widetilde{\Omega} \in \mathbb{R}^{n \times 2}$, $\Phi \in \mathbb{C}^{m^2 \times n}$, $\Psi \in \mathbb{R}^{n \times n}$, $V \in \mathbb{C}^{2 \times 9}$, $\underline{\widehat{K}}_{\mathrm{pol}}^{2} \in \mathbb{C}^{m^2 \times 9}$, $\dot{M} \in \mathbb{C}^{3 \times 9}$, and $\varepsilon \geq 0$. The objective function $\left\| \widetilde{\Omega} \right\|_{2,1}$ corresponds to a convex expression, since it is the $L_{2,1}$-norm (convex function) of an affine expression. The first constraint is an inequality with a nonnegative constant ε as RHS and a convex LHS $\left\| \Phi \Psi^{\mathrm{T}} \widetilde{\Omega} V - \underline{\widehat{K}}_{\mathrm{pol}}^{2} \right\|_{\mathrm{F}}$, since it takes the Frobenius-norm (convex function) of an affine expression. The second constraint is a set membership relation with an affine LHS $\dot{M} (\Psi^{\mathrm{T}} \widetilde{\Omega} V)^{\mathrm{T}}$ and the convex set $\mathbb{R}_{\geq 0}^{3 \times n}$ as RHS.

Nonpenalized Formulation (More Than Two SMs)

As formulated in (4.36), the nonpenalized polarimetric CS optimization that is able to account for between two and nine SMs is defined by:

$$\boxed{\begin{aligned} \min_{\underline{\widetilde{P}}_{\mathrm{pol}}} \left\| \Psi \underline{\widetilde{P}}_{\mathrm{pol}} \right\|_{2,1} \quad & \text{subject to} \\ & \left\| \Phi \underline{\widetilde{P}}_{\mathrm{pol}} - \underline{\widehat{K}}_{\mathrm{pol}} \right\|_{\mathrm{F}} \leq \varepsilon \\ & \text{and} \\ & \underline{\widetilde{P}}_{\mathrm{pol}_j} \in \mathbb{H}_{+}^{3} \quad \text{for all} \quad 1 \leq j \leq n \end{aligned}} \tag{6.4}$$

where $\underline{\widetilde{P}}_{\mathrm{pol}} \in \mathbb{C}^{n \times 9}$, $\Phi \in \mathbb{C}^{m^2 \times n}$, $\Psi \in \mathbb{R}^{n \times n}$, $\underline{\widehat{K}}_{\mathrm{pol}} \in \mathbb{C}^{m^2 \times 9}$, $\underline{\widetilde{P}}_{\mathrm{pol}_j} \in \mathbb{C}^{3 \times 3}$, and $\varepsilon \geq 0$.

The objective function $\left\|\Psi\underline{\widetilde{P}}_{\text{pol}}\right\|_{2,1}$ is a convex expression, since it is the $L_{2,1}$-norm (convex function) of an affine expression. The first constraint is an inequality with a nonnegative constant ε as RHS and a convex LHS $\left\|\Phi\underline{\widetilde{P}}_{\text{pol}} - \underline{\widehat{K}}_{\text{pol}}\right\|_{\text{F}}$, because it takes the Frobenius-norm (convex function) of an affine expression. The jth constraint is a set membership relation with an affine LHS $\underline{\widetilde{P}}_{\text{pol}_j}$ and the convex set $\mathbb{H}^3_+$ as RHS.

Penalized Formulation (More Than Two SMs)

The penalized version of the previous problem is given by (4.37), as follows:

$$\begin{aligned}\min_{\underline{\widetilde{P}}_{\text{pol}}}\ \tau\left\|\Psi\underline{\widetilde{P}}_{\text{pol}}\right\|_{2,1} + \left\|\Phi\underline{\widetilde{P}}_{\text{pol}} - \underline{\widehat{K}}_{\text{pol}}\right\|_{\text{F}}^2 \ \text{subject to}\\ \underline{\widetilde{P}}_{\text{pol}_j} \in \mathbb{H}^3_+ \ \text{ for all } \ 1 \leq j \leq n\end{aligned} \tag{6.5}$$

where $\underline{\widetilde{P}}_{\text{pol}} \in \mathbb{C}^{n\times 9}$, $\Phi \in \mathbb{C}^{m^2\times n}$, $\Psi \in \mathbb{R}^{n\times n}$, $\underline{\widehat{K}}_{\text{pol}} \in \mathbb{C}^{m^2\times 9}$, $\underline{\widetilde{P}}_{\text{pol}_j} \in \mathbb{C}^{3\times 3}$, and $\tau \geq 0$. The objective function is a convex expression, since it is the sum of two convex expressions, namely, the product of a nonnegative constant τ and the $L_{2,1}$-norm (convex function) of the affine expression $\Psi\underline{\widetilde{P}}_{\text{pol}}$, and the square (nondecreasing convex function) of the Frobenius-norm (convex function) of the affine expression $\Phi\underline{\widetilde{P}}_{\text{pol}} - \underline{\widehat{K}}_{\text{pol}}$. The jth constraint is a set membership relation with an affine LHS $\underline{\widetilde{P}}_{\text{pol}_j}$ and the convex set $\mathbb{H}^3_+$ as RHS.

6.3 Separation of SMs

According to (5.23) and (5.24), the region defined by valid parameter pairs $(\dot{a}, \dot{b})$ that allow for separation of SMs can be found by performing two optimizations, namely, a

minimization and a maximization, as formulated below:

$$\begin{aligned}
&\min_{\widetilde{a},\widetilde{b}} \ \widetilde{a}+\widetilde{b} \ \text{ subject to} \\
&\qquad \widetilde{a}\overline{W}_1 + (1-\widetilde{a})\overline{W}_2 \quad \in \quad \mathbb{H}_+^m \\
&\qquad \widetilde{b}\overline{W}_1 + (1-\widetilde{b})\overline{W}_2 \quad \in \quad \mathbb{H}_+^m \\
&\qquad (1-\widetilde{b})\overline{V}_1 - \widetilde{b}\overline{V}_2 \quad \in \quad \mathbb{H}_+^3 \\
&\qquad -(1-\widetilde{a})\overline{V}_1 + \widetilde{a}\overline{V}_2 \quad \in \quad \mathbb{H}_+^3
\end{aligned} \tag{6.6}$$

$$\begin{aligned}
&\max_{\widetilde{a},\widetilde{b}} \ \widetilde{a}+\widetilde{b} \ \text{ subject to} \\
&\qquad \widetilde{a}\overline{W}_1 + (1-\widetilde{a})\overline{W}_2 \quad \in \quad \mathbb{H}_+^m \\
&\qquad \widetilde{b}\overline{W}_1 + (1-\widetilde{b})\overline{W}_2 \quad \in \quad \mathbb{H}_+^m \\
&\qquad (1-\widetilde{b})\overline{V}_1 - \widetilde{b}\overline{V}_2 \quad \in \quad \mathbb{H}_+^3 \\
&\qquad -(1-\widetilde{a})\overline{V}_1 + \widetilde{a}\overline{V}_2 \quad \in \quad \mathbb{H}_+^3
\end{aligned} \tag{6.7}$$

where $\widetilde{a}$ and $\widetilde{b}$ are real numbers; $\overline{W}_1$ and $\overline{W}_2 \in \mathbb{C}^{m\times m}$; and $\overline{V}_1$ and $\overline{V}_2 \in \mathbb{C}^{3\times 3}$. Note that the objective function of both optimization problems are based upon the affine expression $\widetilde{a}+\widetilde{b}$ (sum of two affine expressions). As such, it is both convex and concave, thus providing direct compliance with the convexity rules. In addition, all constraints are set membership relations with affine LHSs and convex sets as RHSs.

7 Experimental Results

7.1 Sparsity-Based Experiments

In order to demonstrate the advantages and the shortcomings of the sparsity-based methodologies outlined in Chapter 4, both simulated and real data will be used. The real data consist of 21 polarimetric SAR images obtained by the E-SAR airborne sensor of DLR during a campaign near Dornstetten, Germany, in 2006. All flights were performed at approximately the same altitude with horizontal baselines of about 20 m. Figures 7.1 and 7.2 show, respectively, an optical image and the amplitude of a radar image of this area. The center frequency used was 1.3 GHz (L-band) and the nominal altitude above ground was about 3200 m. The resulting resolutions were 0.66 m and 2.07 m in azimuth and range, respectively. The near, middle, and far ranges corresponded to 3953.15 m, 4527.09 m, and 5102.52 m, respectively [Nann 09, Nann 11]. Three different constellations will be considered employing the following: *C1*) all 21 passes; *C2*) 10 irregular passes; and *C3*) 6 irregular passes. Figures 7.3–7.5 show the histograms of horizontal baselines and corresponding horizontal cobaselines. Note that Figure 7.3(b) uncovers a high level of redundancy, unlike Figures 7.4(b) and 7.5(b).

7.1.1 Single-Channel CS

7.1.1.1 Experiments with Simulated Data

This section presents a comparison of FB and CB (as defined in Section 2.4) with the single-channel CS technique by letting $\tau_1 = \tau_2 = 0.5$ [see (4.31)] and employing a Daubechies Symmlet wavelet with 4 vanishing moments and 3 levels of decomposi-

Figure 7.1: Test site near Dornstetten, Germany ($47^\circ\ 59'\ 37.45''$ N, $10^\circ\ 51'\ 40.27''$ E). Google.

tion. To this end, a 300-look cross-range profile was simulated based on a circular Gaussian distribution with zero mean and unit variance. In addition, multi-baseline measurements were generated considering the system parameters previously introduced and constellations *C1–C3* at the near, middle, and far ranges. Decorrelation effects were introduced by means of Gaussian noise using a signal-to-noise ratio (SNR) of 10 dB.

The tomographic inversion was carried out under different assumptions on the extent of the cross-range profile, i.e., the observation space. Figure 7.6 shows the normalized profiles as a function of height obtained using 21 passes. First, an observation space of 80 m was assumed with $n = 256$ at near, middle, and far ranges [see Figures 7.6(a)–(c)]. Then, it was restricted to 40 m with $n = 128$ [see Figures 7.6(d)–(f)]. Similarly, the reconstruction was performed employing 10 and 6 tracks (see Figures 7.7 and 7.8).

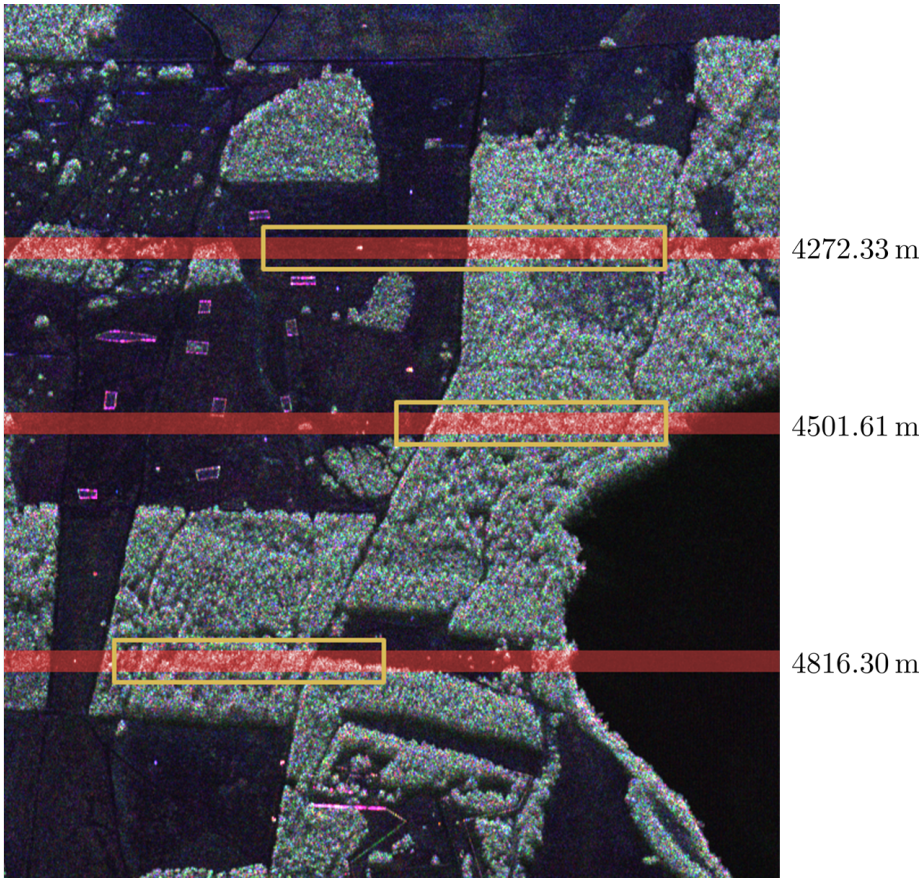

Figure 7.2: Polarimetric SAR image of the test site near Dornstetten, Germany (red: HH − VV; green: HV; blue: HH + VV). The targets of interest are located within the yellow rectangles along azimuth.

Alternatively, Figure 7.9 shows an example of the impact of choosing an insufficient range of heights (i.e., $20\,\mathrm{m}$ with $n = 128$), where part of the backscatter is neglected.

In light of these simulations, several observations can be made:

a) When using all the available passes (Figure 7.6), CS almost does not suffer from ambiguities. A further reduction of the observation space does not seem to provide any significant advantage.

b) When decreasing the number of passes to 10 (Figure 7.7), despite providing similar results to those obtained using 21 tracks, a further reduction of the range of heights does prove to be advantageous for CS at the near range. The reconstruction is actually unsatisfactory if this is not taken into account [compare Figure 7.7(a) with (d)].

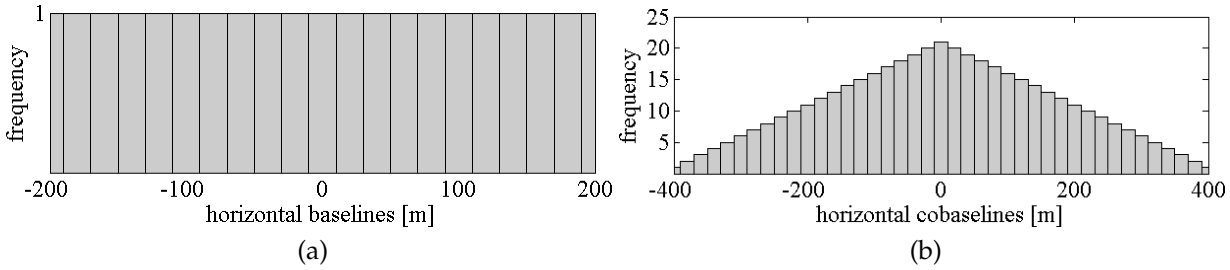

Figure 7.3: Histogram of (a) 21 horizontal baselines employed in the first constellation and (b) resulting horizontal cobaselines.

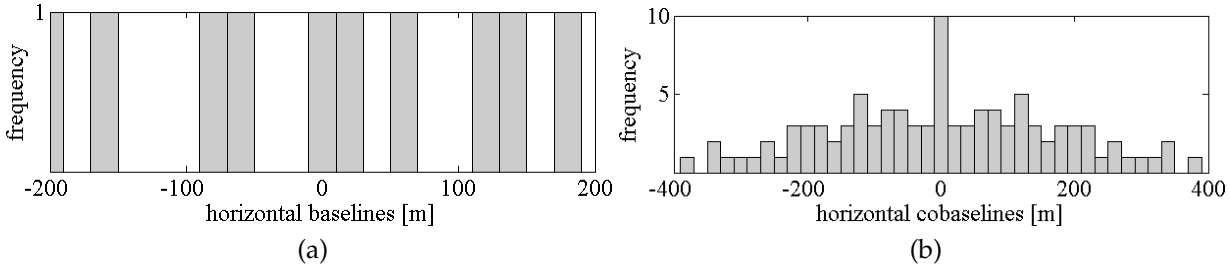

Figure 7.4: Histogram of (a) 10 horizontal baselines employed in the second constellation and (b) resulting horizontal cobaselines.

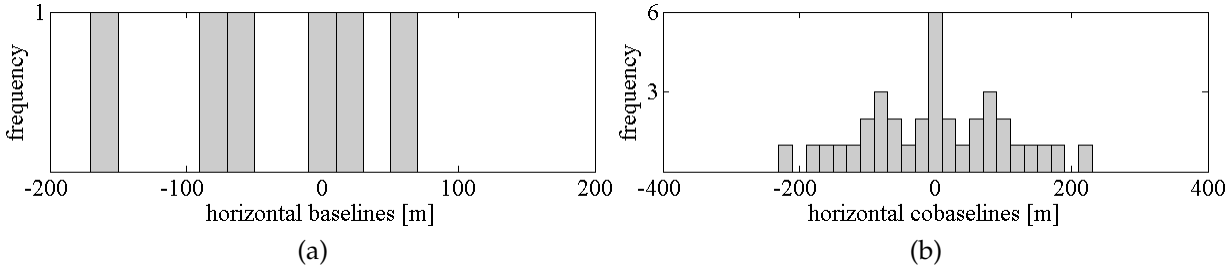

Figure 7.5: Histogram of (a) 6 horizontal baselines employed in the third constellation and (b) resulting horizontal cobaselines.

c) A more limited number of tracks (Figure 7.8) can lead to unsatisfactory results at the near range, regardless of the previous knowledge about the observation space [compare Figure 7.8(a) with (d)].

d) An erroneous range of heights may introduce artifacts in the CS reconstruction (see Figure 7.9).

Finally, note that, although the TV-norm regularization promotes the removal of spurious spikes and aliasing-like artifacts, in practice, setting $\tau_2 = 0$ also leads to satisfactory results [Agui 13c].

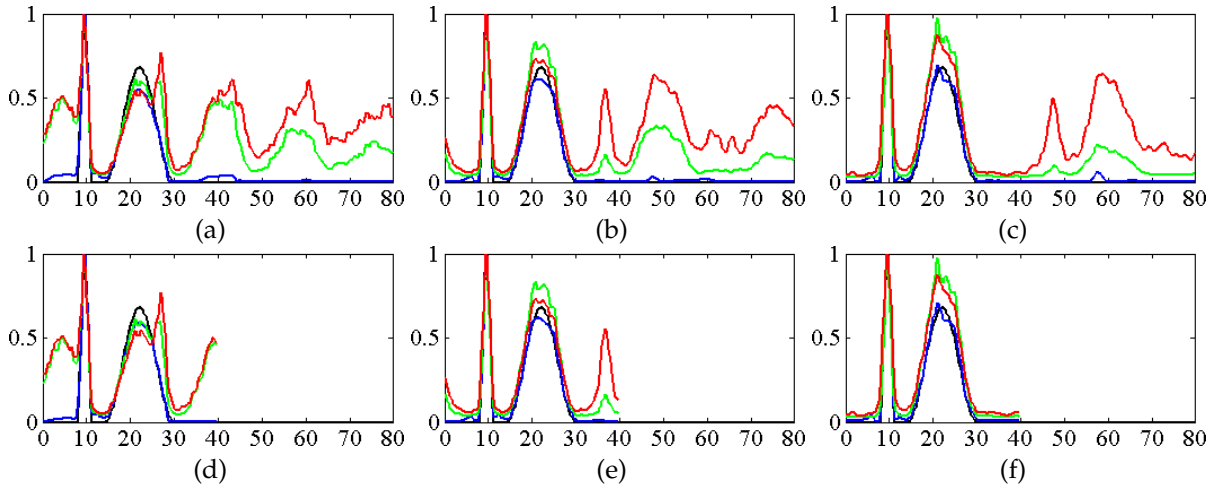

Figure 7.6: Normalized cross-range profiles as a function of height (in meters) obtained using 21 passes, 300 looks, and SNR = 10 dB. (Black) Simulated. (Blue) CS. (Green) CB. (Red) FB. (Top plots) An observation space corresponding to a height range of 80 m has been considered at (a) near, (b) middle, and (c) far ranges. (Bottom plots) A limited observation space corresponding to a height range of 40 m has been considered at (d) near, (e) middle, and (f) far ranges.

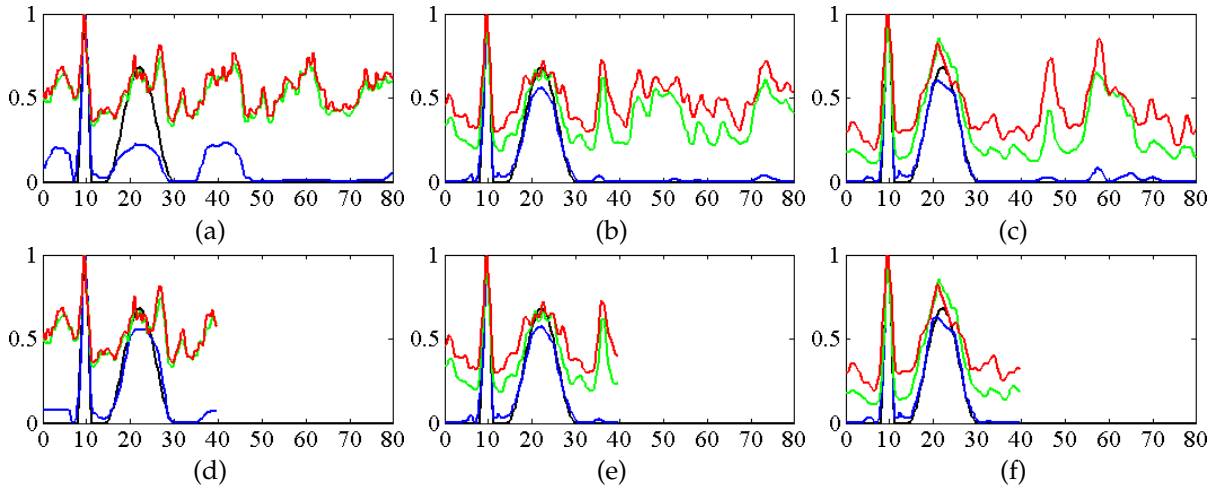

Figure 7.7: Normalized cross-range profiles as a function of height (in meters) obtained using 10 irregular passes, 300 looks, and SNR = 10 dB. (Black) Simulated. (Blue) CS. (Green) CB method. (Red) FB. (Top plots) An observation space corresponding to a height range of 80 m has been considered at (a) near, (b) middle, and (c) far ranges. (Bottom plots) A limited observation space corresponding to a height range of 40 m has been considered at (d) near, (e) middle, and (f) far ranges.

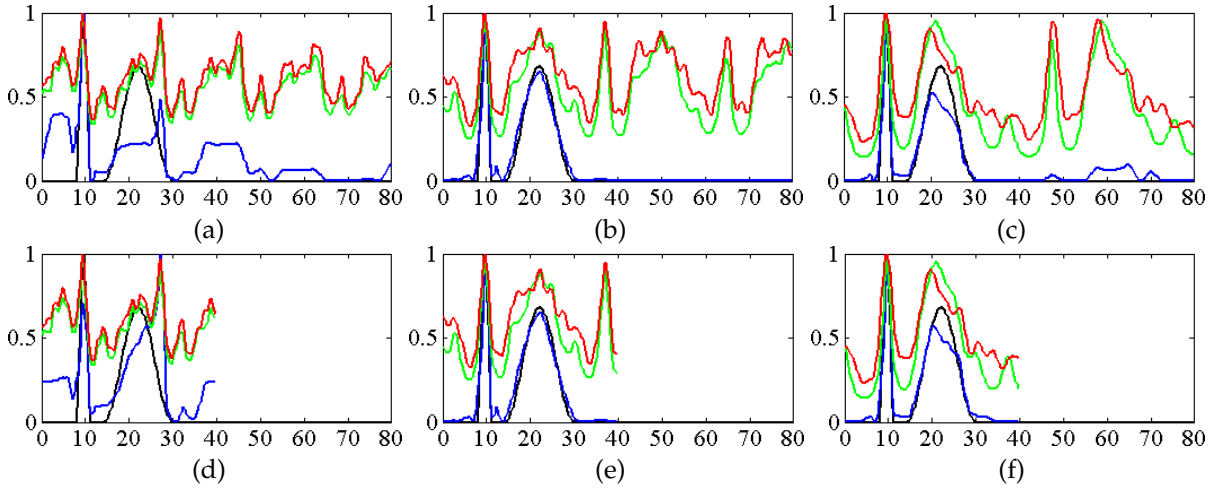

Figure 7.8: Normalized cross-range profiles as a function of height (in meters) obtained using 6 irregular passes, 300 looks, and SNR $= 10$ dB. (Black) Simulated. (Blue) CS. (Green) CB method. (Red) FB. (Top plots) An observation space corresponding to a height range of 80 m has been considered at (a) near, (b) middle, and (c) far ranges. (Bottom plots) A limited observation space corresponding to a height range of 40 m has been considered at (d) near, (e) middle, and (f) far ranges.

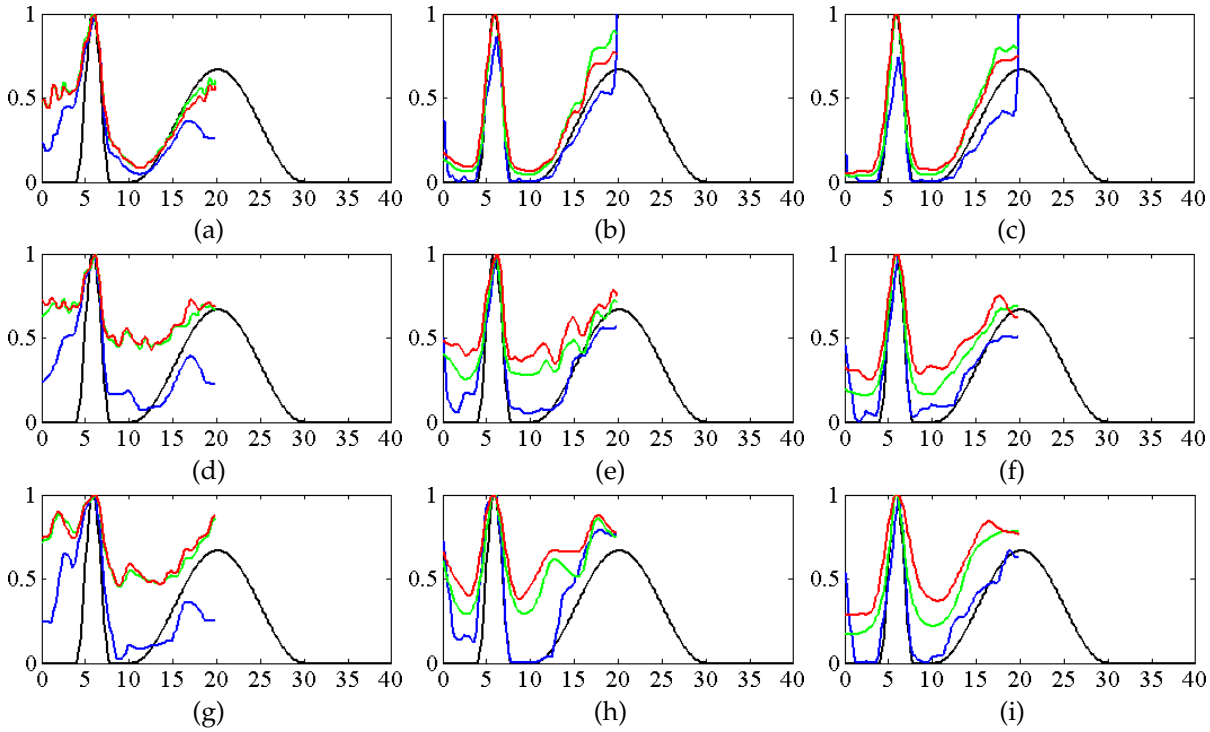

Figure 7.9: Normalized cross-range profiles as a function of height (in meters) obtained using 300 looks and SNR $= 10$ dB. (Black) Simulated. (Blue) CS. (Green) CB. (Red) FB. The observation space corresponds to a height range of 20 m, thus ignoring part of the cross-range backscatter. (Top plots) 21 passes at (a) near, (b) middle, and (c) far ranges. (Middle plots) 10 irregular passes at (d) near, (e) middle, and (f) far ranges. (Bottom plots) 6 irregular passes at (g) near, (h) middle, and (i) far ranges.

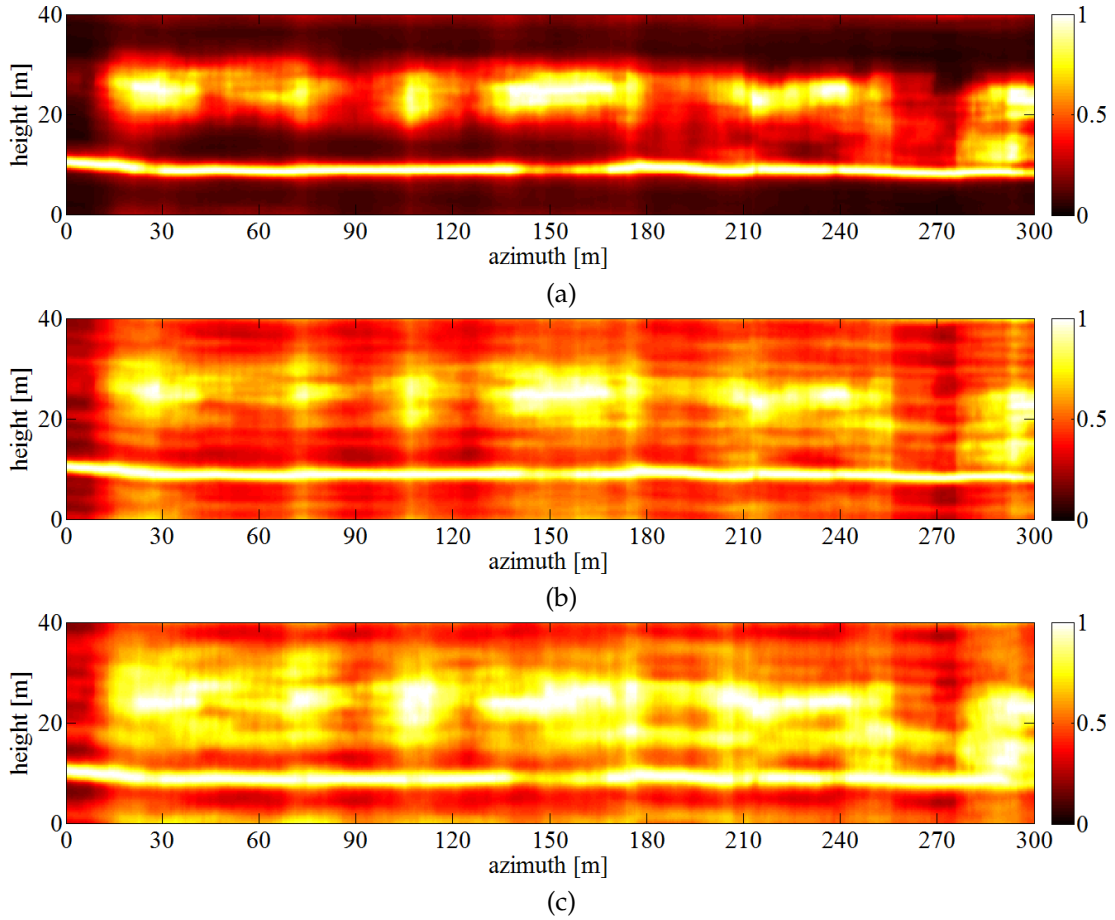

Figure 7.10: Span of tomogram (normalized at every position) obtained by FB as a function of azimuth and height (300 m by 40 m) using a $20 \times 20\,\mathrm{m}^2$ window with (a) 21, (b) 10, and (c) 6 passes. Range distance: 4816.30 m.

7.1.1.2 Experiments with Real Data

For validation purposes, several contiguous azimuth positions were selected at two different range locations (i.e., 4816.30 m and 4501.61 m), as indicated by the yellow rectangles and the red lines in Figure 7.2. As a result, tomographic slices were obtained as a function of azimuth and height of dimensions 300 m by 40 m ($n = 128$), respectively. In both cases, a $20 \times 20\,\mathrm{m}^2$ estimation window was considered. In Figure 7.10, FB was used for the range distance 4816.30 m. Figures 7.10(a)–(c) display the normalized sum of the cross-range power throughout polarimetric channels (i.e., the span) using the constellations *C1*–*C3*, respectively. Likewise, as presented in Figure 7.11, the reconstruction was carried out with CB. In order to obtain CS results, first note that (4.29)

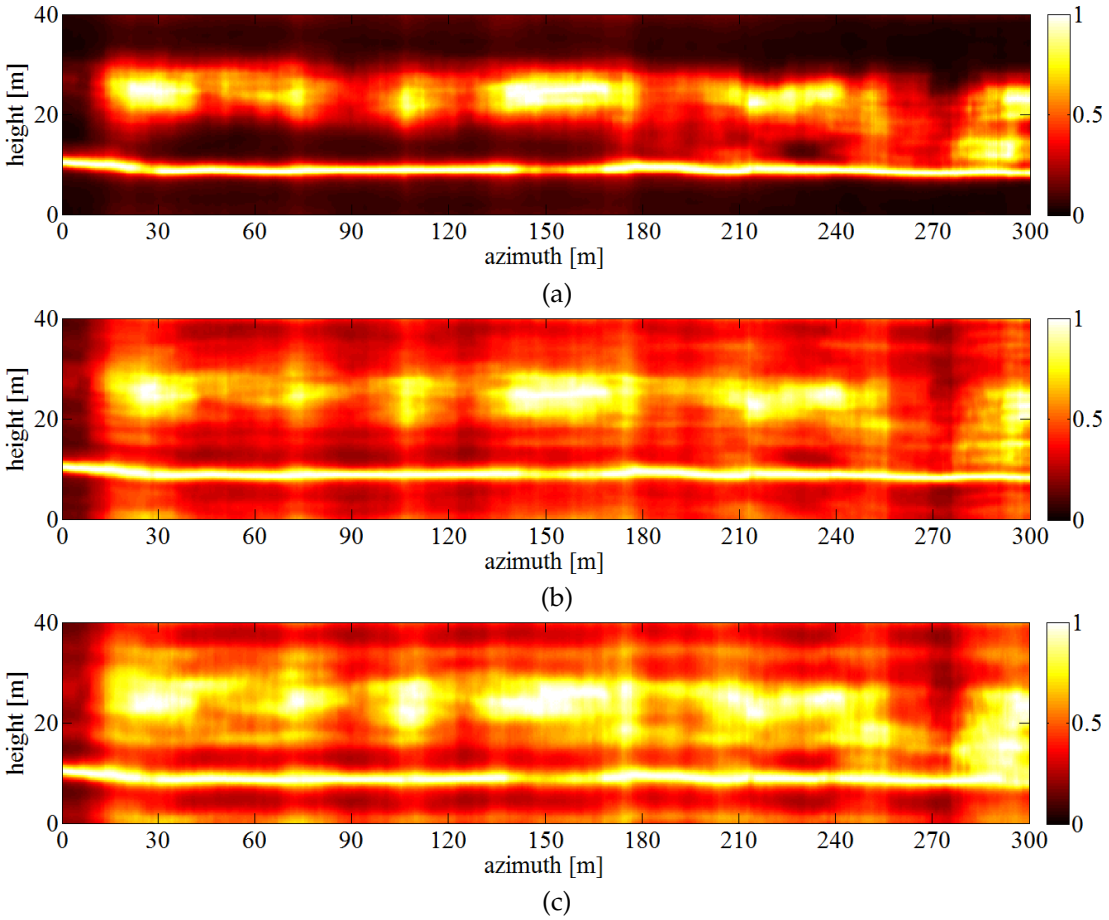

Figure 7.11: Span of tomogram (normalized at every position) obtained by CB as a function of azimuth and height (300 m by 40 m) using a $20 \times 20\,\mathrm{m}^2$ window with (a) 21, (b) 10, and (c) 6 passes. Range distance: 4816.30 m.

implies that:

$$k_{\text{HH–HH}} + k_{\text{VV–HH}} + k_{\text{HV–HV}} = \Phi\left(p_{\text{HH–HH}} + p_{\text{VV–HH}} + p_{\text{HV–HV}}\right) \tag{7.1}$$

It is therefore possible to estimate the span directly by carrying out the optimization given by (4.31) based on $\widehat{k}_{\text{span}} = \widehat{k}_{\text{HH–HH}} + \widehat{k}_{\text{VV–HH}} + \widehat{k}_{\text{HV–HV}}$. Figure 7.12 shows the results obtained using $\tau_1 = \tau_2 = 0.5$ and a Daubechies Symmlet wavelet with 4 vanishing moments and 3 levels of decomposition.

Evidently, all methods bear comparison with each other for *C1* [see Figures 7.10(a), 7.11(a), and 7.12(a)]. However, a reduction in the number of tracks, i.e., constellations *C2*–*C3*, reveals the robustness of the different methods. In contrast to CS [Figures 7.12(b) and (c)], these irregular baseline distributions cause FB [Figures 7.10(b) and (c)] as well

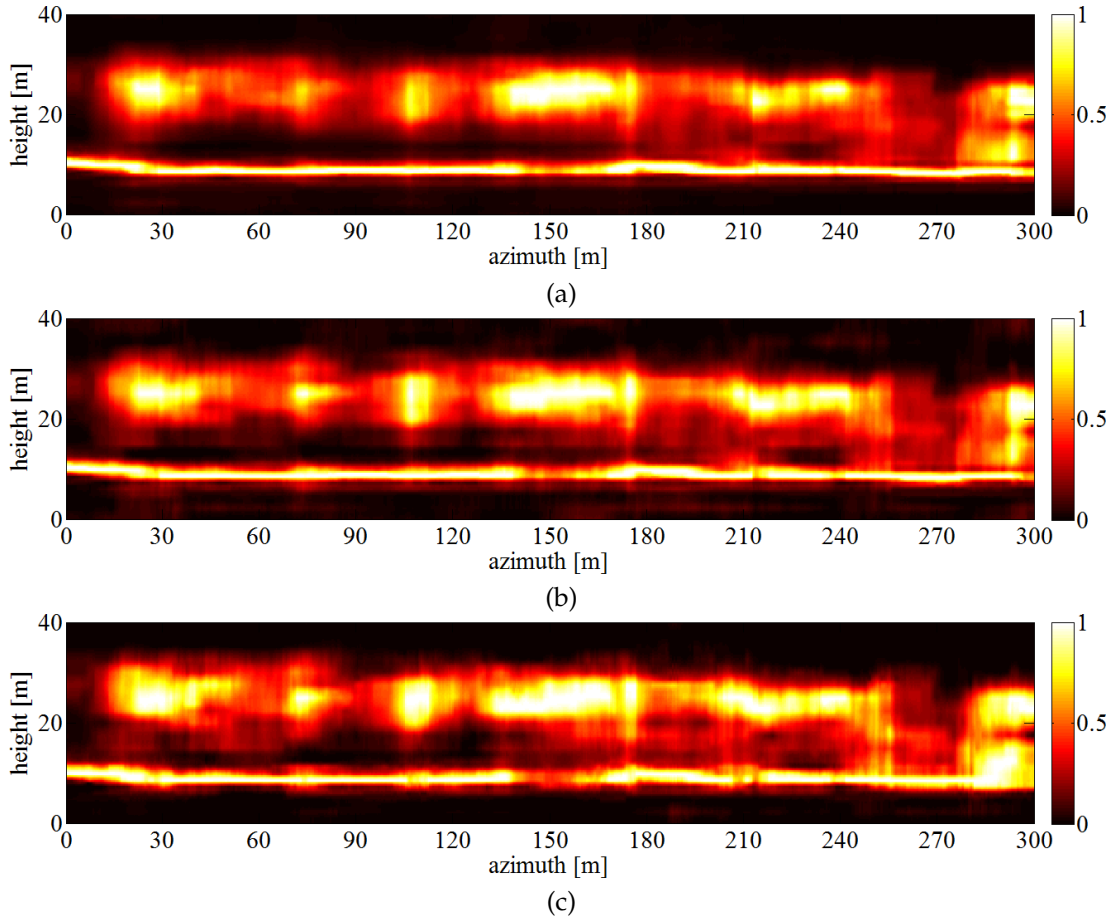

Figure 7.12: Span of tomogram (normalized at every position) obtained by CS as a function of azimuth and height (300 m by 40 m) using a $20 \times 20\,\mathrm{m}^2$ window with (a) 21, (b) 10, and (c) 6 passes. Range distance: 4816.30 m.

as CB [Figures 7.11(b) and (c)] to present more severe artifacts, just as observed with the simulated data. Figures 7.13–7.15 show similar results at the nearer range 4501.61 m, so as to see the impact of the ambiguities even for *C1*. Upon comparison, the CS reconstruction exhibits the lowest ambiguity level.

7.1.1.3 Computation Time

Note that even though research is currently being conducted in order to solve CS problems efficiently (see, for example, [Beck 11] and the references therein), the increase in computational complexity is significant. By way of illustration, Figure 7.16 presents three histograms of the reconstruction time required for single-channel CS [as formulated in (4.31)]. The different constellations (*C1*–*C3*) were employed for simulating

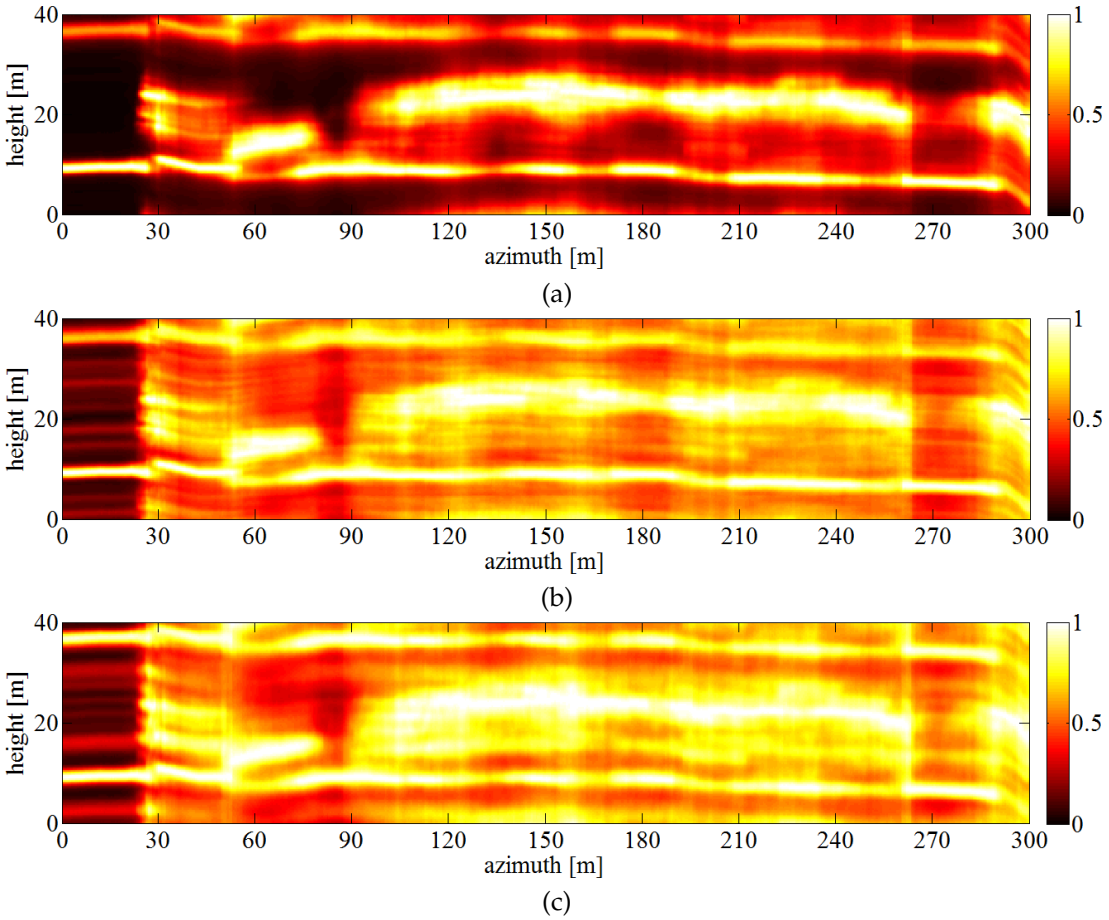

Figure 7.13: Span of tomogram (normalized at every position) obtained by FB as a function of azimuth and height (300 m by 40 m) using a $20 \times 20\,\mathrm{m}^2$ window with (a) 21, (b) 10, and (c) 6 passes. Range distance: 4501.61 m.

the corresponding multi-baseline measurements at the far range. For every realization (2000 in total), one of the profiles from the left column of Figure 4.4 was chosen uniformly at random. The SNR $= 10$ dB and the number of looks was 300. The resulting times have been normalized to the FB reconstruction time using 21 passes. The solver used was CVX, which is a package for specifying and solving convex programs [Gran 13]. As conveyed by the histograms, besides incurring much more computation time, CS is less predictable, due to the iterative nature of the algorithm.

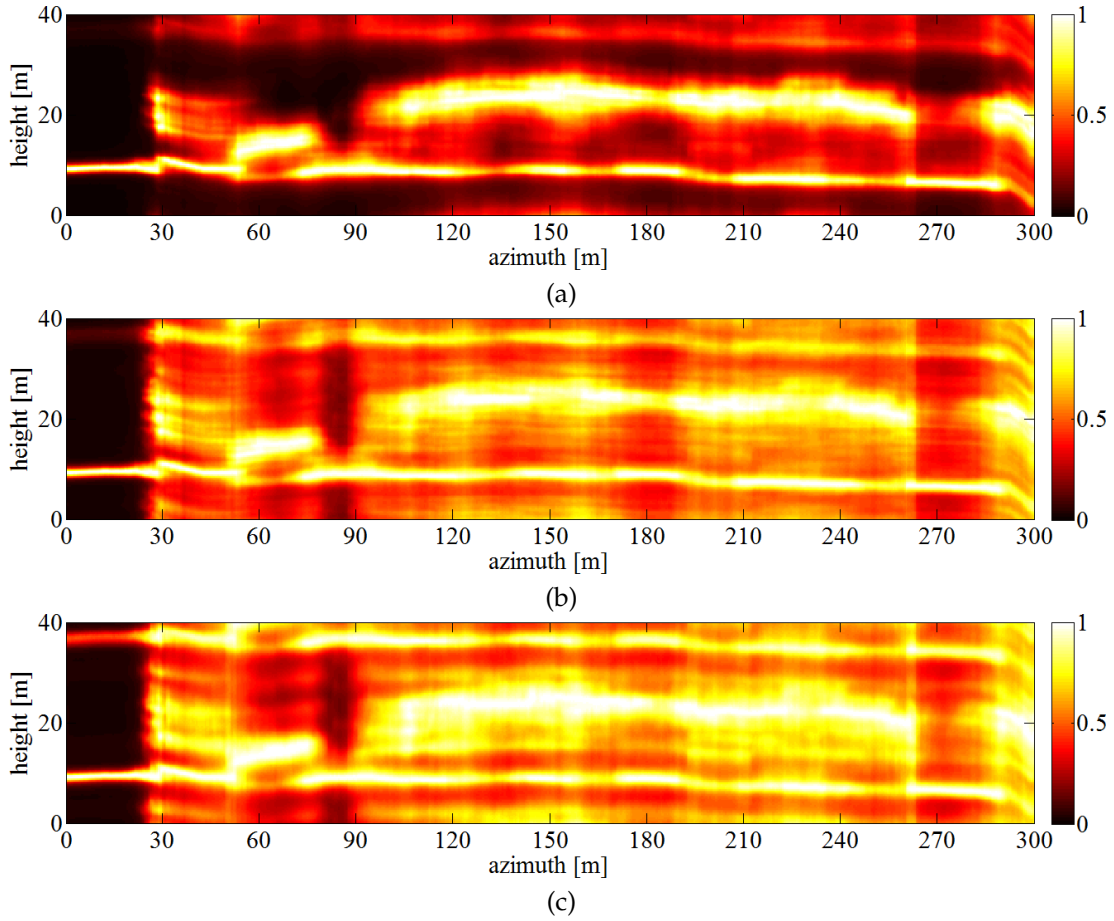

Figure 7.14: Span of tomogram (normalized at every position) obtained by CB as a function of azimuth and height (300 m by 40 m) using a $20 \times 20\,\mathrm{m}^2$ window with (a) 21, (b) 10, and (c) 6 passes. Range distance: 4501.61 m.

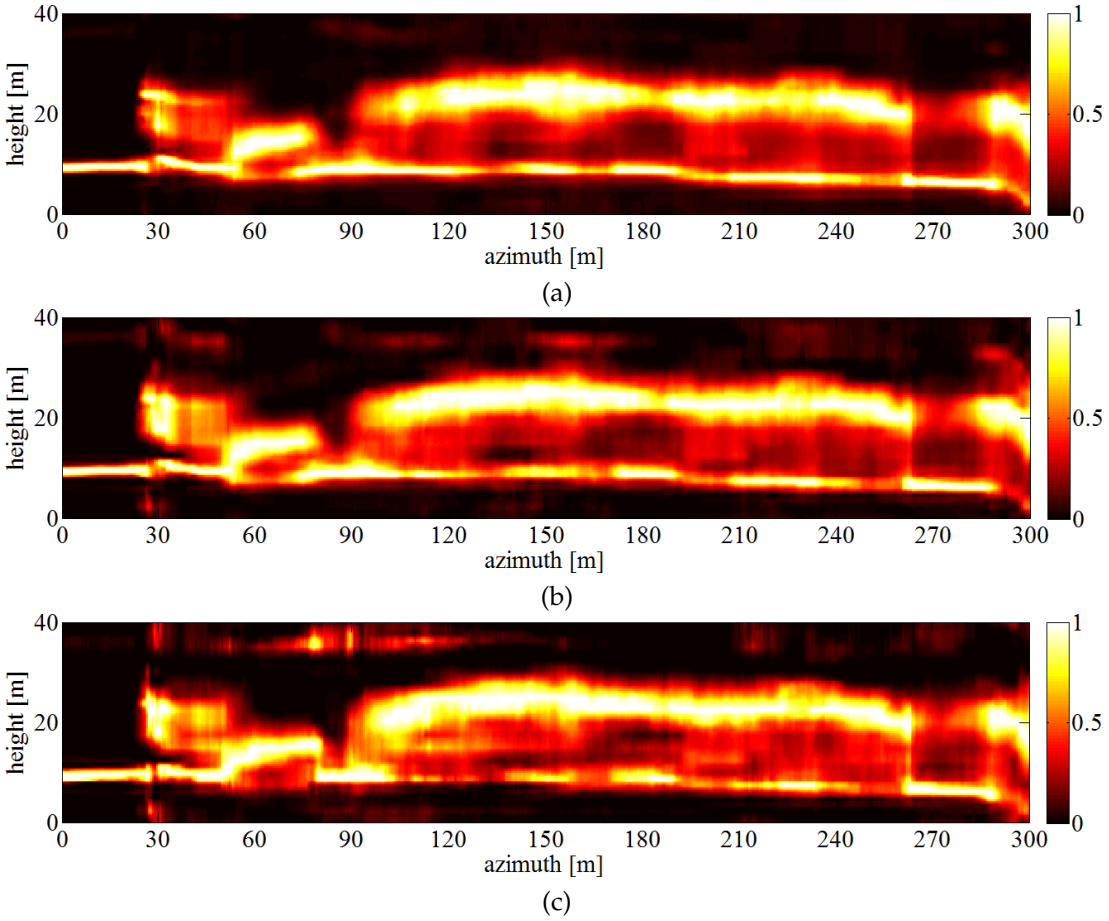

Figure 7.15: Span of tomogram (normalized at every position) obtained by CS as a function of azimuth and height (300 m by 40 m) using a $20 \times 20\,\mathrm{m}^2$ window with (a) 21, (b) 10, and (c) 6 passes. Range distance: 4501.61 m.

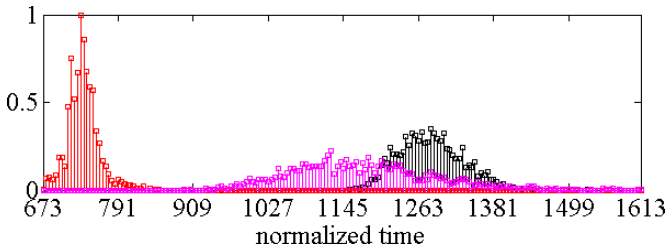

Figure 7.16: Normalized histogram of the reconstruction time required for CS (black: 21 passes; red: 10 passes; magenta: 6 passes). The times have been normalized to the FB reconstruction time using 21 passes.

7.1.2 Polarimetric CS

7.1.2.1 Tomographic Slices

For the polarimetric CS case, the tomographic reconstruction was conducted in the lexicographic representation according to (4.37). Again, the sparsifying basis $\Psi \in \mathbb{R}^{128\times128}$ was based on the Daubechies Symmlet wavelet with 4 vanishing moments and 3 levels of decomposition. The same azimuth positions as those selected for the single-channel case at $4816.30\,\mathrm{m}$ were considered, as indicated by the yellow rectangle in Fig. 7.2. The sample covariance matrix was computed by taking a $20 \times 20\,\mathrm{m}^2$ estimation window. The value of τ was found heuristically by performing the reconstruction repeatedly with increasing τ starting from 0 (i.e., no regularization). Then, the smallest value was chosen such that all the recovered profiles exhibited no spikes, so as to be consistent with the assumption that the unknown cross-range powers are sparse in the wavelet domain. In this regard, note that spikes, or rather spatially-sparse solutions, are expected in this kind of optimization when it is not regularized but nonnegativity constraints are imposed (see, for example, [Dono 10]). For this specific tomographic slice $\tau = 2$ was decided upon. Figures 7.17–7.19 show a comparison of the reconstructed profiles using *C2* for the HH, VV, and HV channels, respectively. In each figure, the FB reconstruction using *C1* is shown as a reference first, followed by the FB, CB, and CS reconstructions. Likewise, Figures 7.20–7.22 present tomographic slices using *C3*. As conveyed by the figures, the CS reconstruction is able to counter the artifacts exhibited by CB and FB, just like in the single-channel case.

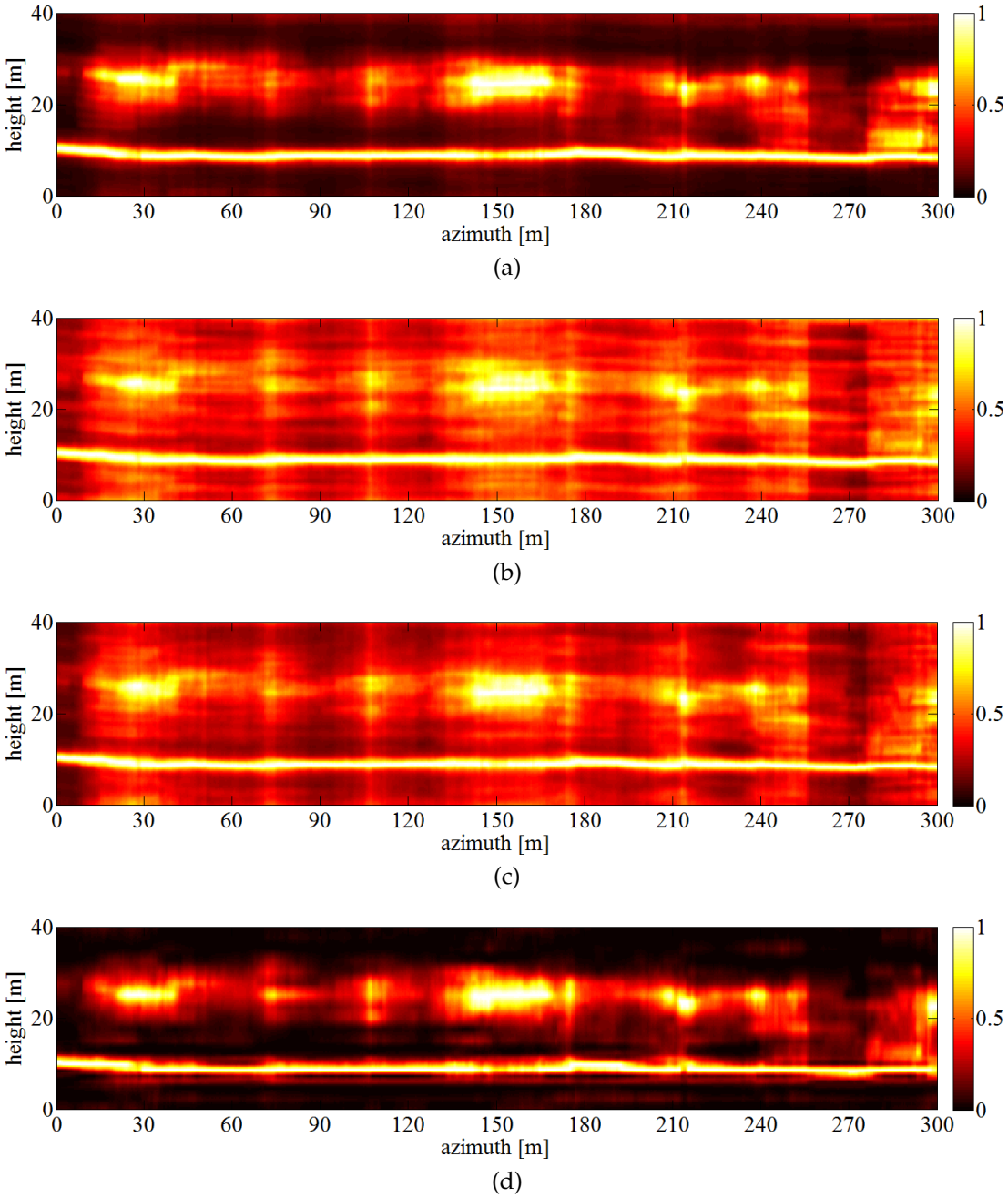

Figure 7.17: Tomographic slices in the HH channel (normalized at every position) obtained as a function of azimuth and height (300 m by 40 m) using a $20 \times 20\,\mathrm{m}^2$ window. (a) FB reconstruction with 21 passes. (b) FB reconstruction with 10 passes. (c) CB reconstruction with 10 passes. (d) Polarimetric CS reconstruction with 10 passes. Range distance: 4816.30 m.

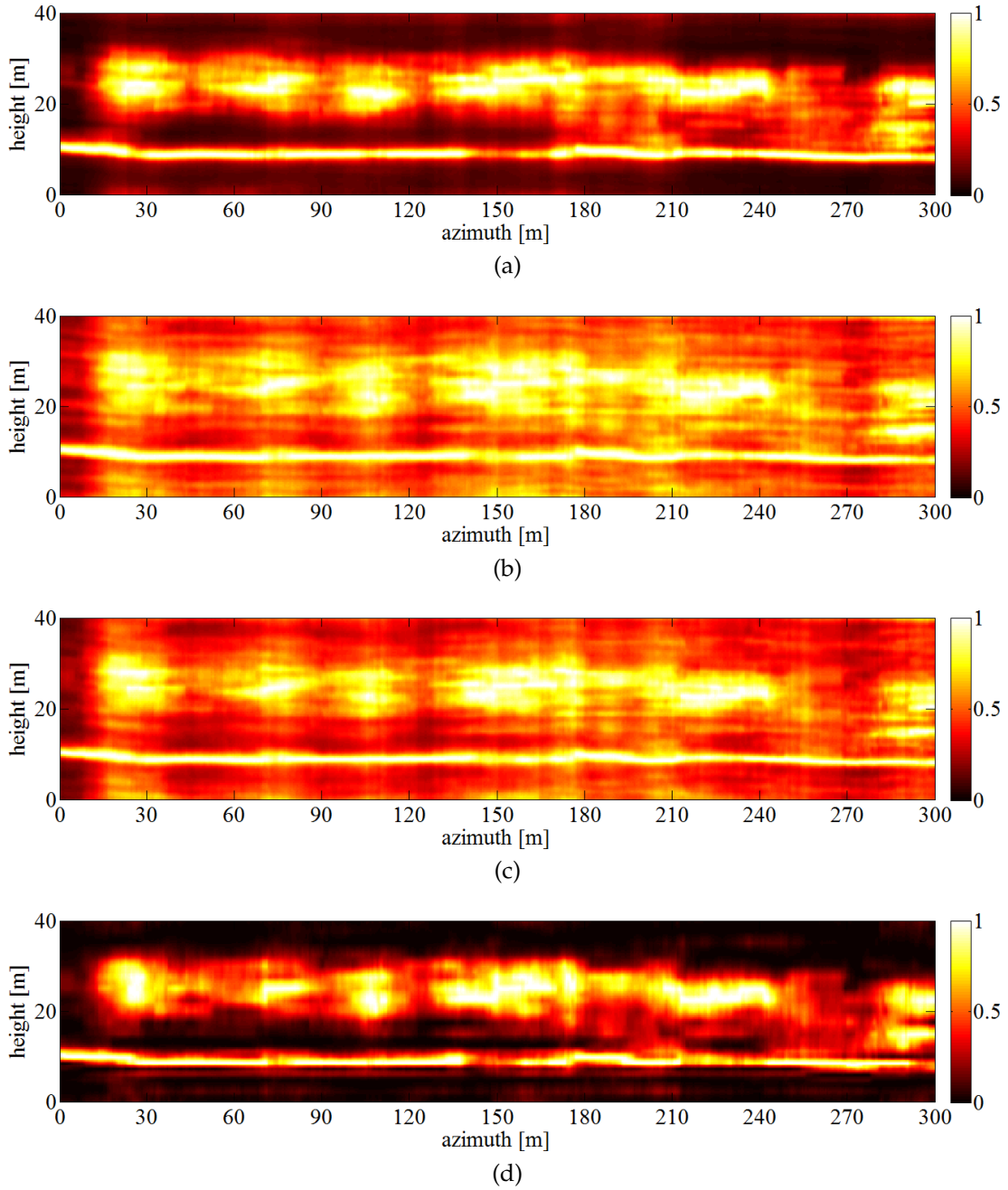

Figure 7.18: Tomographic slices in the VV channel (normalized at every position) obtained as a function of azimuth and height (300 m by 40 m) using a $20 \times 20\,\mathrm{m}^2$ window. (a) FB reconstruction with 21 passes. (b) FB reconstruction with 10 passes. (c) CB reconstruction with 10 passes. (d) Polarimetric CS reconstruction with 10 passes. Range distance: 4816.30 m.

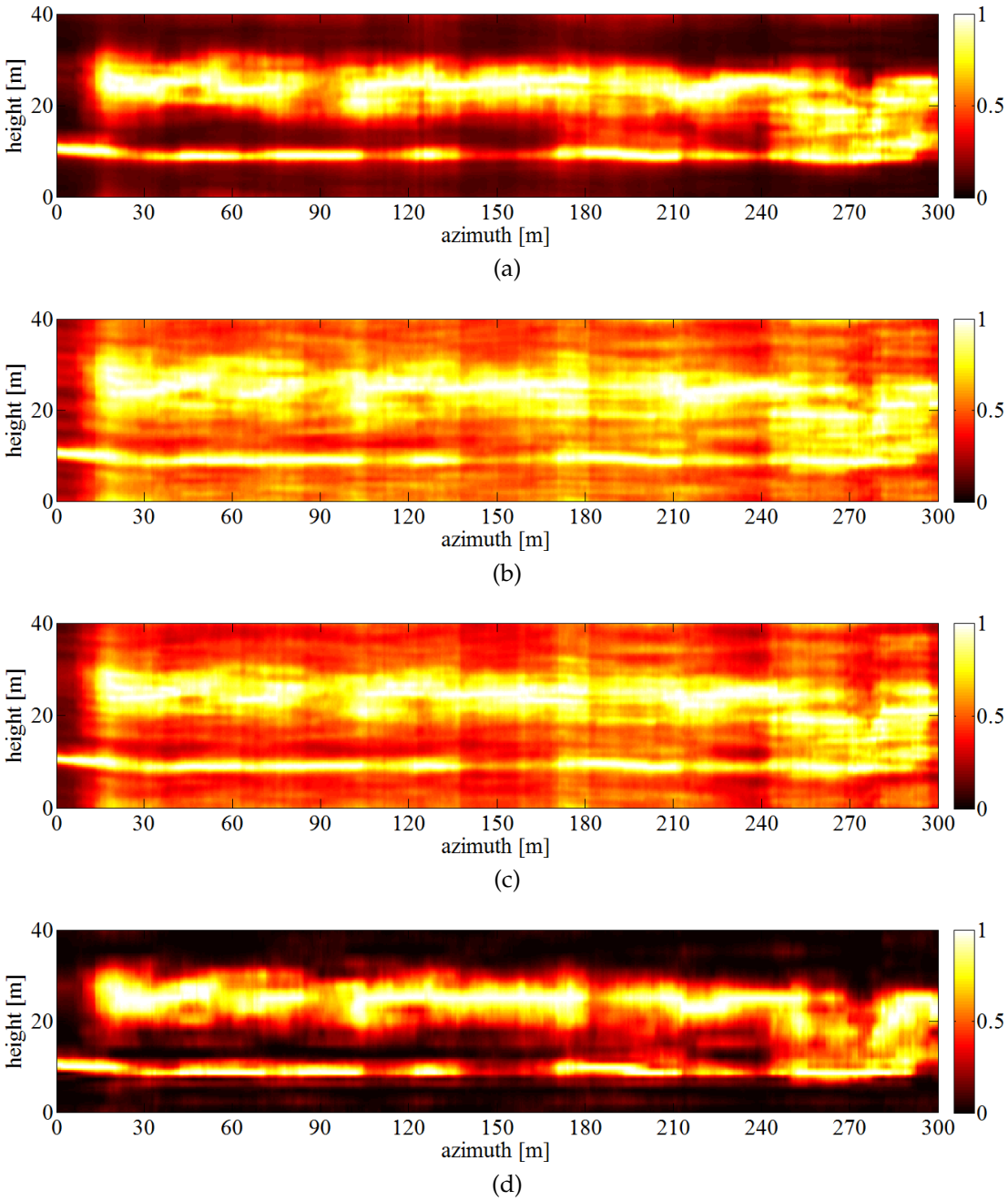

Figure 7.19: Tomographic slices in the HV channel (normalized at every position) obtained as a function of azimuth and height (300 m by 40 m) using a $20 \times 20\,\mathrm{m}^2$ window. (a) FB reconstruction with 21 passes. (b) FB reconstruction with 10 passes. (c) CB reconstruction with 10 passes. (d) Polarimetric CS reconstruction with 10 passes. Range distance: 4816.30 m.

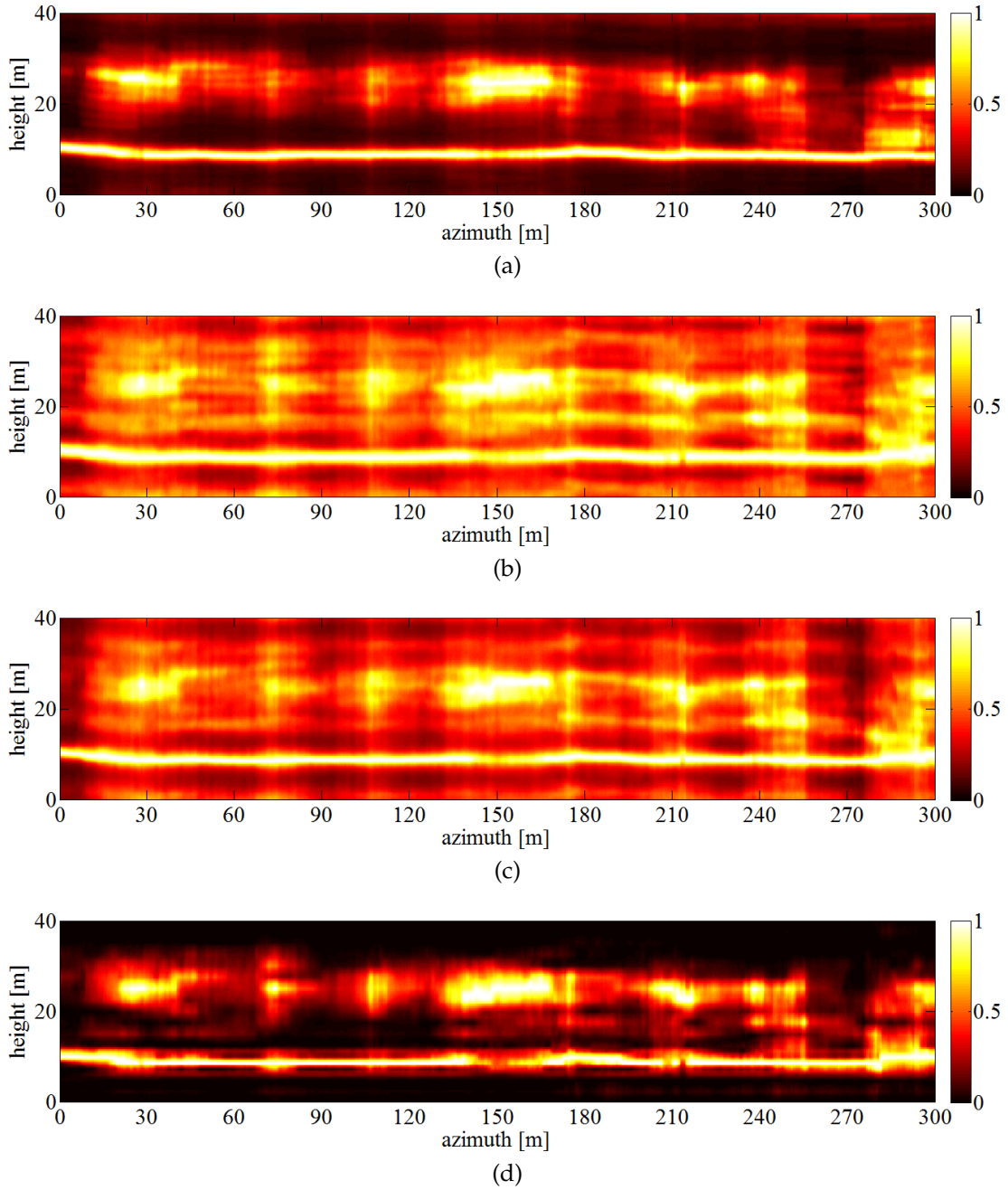

Figure 7.20: Tomographic slices in the HH channel (normalized at every position) obtained as a function of azimuth and height (300 m by 40 m) using a $20 \times 20\,\mathrm{m}^2$ window. (a) FB reconstruction with 21 passes. (b) FB reconstruction with 6 passes. (c) CB reconstruction with 6 passes. (d) Polarimetric CS reconstruction with 6 passes. Range distance: 4816.30 m.

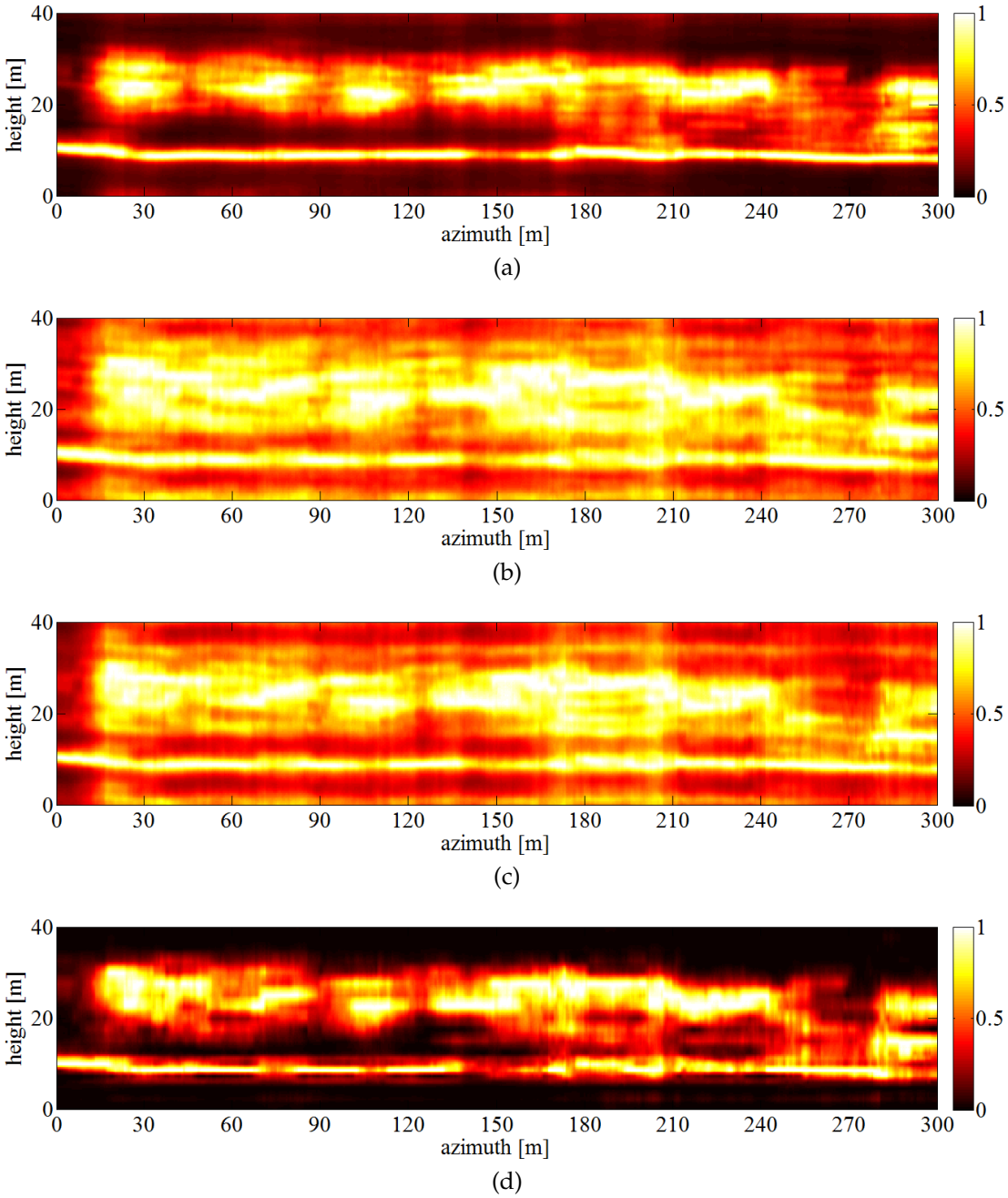

Figure 7.21: Tomographic slices in the VV channel (normalized at every position) obtained as a function of azimuth and height (300 m by 40 m) using a $20 \times 20\,\mathrm{m}^2$ window. (a) FB reconstruction with 21 passes. (b) FB reconstruction with 6 passes. (c) CB reconstruction with 6 passes. (d) Polarimetric CS reconstruction with 6 passes. Range distance: 4816.30 m.

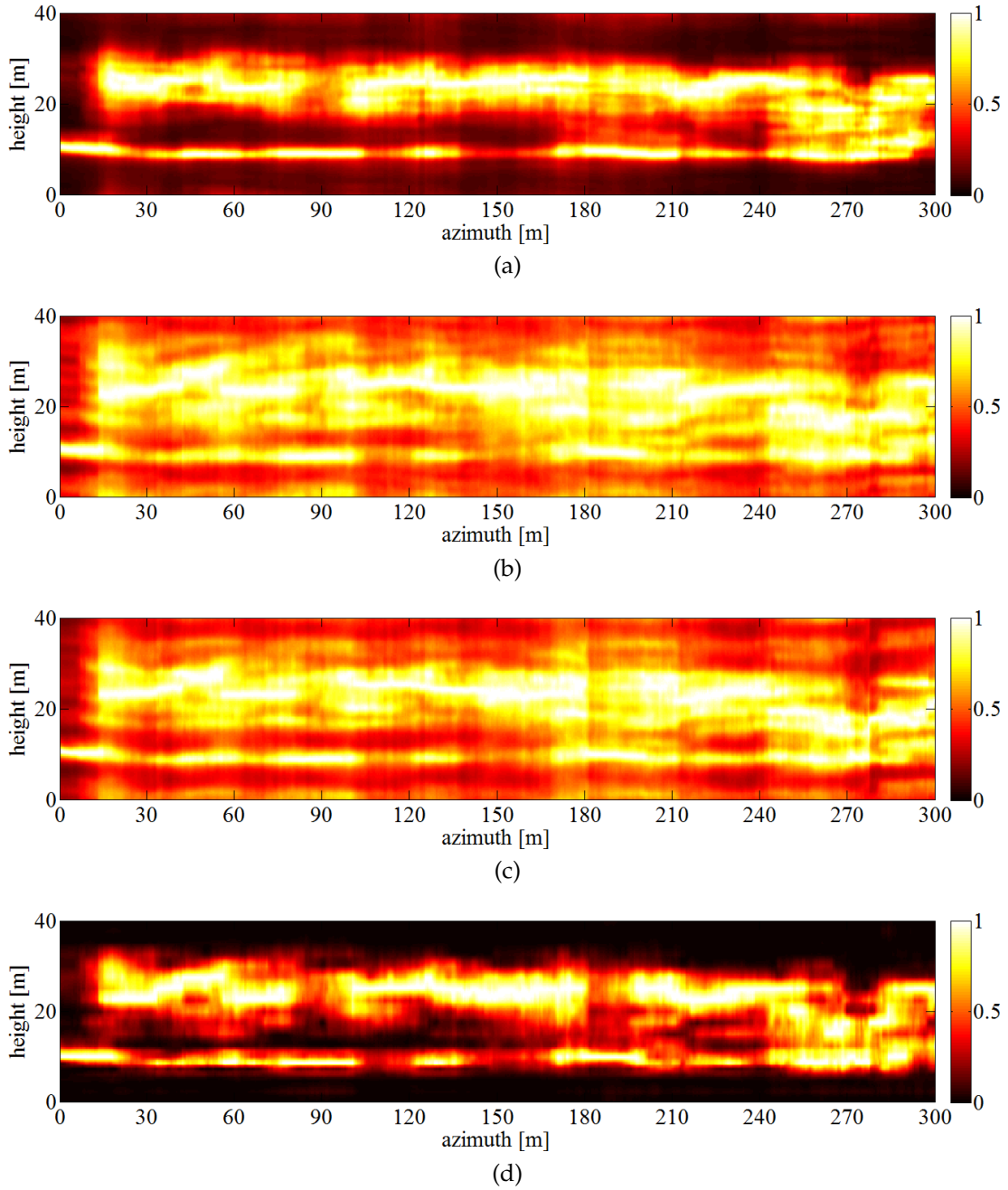

Figure 7.22: Tomographic slices in the HV channel (normalized at every position) obtained as a function of azimuth and height (300 m by 40 m) using a $20 \times 20\,\mathrm{m}^2$ window. (a) FB reconstruction with 21 passes. (b) FB reconstruction with 6 passes. (c) CB reconstruction with 6 passes. (d) Polarimetric CS reconstruction with 6 passes. Range distance: 4816.30 m.

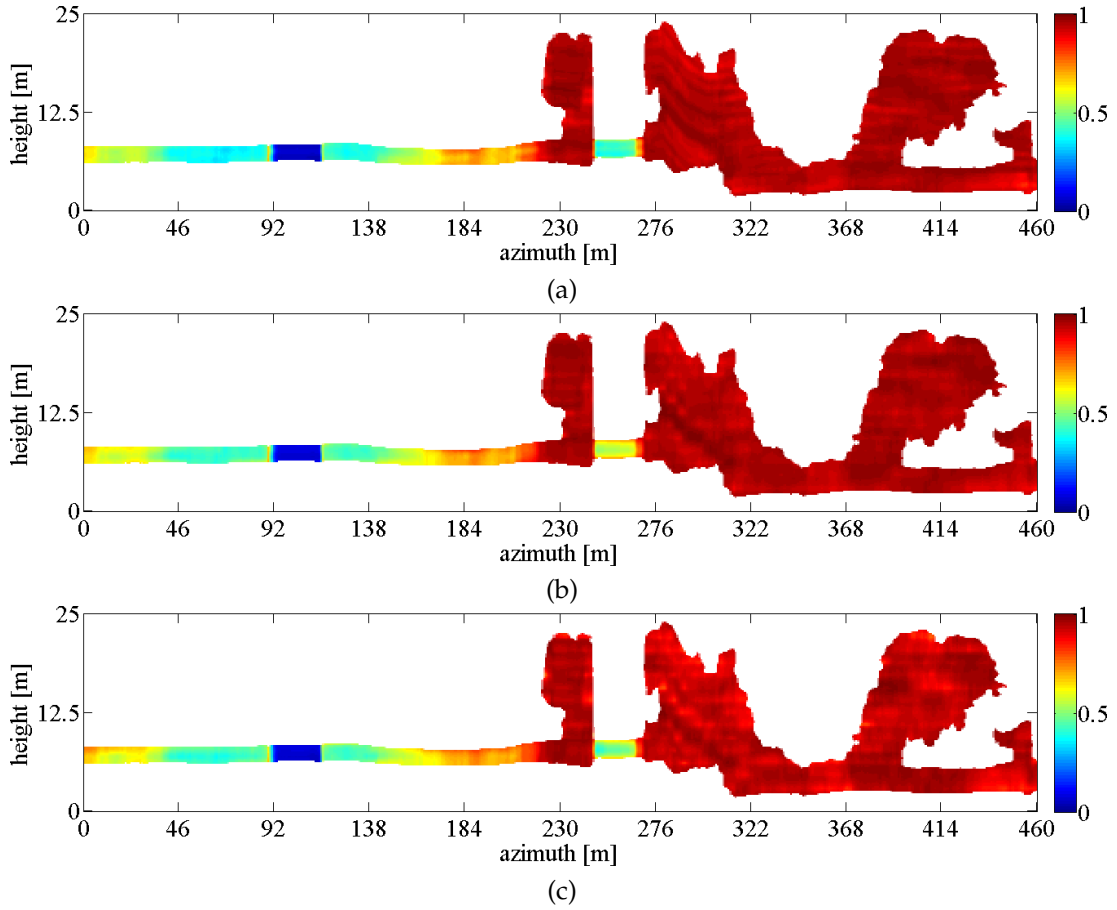

Figure 7.23: Polarimetric entropy obtained as a function of azimuth and height ($460\,\mathrm{m}$ by $25\,\mathrm{m}$) using a $20 \times 20\,\mathrm{m}^2$ window and a common mask. The slices correspond to (a) FB with 21 passes, (b) polarimetric CS with 10 passes, and (c) polarimetric CS with 6 passes. Range distance: $4272.33\,\mathrm{m}$.

7.1.2.2 Polarimetric Validation

In order to validate the property of physical validity, tomographic slices of dimensions $460\,\mathrm{m}$ by $25\,\mathrm{m}$ were obtained in the Pauli representation according to (4.37) using $C2$ and $C3$. The sparsifying basis $\Psi \in \mathbb{R}^{128\times128}$ corresponded to that used in previous sections and the sample covariance matrix was computed by taking a $20 \times 20\,\mathrm{m}^2$ estimation window. The range distance was $4272.33\,\mathrm{m}$, as indicated by the yellow rectangle in Fig. 7.2. Then, several polarimetric parameters (see Section 3.3) were computed for each retrieved $\underline{\widetilde{P}}_{\mathrm{pol}_j}$. Figures 7.23–7.26 present, respectively, the polarimetric entropy, anisotropy, mean alpha angle, and maximum alpha angle (note that angles are given in degrees). In each figure, the FB reconstruction using 21 passes is shown first, followed by the CS reconstruction with $C2$ and $C3$. Note that, for comparison purposes,

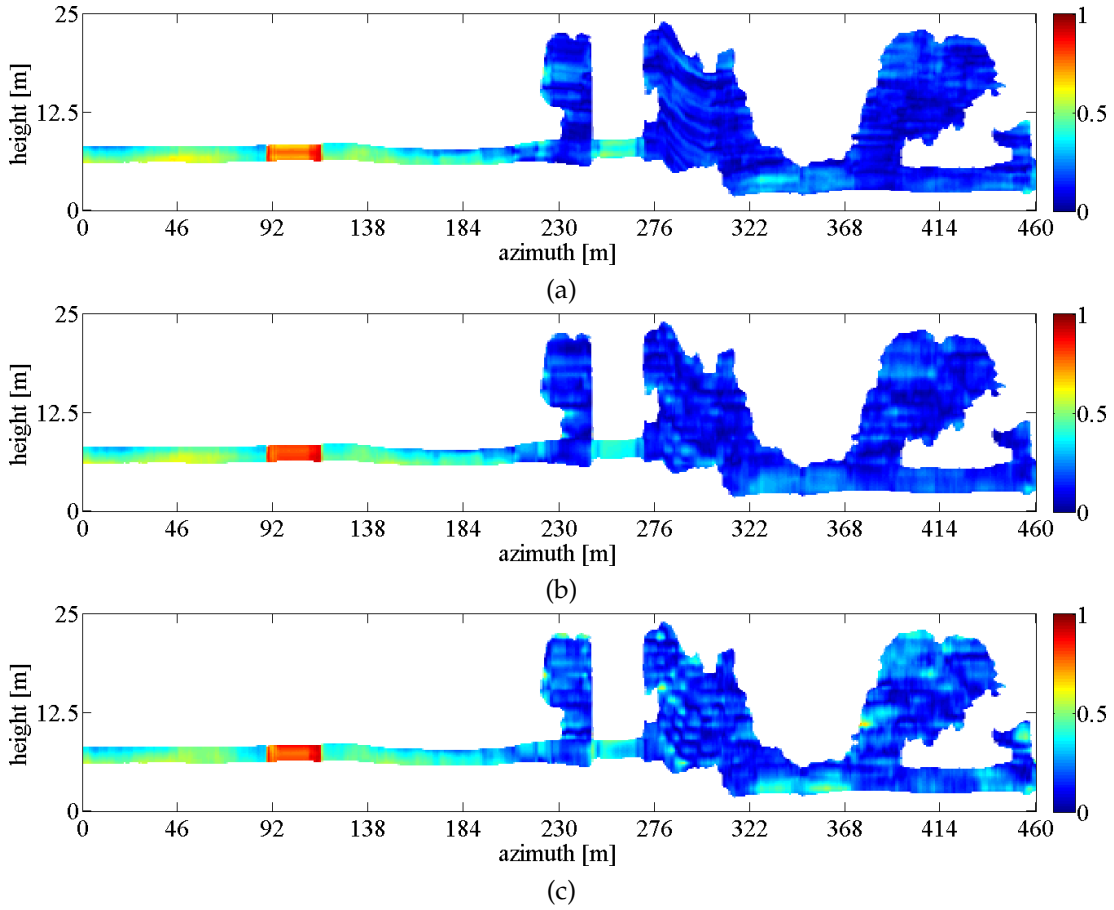

Figure 7.24: Polarimetric anisotropy obtained as a function of azimuth and height (460 m by 25 m) using a $20 \times 20\,\mathrm{m}^2$ window and a common mask. The slices correspond to (a) FB with 21 passes, (b) polarimetric CS with 10 passes, and (c) polarimetric CS with 6 passes. Range distance: 4272.33 m.

a common mask has been applied and thus white regions should not be considered.

In addition to bearing comparison with the linear reconstruction provided by FB, the CS slices are consistent with the expected scattering phenomena. Specifically, the azimuth interval $[46\,\mathrm{m}, 138\,\mathrm{m}]$ is known to correspond with scattering from a bare surface where a metallic container of dimensions $6.10 \times 2.40 \times 2.55\,\mathrm{m}^3$ ([length] $\times$ [width] $\times$ [height]) has been placed at $100\,\mathrm{m}$ [Nann 11]. As a result, while the entropy is low for both the ground and the container, the mean and maximum alpha angle tend to be $0°$ for the ground and $90°$ for the container. The anisotropy is not considered in this interval, since it is expected to be noisy due to the low entropy values [Lee 09]. On the other hand, the azimuth interval $[230\,\mathrm{m}, 414\,\mathrm{m}]$ corresponds with forest scattering where another metallic container has been placed at $250\,\mathrm{m}$. As expected, the entropy is high for the forest but lower for the container, while the anisotropy gives, in general, low

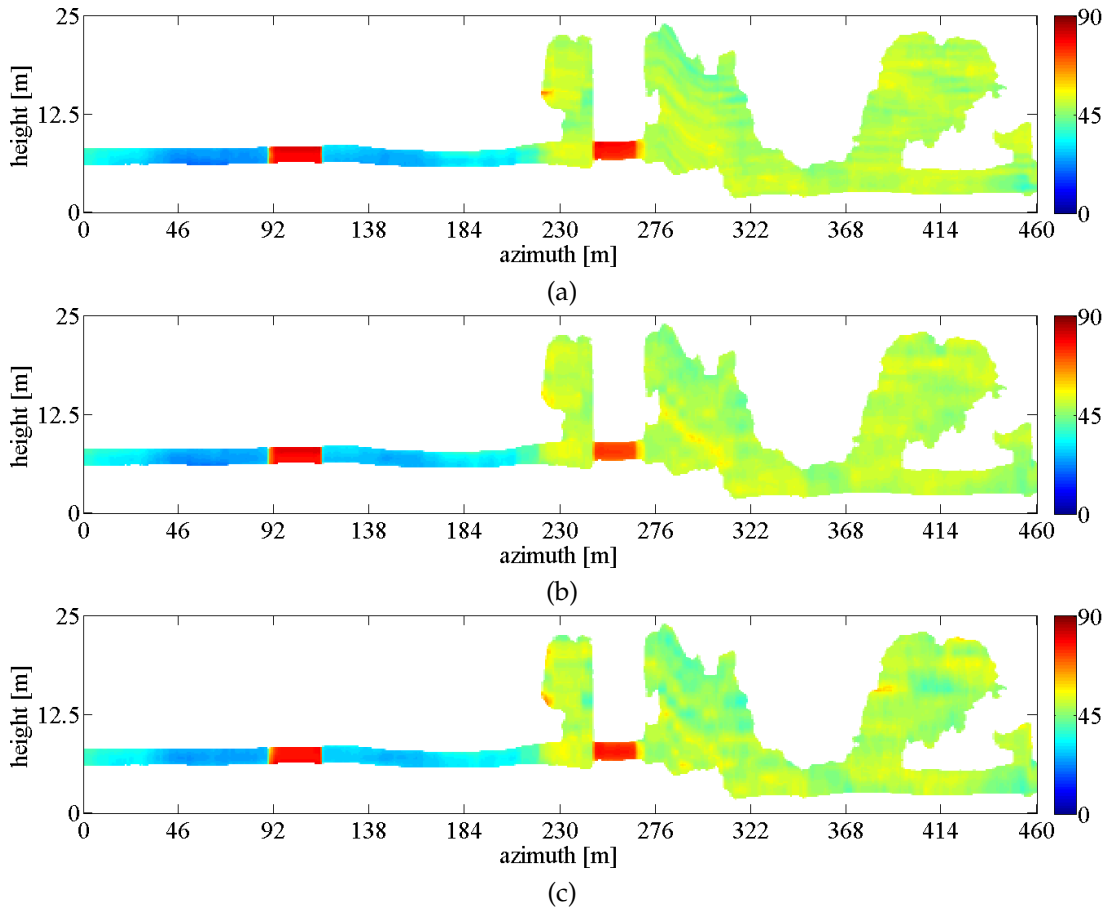

Figure 7.25: Mean alpha angle obtained as a function of azimuth and height (460 m by 25 m) using a $20 \times 20\,\mathrm{m}^2$ window and a common mask. The slices correspond to (a) FB with 21 passes, (b) polarimetric CS with 10 passes, and (c) polarimetric CS with 6 passes. Range distance: 4272.33 m.

values [Lee 09]. In addition, the mean alpha angle throughout the forest corresponds with volume scattering and is hence close to $45°$.

For additional verification purposes, 4000 azimuth–range positions were randomly chosen from a region where cross-range profiles are expected to have a very limited spatial extent, as indicated by the yellow rectangle in Figure 7.27. Then, the tomographic reconstruction was carried out by FB using constellation *C1* and by polarimetric CS using constellations *C2* and *C3*. Next, the estimated $\underline{\widetilde{P}}_{\mathrm{pol}_j}$ corresponding to the height of maximum span was selected, thus yielding 2-D maps of 3-by-3 covariance matrices. Subsequently, the entropy, anisotropy, and alpha angles were computed for these 2-D maps as well as for two 2-D polarimetric SAR images corresponding to the reference track (i.e., the 0-baseline track) and a 100 m-baseline slave track. The reason for this choice lies in the fact that, since a limited cross-range spatial distribution

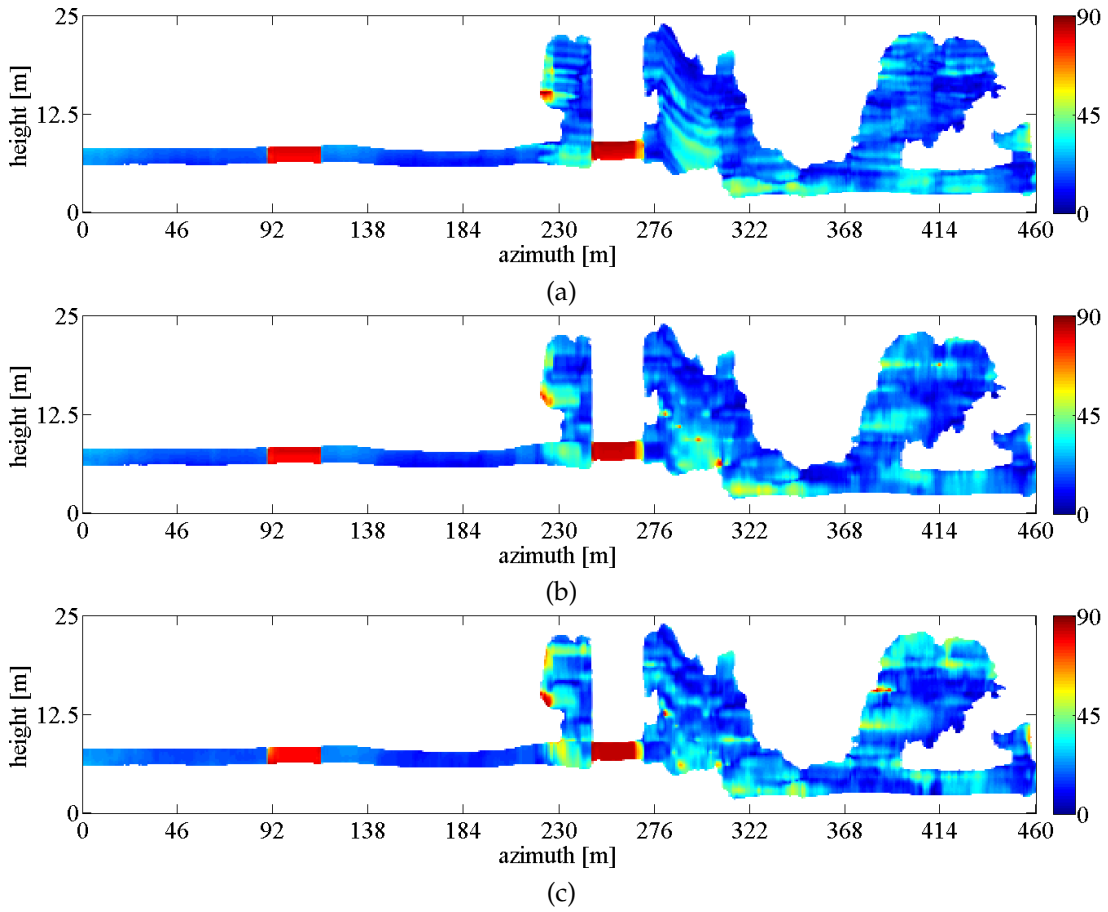

Figure 7.26: Maximum alpha angle obtained as a function of azimuth and height (460 m by 25 m) using a $20 \times 20\,\mathrm{m}^2$ window and a common mask. The slices correspond to (a) FB with 21 passes, (b) polarimetric CS with 10 passes, and (c) polarimetric CS with 6 passes. Range distance: 4272.33 m.

is expected, the polarimetric parameters derived from these five 2-D maps should be highly correlated. However, in practice, these parameters do experience small variations which are independent of possible artifacts due to tomographic processing. This is illustrated in Figure 7.28, where the reference and slave maps are compared. The green line indicates the ideal perfect correlation, while the red line has been obtained by a Least Squares (LS) fit. Figures 7.29–7.31 show, respectively, the same kind of comparison with respect to the reference track for FB with 21 passes and for CS with 10 and 6 passes. In addition, Figures 7.32 and 7.33 show a comparison with respect to FB with 21 passes for CS with 10 and 6 passes, respectively. The resulting root mean square errors (RMSEs) are reported in Figure 7.34, which should be interpreted as a *deviation* rather than an *error*.

As observed in the scattergraphs and bar charts, all tomographic inversions incur an

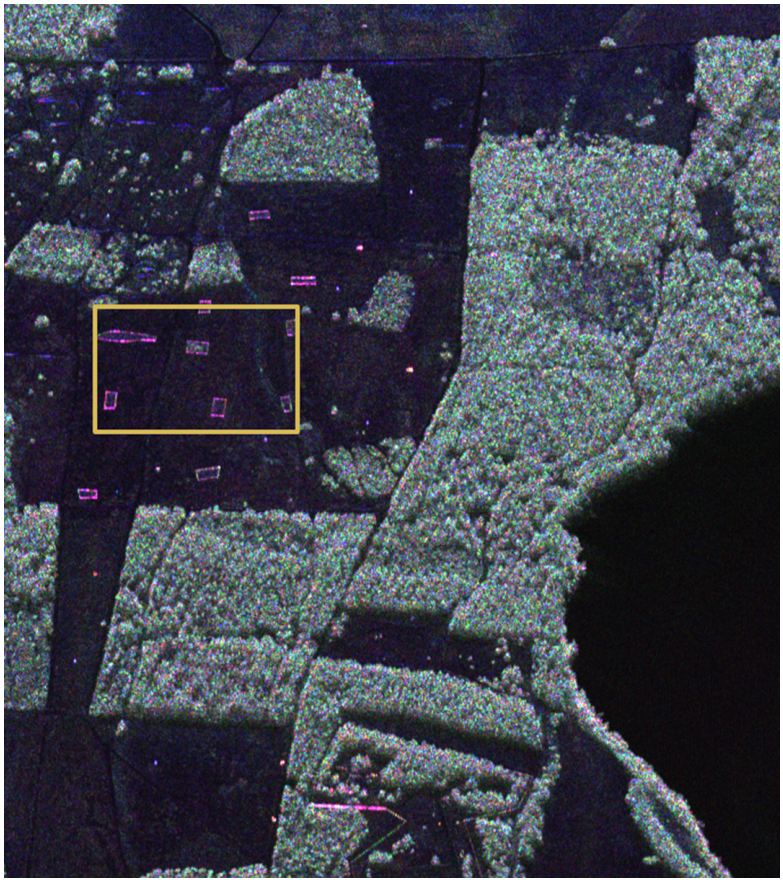

Figure 7.27: Polarimetric SAR image of the test site near Dornstetten, Germany (red: HH − VV; green: HV; blue: HH + VV). The yellow rectangle indicates a region where no volume scattering is expected.

acceptable error with respect to the reference track, which provides a pseudo-ground truth. In particular, the entropy, anisotropy, and mean and maximum alpha angle correspond, respectively, with a RMSE of less than 0.12, 0.08, $2.9°$, and $5.23°$. Similarly, the RMSE of CS with respect to FB is, respectively, of less than 0.03, 0.05, $1.09°$, and $2.23°$. Also, note that the entropy parameter tends to shift to lower values when comparing the reference track with the tomographic results [see Figures 7.29(a), 7.30(a), and 7.31(a)], which can be explained by a possible noise reduction due to the additional (multi-baseline) measurements.

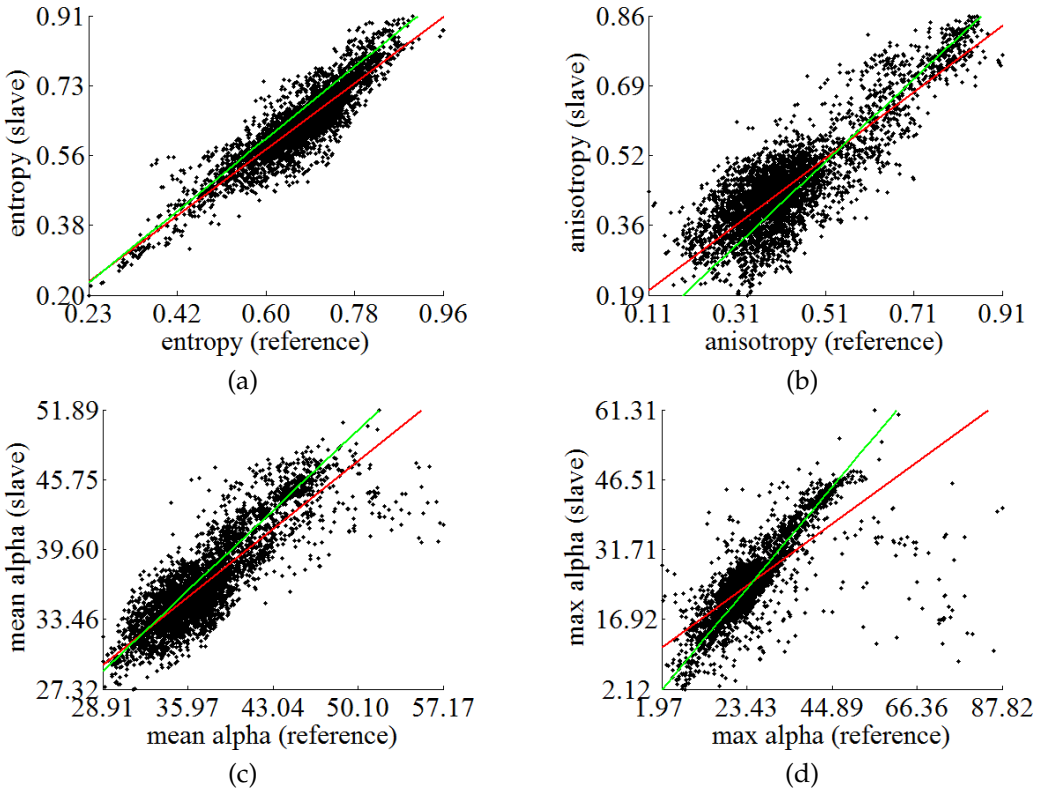

Figure 7.28: Comparison of reference image with another 100 m-baseline image (slave) in terms of entropy, anisotropy, and mean and maximum alpha angle. (Green line) Ideal correlation. (Red line) LS fit.

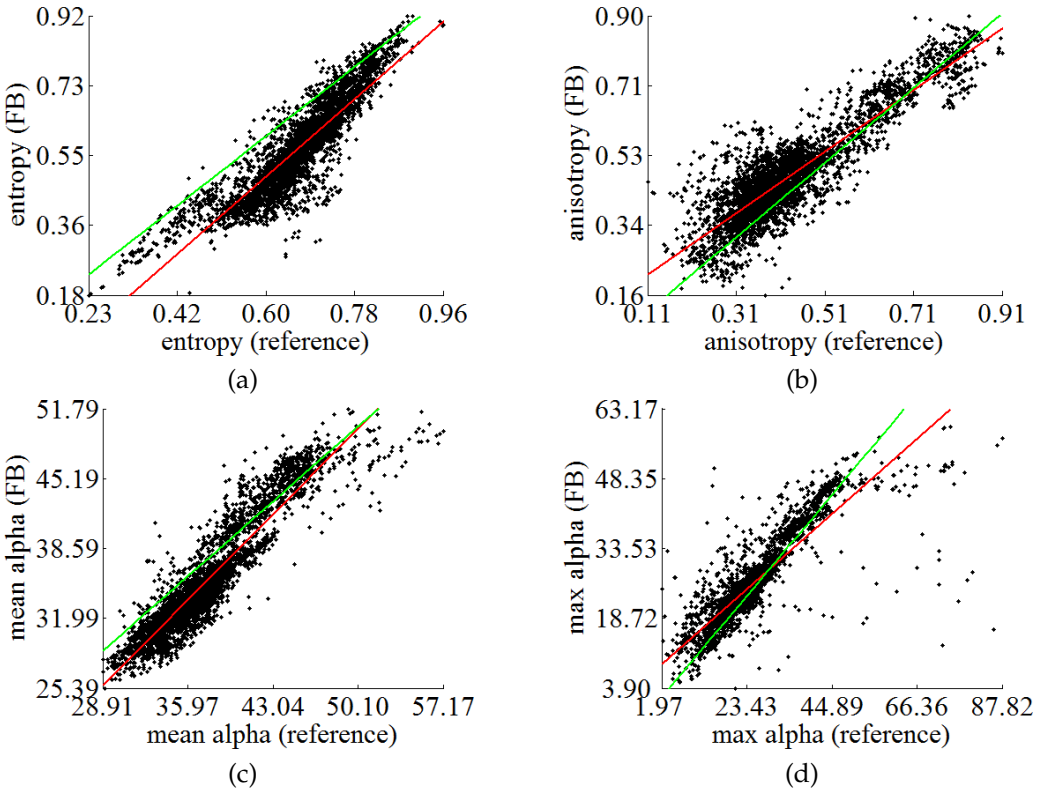

Figure 7.29: Comparison of reference image with FB layer (using 21 passes) in terms of entropy, anisotropy, and mean and maximum alpha angle. (Green line) Ideal correlation. (Red line) LS fit.

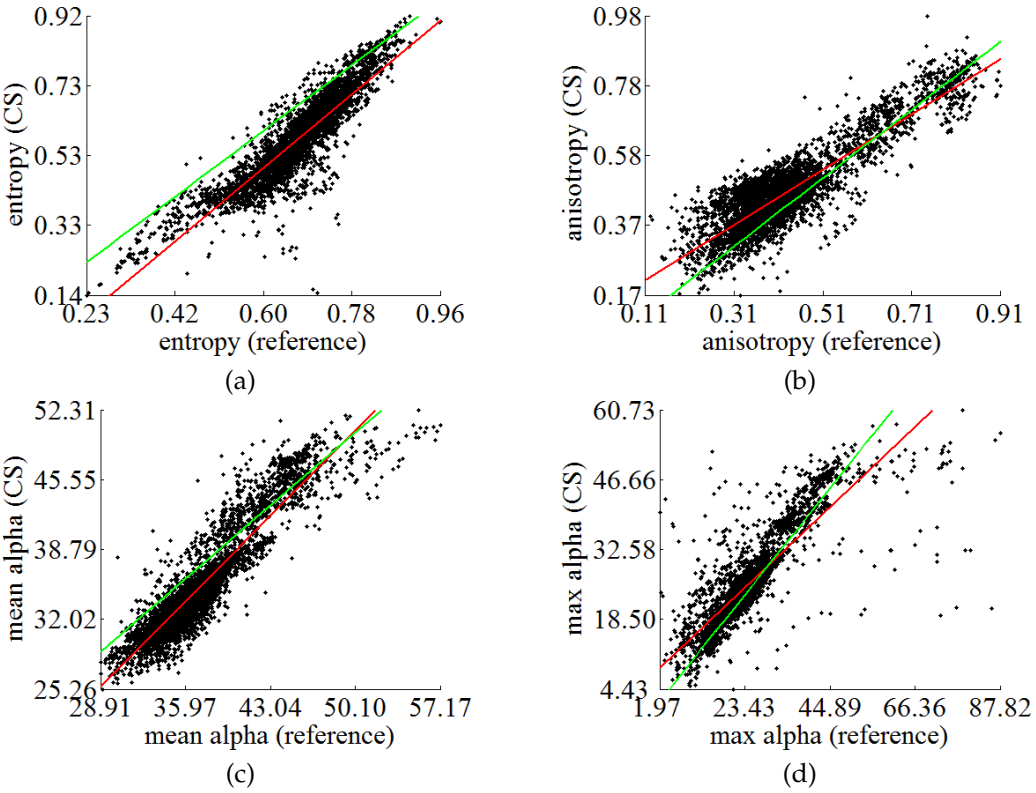

Figure 7.30: Comparison of reference image with CS layer (using 10 passes) in terms of entropy, anisotropy, and mean and maximum alpha angle. (Green line) Ideal correlation. (Red line) LS fit.

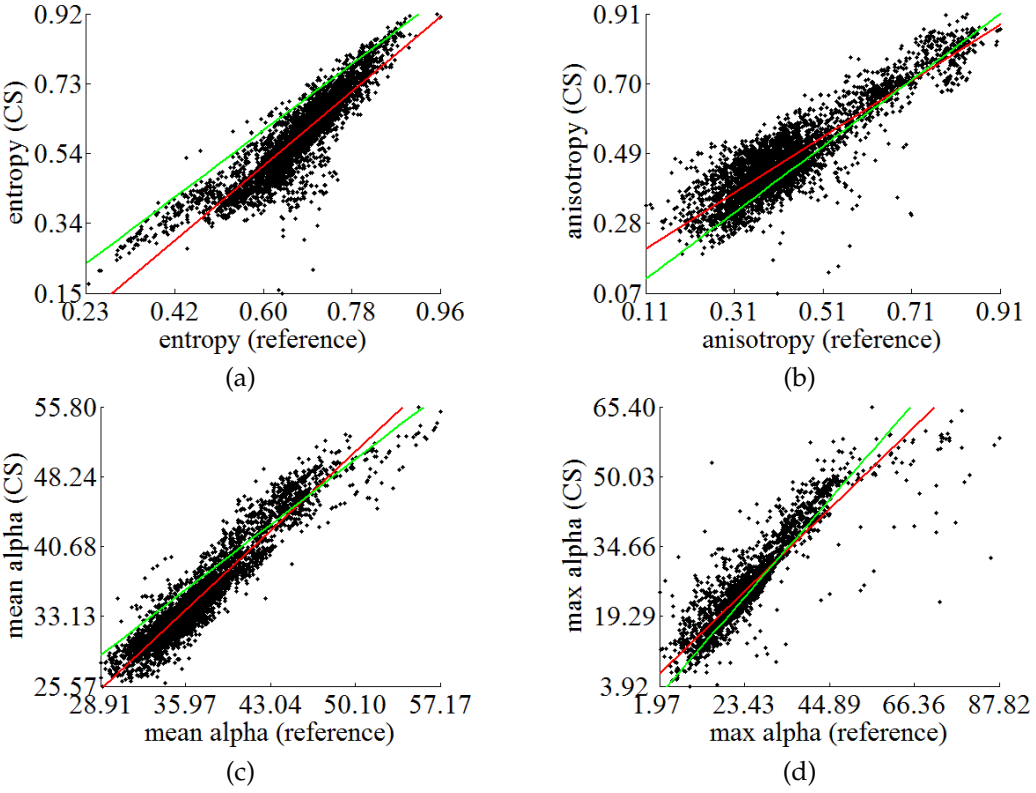

Figure 7.31: Comparison of reference image with CS layer (using 6 passes) in terms of entropy, anisotropy, and mean and maximum alpha angle. (Green line) Ideal correlation. (Red line) LS fit.

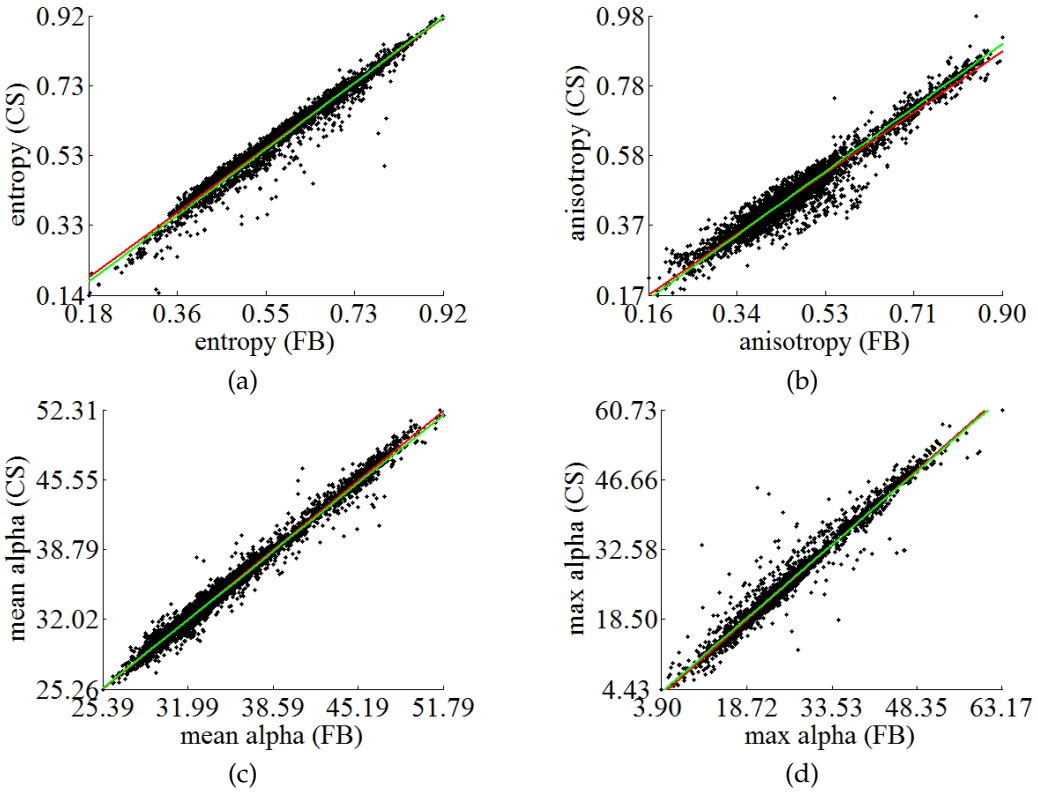

Figure 7.32: Comparison of FB layer (using 21 passes) with CS layer (using 10 passes) in terms of entropy, anisotropy, and mean and maximum alpha angle. (Green line) Ideal correlation. (Red line) LS fit.

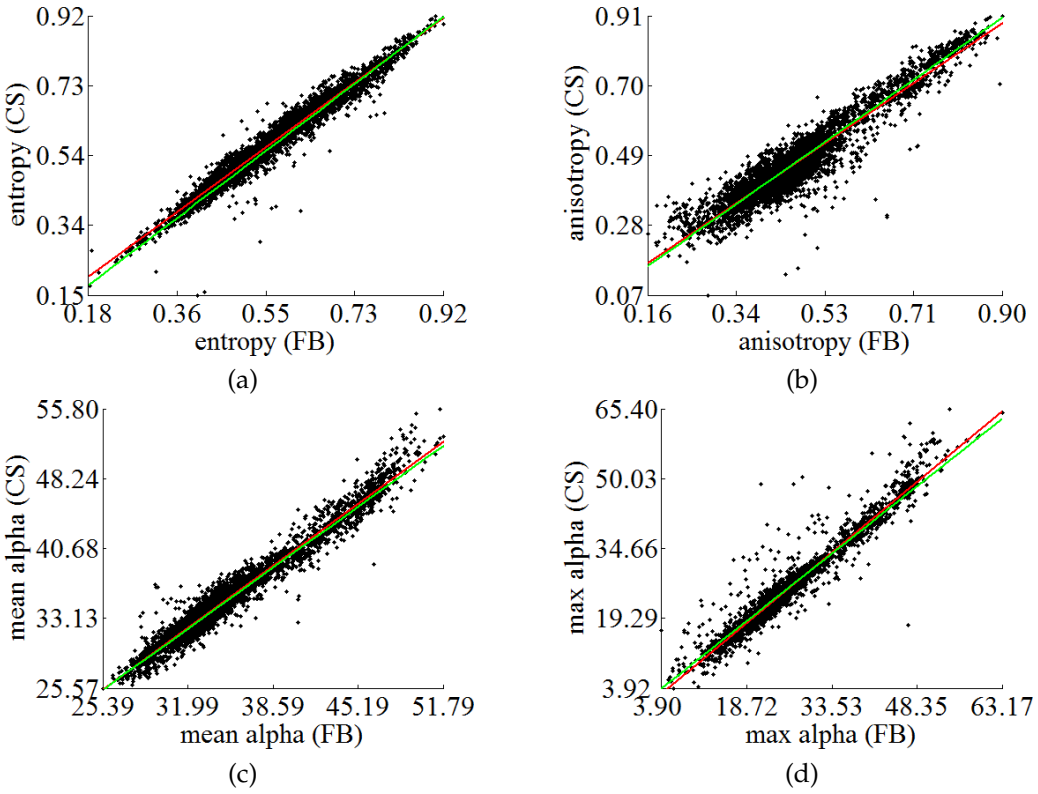

Figure 7.33: Comparison of FB layer (using 21 passes) with CS layer (using 6 passes) in terms of entropy, anisotropy, and mean and maximum alpha angle. (Green line) Ideal correlation. (Red line) LS fit.

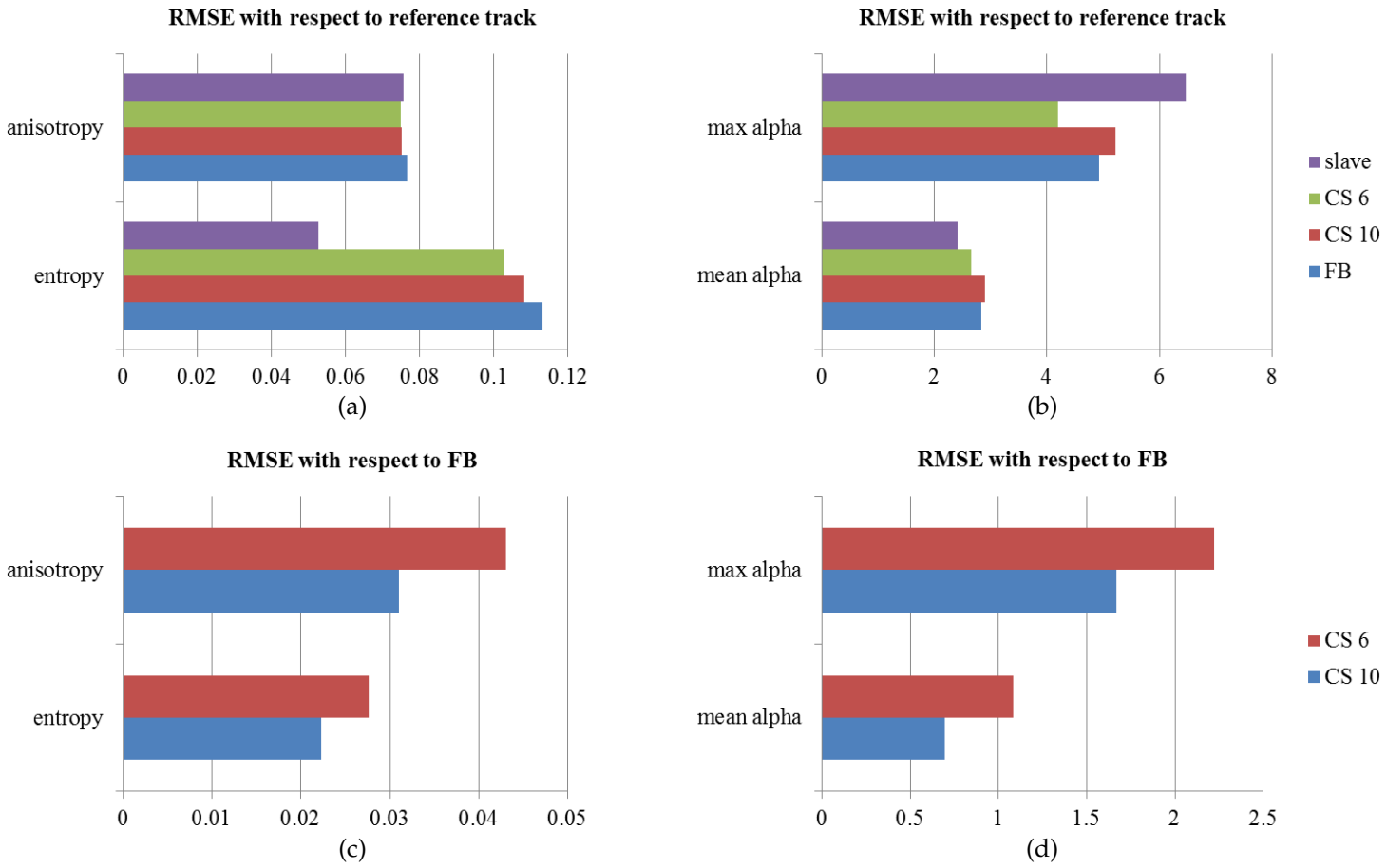

Figure 7.34: RMSE corresponding to the estimated entropy, anisotropy, and mean and maximum alpha angle using a 100 m-baseline image (slave), a FB layer with 21 passes, and CS layers with 10 and 6 passes. (Top plots) RMSE with respect to the reference track. (Bottom plots) RMSE with respect to the FB layer using 21 tracks.

Figure 7.35: Test site near Umeå, Sweden ($64^\circ\ 13'\ 57.62''$ N, $19^\circ\ 49'\ 14.21''$ E). Google.

7.2 Separation of SMs

This section verifies the optimization-based separation of SMs as given by (5.23) and (5.24). To this end, multi-baseline data acquired by the E-SAR sensor near Umeå, Sweden, in 2008 [Hajn 09], will be employed. Figures 7.35 and 7.36 show, respectively, an optical image and the amplitude of a radar image of this area. The center frequency used was 0.35 GHz (P-band) and the resulting resolutions were 1.60 m and 2.07 m in azimuth and range, respectively. The acquisition geometry corresponded to 9 parallel passes thus yielding 8 horizontal baselines of 8 m, 16 m, 24 m, 32 m, 40 m, 88 m, 184 m, and 288 m. Due to this favorable baseline distribution, CB has been chosen for tomographic analysis purposes.

First, three tomographic slices were obtained as a function of azimuth and height

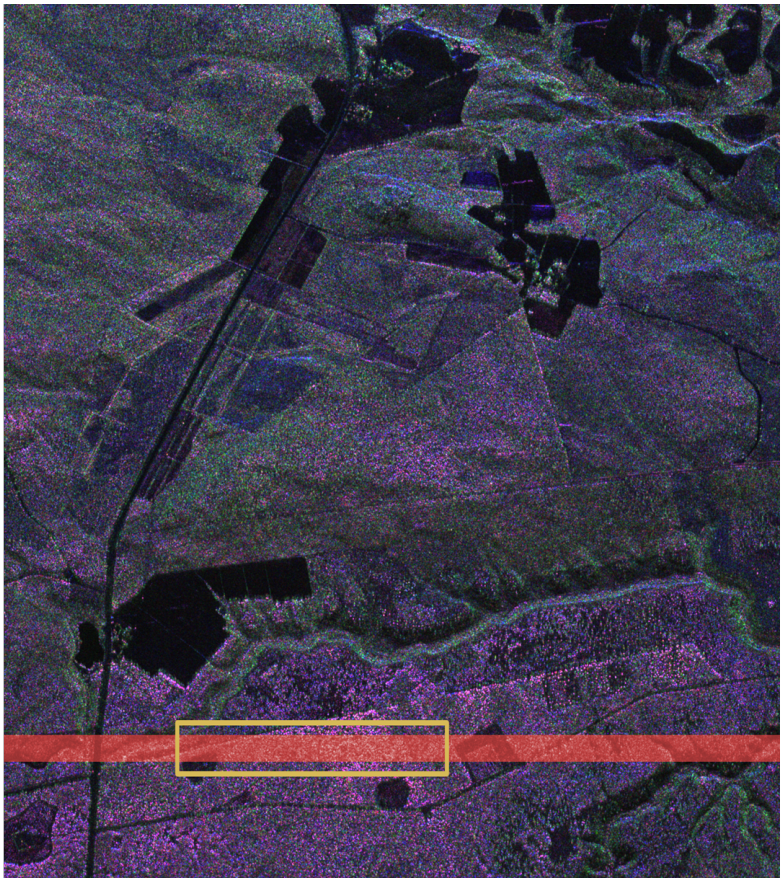

Figure 7.36: Polarimetric SAR image of the test site near Umeå, Sweden (red: HH − VV; green: HV; blue: HH + VV). The targets of interest are located within the yellow rectangle along azimuth.

(730 m by 50 m) using an estimation window of $30 \times 30\,\mathrm{m}^2$ at a range distance of 6081.97 m (see Figure 7.36). Figures 7.37(a)–(c) show the HH, VV, and HV channels, respectively. Then, the optimizations given by (5.23) and (5.24) were carried out so as to find the range of valid values for the $\dot{a}$ and $\dot{b}$ parameters. In agreement with [Teba 10c, Teba 12] the values given by $\dot{a}_{\text{max}}$ (i.e, the maximum $\dot{a}$) and $\dot{b}_{\text{min}}$ (i.e., the minimum $\dot{b}$) led to rank-deficient structure matrices, i.e., K_{G} and K_{V}, and can thus be associated with thin cross-range structures [Teba 12]. Whereas it is known that low-rank solutions are appropriate for identifying the ground SM, it is still unclear what criteria should be applied for finding the real volume SM [Teba 12]. Since this topic is outside the scope of this dissertation and a detailed treatment can be found in [Teba 12], only four possible solutions will be reported, based on four equally-spaced values for $\dot{b}$, i.e., $\dot{b}_{\text{min}} = \dot{b}_1 < \dot{b}_2 < \dot{b}_3 < \dot{b}_4 = \dot{b}_{\text{max}}$, where $\dot{b}_{\text{min}}$ and $\dot{b}_{\text{max}}$ define the interval of allowable values. Figures 7.38(a)–(d) show (in green) the CB tomographic slices corresponding to $\dot{b}_1$, $\dot{b}_2$, $\dot{b}_3$, and $\dot{b}_4$, respectively; and (in red) the CB tomograms for $\dot{a}_{\text{max}}$. Noticeably, the

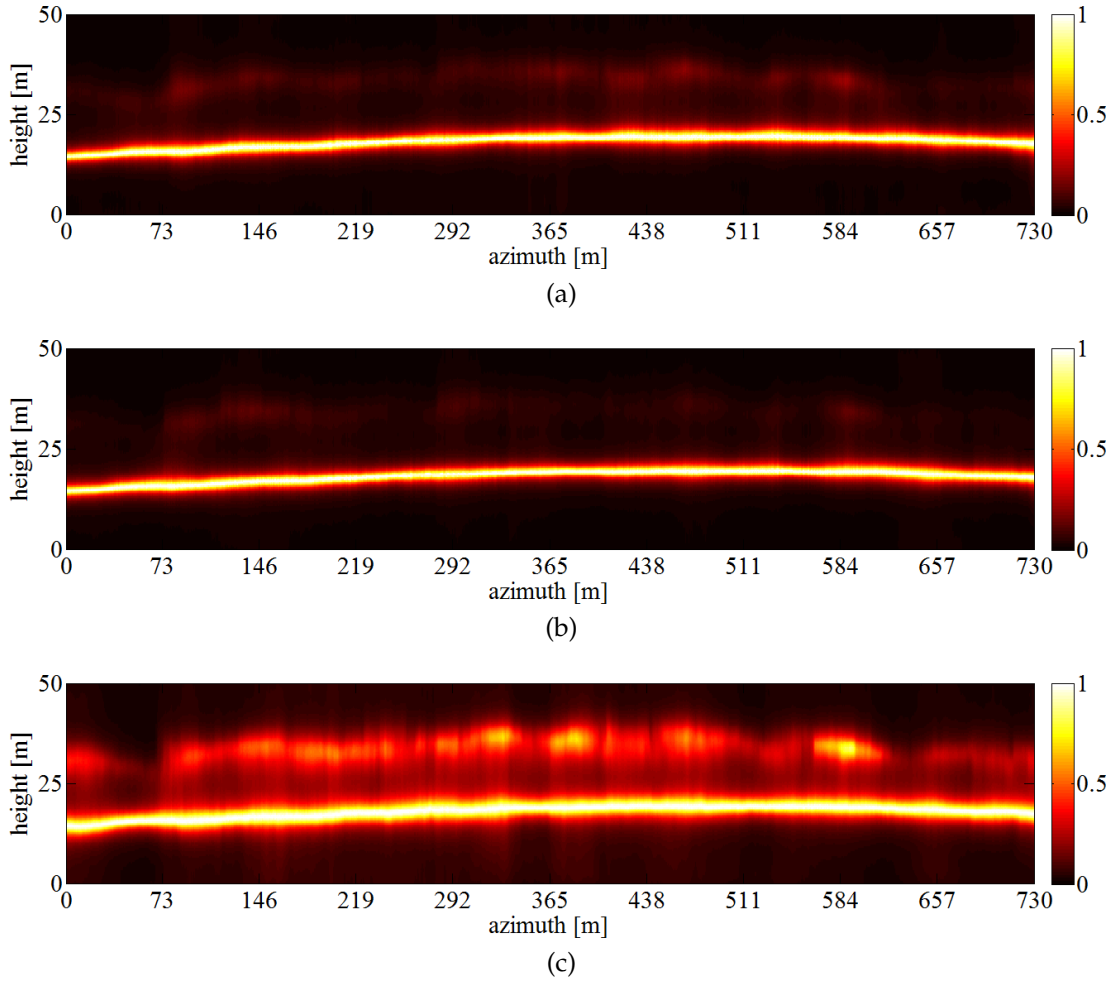

Figure 7.37: Tomographic slices (normalized at every position) obtained by CB as a function of azimuth and height (730 m by 50 m) in the (a) HH, (b) VV, and (c) HV channels. Estimation windows: $30 \times 30\,\mathrm{m}^2$. Range distance: 6081.97 m.

$(\dot{a}_{\max}, \dot{b}_1)$ (low-rank) solution pair results in two SMs that tend to exhibit disjoint support, which is consistent with the fact that the union of the supports of the two SMs should remain constant. On the contrary, higher values of $\dot{b}$ lead to larger cross-range structures where the support of the SMs intersect and thus appear in yellow. Finally, in order to reduce noise in the tomograms, a reduced-rank structure matrix has been used. The basic method proceeds as follows. First, compute the CB projection matrix H (see Section 2.4). Then, obtain the cross-range power by applying H to a low-rank approximation of the covariance matrix [Agui 12b]. Figure 7.39 presents the same SMs shown in Figure 7.38 by using the best rank-1 approximation.

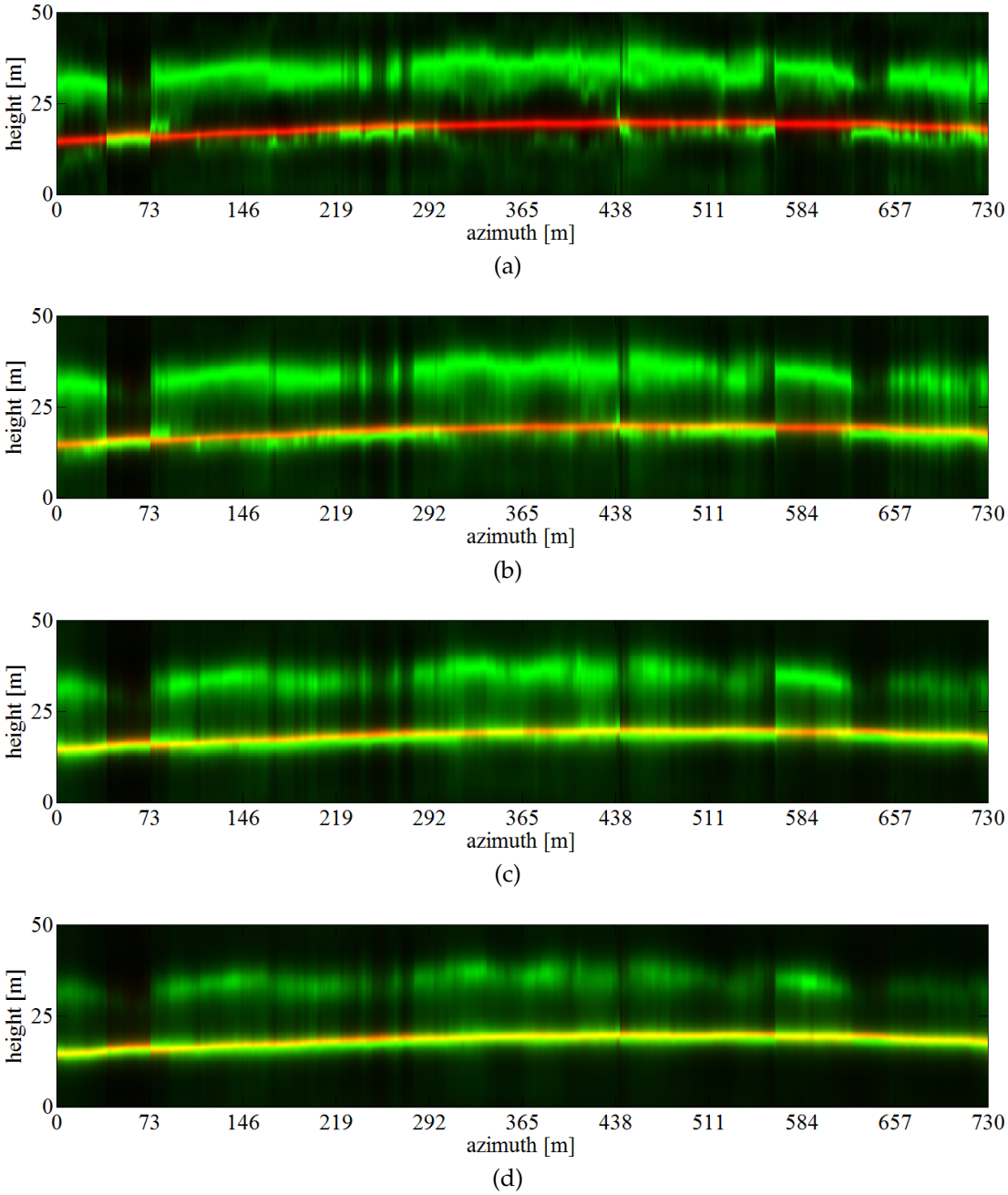

Figure 7.38: Tomographic slices of two SMs (normalized separately at every position) obtained by CB as a function of azimuth and height (730 m by 50 m) using an estimation window of 30 $\times$ 30 m^2. The $(\dot{a}, \dot{b})$ pair of parameters is given by (a) $(\dot{a}_{\max}, \dot{b}_1)$, (b) $(\dot{a}_{\max}, \dot{b}_2)$, (c) $(\dot{a}_{\max}, \dot{b}_3)$, and (d) $(\dot{a}_{\max}, \dot{b}_4)$. The ground and volume SMs are shown, respectively, in red and green. Range distance: 6081.97 m.

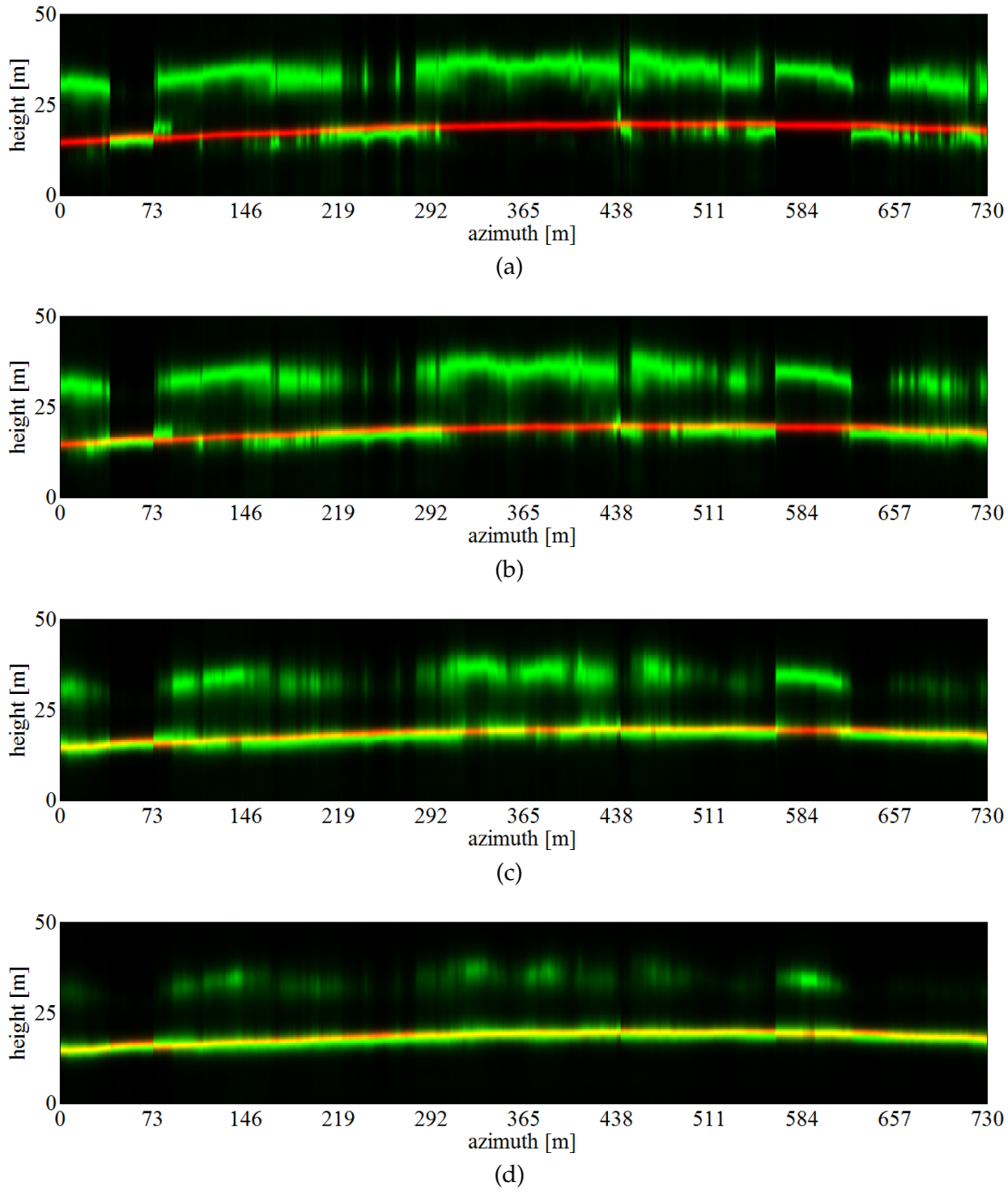

Figure 7.39: Tomographic slices of two SMs (normalized separately at every position) obtained by CB as a function of azimuth and height (730 m by 50 m) using an estimation window of $30 \times 30\,\mathrm{m}^2$ and the best rank-1 approximation of the structure matrices. The $(\dot{a}, \dot{b})$ pair of parameters is given by (a) $(\dot{a}_{\max}, \dot{b}_1)$, (b) $(\dot{a}_{\max}, \dot{b}_2)$, (c) $(\dot{a}_{\max}, \dot{b}_3)$, and (d) $(\dot{a}_{\max}, \dot{b}_4)$. The ground and volume SMs are shown, respectively, in red and green. Range distance: 6081.97 m.

8 Conclusions and Recommendations

The experimental results shown in this work, which are in line with the analysis reported in [Agui 13a, Agui 13b, Agui 13c], emphasize the ambiguity-rejection capabilities of CS as well as its ability to recover the complete cross-range backscattered power with few highly-irregular passes. A direct—and desirable—result is the increase in the height of ambiguity (see Figure 7.15). In addition, the polarimetric CS method provides high resolution while attaining physical validity (in terms of positive semidefiniteness), a property that is commonly sacrificed by most super-resolution estimators. Nevertheless, special consideration should be given to the following points:

a) It follows from the random sampling strategy outlined in Section 4.1.1 that a reduction in aliasing-like artifacts entails a nondeterministic acquisition geometry. Although such an approach might require extensive simulations prior to planning campaigns that rely on very few baselines, this downside could be alleviated by having a large tomographic aperture with a few small approximately regular baselines, in addition to few large highly-irregular ones. Nonetheless, when several passes are available, the natural deviations from the ideal tracks seem to provide (at least at L-band) the required randomness for ambiguity rejection [see, for example, Figure 7.15(a)].

b) According to the results presented in Section 7.1.1.1, large tomographic apertures with very sparse baselines can reduce the usable swath. This is due to the fact that the tomographic sampling interval [see (2.38)] intrinsically experiences higher variations at the near range [Baml 98]. Hence, this kind of sparse constellation and wide-swath airborne tomography are bound to be conflicting requirements, unless simpler models that make additional assumptions are used.

c) It is known that, for SAR tomography, the order of the RIP might fall short of ideal, even when attaining optimal coherence between the measurement basis and the

sparsity basis (see, for example, [Zhu 12]). Nonetheless, the experiments outlined in Section 7.1.1.1 (see observations *a*–*c*) indicate that this inherent limitation can be transcended (to a certain extent, depending on the number of available passes) by appropriately defining the range of heights.

d) Of equal importance is the fact that, while an adequate definition of the observation space leads to improved ambiguity-rejection capabilities, an erroneous range of heights impacts on the CS reconstruction (see observation *d* in Section 7.1.1.1). Nevertheless, this is appropriately bounded, as the backscatter corresponding to the neglected observation space can be absorbed by ε in (4.3).

e) As is clear from the previous points, an arguable case can be made that CS requires special consideration due to the fact that it inherently estimates the cross-range backscattered power simultaneously for all heights. However, note that this required *a priori* knowledge is also implicitly critical for conventional estimators, such as FB and CB, as the maximum height is an important parameter for appropriate campaign design [Nann 11].

f) Although not shown in this work, CS tomographic profiles at P-band are expected to require special consideration, as they are known to be dominated by ground-level contributions [Teba 12]. In such a case, volume backscattering might be very low with respect to the ground-level component and thus improper regularization might result in vanishing canopies. To account for this, separation of ground and volume SMs is recommended prior to carrying out CS reconstructions.

g) Since it is not always possible to conduct a multi-baseline acquisition in a short period of time, care must be taken to properly account for the possible variations (in terms of structural and electromagnetic properties) undergone by the scene (see, for example, [Lomb 98b,Lomb 12,Lomb 14]). From (4.30), (4.35), and (4.36), it is clear that the CS methodologies formulated in this work treat these variations as a simple additive perturbation. That being said, the development of more sophisticated—or simpler—CS models is recommended for future work.

h) One of the research objectives accomplished in this work was to significantly reduce the number of passes required for robust tomographic imaging. Note, however, that although CS has led to high-quality imaging (in terms of low sidelobe and ambiguity levels) with a provable upper bound on the reconstruction error [see (4.3)], operational use of CS methods should consider the corresponding estimation variance (i.e., achievable lower bounds). For examples of considerations of this kind

in the context of SAR tomography, the reader is referred to [Gini 02,Pard 08,Baml 09, Zhu 12].

i) The polarimetric extension of CS has been evaluated in terms of estimation of standard polarimetric parameters such as entropy, anisotropy, and alpha angle. While this is a reasonable validation approach, the effectiveness of polarimetric CS ought to be evaluated as a function of applications (e.g., biomass and soil moisture estimation), which is also recommended for future work.

j) Finally, note that, even though this thesis has focused on single-channel and fully-polarimetric data, all the results can be readily derived and remain valid for dual-polarized sensors.

Bibliography

[Agui 11] E. Aguilera, M. Nannini, L. Marotti, P. Prats-Iraola, and A. Reigber. "Polarimetric SAR tomography with TerraSAR-X by means of distributed compressed sensing". In: *Proceedings of ESA FRINGE Workshop*, 2011.

[Agui 12a] E. Aguilera, M. Nannini, and A. Reigber. "Multisignal compressed sensing for polarimetric SAR tomography". *IEEE Geosci. Remote Sens. Lett.*, Vol. 9, No. 5, pp. 871–875, Sep. 2012.

[Agui 12b] E. Aguilera, M. Nannini, and A. Reigber. "Wavelet-based compressed sensing for SAR tomography of forested areas". In: *Proc. EUSAR*, pp. 259–262, Apr. 2012.

[Agui 13a] E. Aguilera, M. Nannini, and A. Reigber. "A data-adaptive compressed sensing approach to polarimetric SAR tomography of forested areas". *IEEE Geosci. Remote Sens. Lett.*, Vol. 10, No. 3, pp. 543–547, May 2013.

[Agui 13b] E. Aguilera, M. Nannini, and A. Reigber. "Wavelet-based compressed sensing for polarimetric SAR tomography". In: *Proc. of POLINSAR*, 2013.

[Agui 13c] E. Aguilera, M. Nannini, and A. Reigber. "Wavelet-based compressed sensing for SAR tomography of forested areas". *IEEE Trans. Geosci. Remote Sens.*, Vol. 51, No. 12, pp. 5283–5295, Dec. 2013.

[Baml 09] R. Bamler, M. Eineder, N. Adam, X. Zhu, and S. Gernhardt. "Interferometric potential of high resolution spaceborne SAR". *Photogramm. Fernerkundung Geoinf.*, Vol. 2009, No. 5, pp. 407–419, Nov. 2009.

[Baml 92] R. Bamler. "A comparison of range-Doppler and wave-number domain SAR focusing algorithms". *IEEE Trans. Geosci. Remote Sens.*, Vol. 30, No. 4, pp. 706–713, Jul. 1992.

[Baml 98] R. Bamler and P. Hartl. "Synthetic aperture radar interferometry". *Inverse Problems*, Vol. 14, No. 4, pp. 1–54, Aug. 1998.

[Bara 07] R. Baraniuk. "Compressive sensing". *IEEE Signal Process. Mag.*, Vol. 24, pp. 118–121, Jul. 2007.

[Baro 09] D. Baron, M. Duarte, M. Waking, S. Sarvotham, and R. Baraniuk. "Distributed compressive sensing". *Preprint*, 2009.

[Beck 11] S. Becker, E. Candès, and M. Grant. "Templates for convex cone problems with applications to sparse signal recovery". *Mathematical Programming Computation*, Vol. 3, No. 3, pp. 165–218, Aug. 2011.

[Bess 00] O. Besson, F. Gini, H. Griffiths, and F. Lombardini. "Estimating ocean surface velocity and coherence time using multichannel ATI-SAR systems". In: *Proc. IEE Part-F Radar, Sonar and Navigation*, pp. 299–308, Dec. 2000.

[Bhat 08] S. Bhattacharya, T. Blumensath, B. Mulgrew, and M. Davies. "Synthetic aperture radar raw data encoding using compressed sensing". In: *Radar Conference, 2008. RADAR '08. IEEE*, pp. 1–5, May. 2008.

[Bijm 05] F. Bijma, J. de Munck, and R. Heethaar. "The spatiotemporal MEG covariance matrix modeled as a sum of Kronecker products". *NeuroImage*, Vol. 27, No. 2, pp. 402–415, 2005.

[Blon 08] V. Blondel, S. Boyd, and H. Kimura. *Recent advances in learning and control (tribute to M. Vidyasagar). Lecture Notes in Control and Information Sciences*, Springer, 2008.

[Boer 81] W. Boerner, M. El-Arini, C. Chung-Yee, and P. Mastoris. "Polarization dependence in electromagnetic inverse problems". *IEEE Trans. Antennas Propag.*, Vol. 29, No. 2, pp. 262–271, Mar. 1981.

[Boer 98] W. Boerner, H. Mott, E. Lüneburg, C. Livingstone, B. Brisco, R. Brown, and J. Paterson. *Polarimetry in radar remote sensing: basic and applied concepts*. Vol. 2 of *Manual of Remote Sensing*, Wiley, 1998.

[Borg 87] M. Borgeaud, R. Shin, and J. Kong. "Theoretical models for polarimetric radar clutter". *Journal of Electromagnetic Waves and Applications*, Vol. 1, No. 1, pp. 73–89, 1987.

[Borg 89] M. Borgeaud, S. Nghiem, R. Shin, and J. Kong. "Theoretical models for polarimetric microwave remote sensing of earth terrain". *Journal of Electromagnetic Waves and Applications*, Vol. 3, No. 1, pp. 61–68, 1989.

[Boyd 04] S. Boyd and L. Vandenberghe. *Convex optimization*. Cambridge University Press, 2004.

[Brow 69] W. Brown and R. Fredricks. "Range-doppler imaging with motion through resolution cells". *IEEE Trans. Aerosp. Electron. Syst.*, Vol. AES-5, No. 1, pp. 98–102, Jan. 1969.

[Budi 09] A. Budillon, A. Evangelista, and G. Schirinzi. "SAR tomography from sparse samples". In: *Proc. IGARSS*, pp. 865–868, Jul. 2009.

[Budi 11] A. Budillon, A. Evangelista, and G. Schirinzi. "Three-dimensional SAR focusing from multipass signals using compressive sampling". *IEEE Trans. Geosci. Remote Sens.*, Vol. 49, No. 1, pp. 488–499, Jan. 2011.

[Burr 98] C. S. Burrus, R. Gopinath, and H. Guo. *Introduction to wavelets and wavelet transforms: a primer*. Prentice-Hall, Inc., New Jersey, 1998.

[Cand 05] E. Candès and T. Tao. "Decoding by linear programming". *IEEE Trans. Inf. Theory*, Vol. 51, pp. 4203–4215, Dec. 2005.

[Cand 06a] E. Candès. "Compressive sampling". In: *Proc. Int. Congr. Math., Madrid, Spain*, pp. 1433–1452, 2006.

[Cand 06b] E. Candès, J. Romberg, and T. Tao. "Robust uncertainty principles: exact signal reconstruction from highly incomplete frequency information". *IEEE Trans. Inf. Theory*, Vol. 52, pp. 489–509, Feb. 2006.

[Cand 06c] E. Candès, J. Romberg, and T. Tao. "Stable signal recovery from incomplete and inaccurate measurements". *Communications on Pure and Applied Mathematics*, Vol. 59, pp. 1207–1223, 2006.

[Cand 06d] E. Candès and T. Tao. "Near-optimal signal recovery from random projections: universal encoding strategies?". *IEEE Trans. Inf. Theory*, Vol. 52, pp. 5406–5425, 2006.

[Cand 07] E. Candès and J. Romberg. "Sparsity and incoherence in compressive sampling". *Inverse Problems*, Vol. 23, pp. 969–985, 2007.

[Cand 08] E. Candès. "The restricted isometry property and its implications for compressed sensing". *Comptes Rendus Mathematique*, Vol. 346, pp. 589–592, 2008.

[Capo 69] J. Capon. "High-resolution frequency-wavenumber spectrum analysis". *Proceedings of the IEEE*, Vol. 57, No. 8, pp. 1408–1418, 1969.

[Clou 06] S. Cloude. "Polarization coherence tomography". *Radio Science*, Vol. 41, 2006.

[Clou 10] S. Cloude. *Polarisation: applications in remote sensing*. OUP Oxford, 2010.

[Clou 86] S. Cloude. *Polarimetry: the characterization of polarimetric effects in EM scattering*. PhD thesis, University of Birmingham, Jul. 1986.

[Clou 92] S. Cloude. "Uniqueness of target decomposition theorems in radar polarimetry". In: *Direct and inverse methods in radar polarimetry*, pp. 267–296, Springer Netherlands, 1992.

[Clou 96] S. Cloude and E. Pottier. "A review of target decomposition theorems in radar polarimetry". *IEEE Trans. Geosci. Remote Sens.*, Vol. 34, No. 2, pp. 498–518, Mar. 1996.

[Clou 97] S. Cloude. "An entropy based classification scheme for land applications of polarimetric SAR". *IEEE Trans. Geosci. Remote Sens.*, Vol. 35, No. 1, pp. 68–78, Jan. 1997.

[Cors 99] G. Corsini, M. Diani, F. Lombardini, and G. Pinelli. "Simulated analysis and optimization of a three-antenna airborne InSAR system for topographic mapping". *IEEE Trans. Geosci. Remote Sens.*, Vol. 37, No. 5, pp. 2518–2529, Sep. 1999.

[Cumm 05] I. G. Cumming and F. H. Wong. *Digital processing of synthetic aperture radar data: algorithms and implementation*. Artech House, 2005.

[Curl 91] J. Curlander and R. N. McDonough. *Synthetic aperture radar: systems and signal processing*. Wiley, 1991.

[dAle 12] M. M. d'Alessandro and S. Tebaldini. "Phenomenology of P-Band scattering from a tropical forest through three-dimensional SAR tomography". *IEEE Geosci. Remote Sens. Lett.*, Vol. 9, No. 3, pp. 442–446, May. 2012.

[Daub 88] I. Daubechies. "Orthonormal bases of compactly supported wavelets". *Communications on Pure and Applied Mathematics*, Vol. 41, No. 7, pp. 909–996, Oct. 1988.

[Daub 92] I. Daubechies. *Ten lectures on wavelets*. Society for Industrial and Applied Mathematics (SIAM, 3600 Market Street, Floor 6, Philadelphia, PA 19104), 1992.

[Dono 06] D. Donoho. "Compressed sensing". *IEEE Trans. Inf. Theory*, Vol. 52, pp. 1289–1306, Apr. 2006.

[Dono 10] D. Donoho and J. Tanner. "Counting the faces of randomly-projected hypercubes and orthants, with applications". *Discrete and Computational Geometry*, Vol. 43, pp. 522–541, 2010.

[Duar 12] M. Duarte and R. Baraniuk. "Kronecker compressive sensing". *IEEE Trans. Image Process.*, Vol. 21, No. 2, pp. 494–504, Feb. 2012.

[Elac 06] C. Elachi and J. van Zyl. *Introduction to the physics and techniques of remote sensing*. Wiley, 2006.

[Elda 09] Y. Eldar and M. Mishali. "Robust recovery of signals from a structured union of subspaces". *IEEE Trans. Inf. Theory*, Vol. 55, pp. 5302–5316, 2009.

[Elda 10] Y. Eldar and H. Rauhut. "Average case analysis of multichannel sparse recovery using convex relaxation". *IEEE Trans. Inf. Theory*, Vol. 56, pp. 505–519, Jan. 2010.

[Forn 03] G. Fornaro, F. Serafino, and F. Soldovieri. "Three-dimensional focusing with multipass SAR data". *IEEE Trans. Geosci. Remote Sens.*, Vol. 41, No. 3, pp. 507–517, Mar. 2003.

[Forn 11] M. Fornasier and H. Rauhut. "Compressive sensing". In: O. Scherzer, Ed., *Handbook of mathematical methods in imaging*, pp. 187–228, Springer New York, 2011.

[Frey 08] O. Frey, F. Morsdorf, and E. Meier. "Tomographic imaging of a forested area by airborne multi-baseline P-band SAR". *Sensors*, Vol. 8, No. 9, pp. 5884–5896, Sep. 2008.

[Frey 11a] O. Frey and E. Meier. "3-D time-domain SAR imaging of a forest using airborne multibaseline data at L- and P-Bands". *IEEE Trans. Geosci. Remote Sens.*, Vol. 49, No. 10, pp. 3660–3664, Oct. 2011.

[Frey 11b] O. Frey and E. Meier. "Analyzing tomographic SAR data of a forest with respect to frequency, polarization, and focusing technique". *IEEE Trans. Geosci. Remote Sens.*, Vol. 49, No. 10, pp. 3648–3659, Oct. 2011.

[Gini 02] F. Gini, F. Lombardini, and M. Montanari. "Layover solution in multibaseline SAR interferometry". *IEEE Trans. Aerosp. Electron. Syst.*, Vol. 38, No. 4, pp. 1344–1356, Oct. 2002.

[Gran 13] M. Grant and S. Boyd. "CVX: Matlab software for disciplined convex programming". 2013. http://cvxr.com/cvx.

[Guil 05] S. Guillaso and A. Reigber. "Polarimetric SAR tomography". In: *Proc. of POLINSAR*, Jan. 2005.

[Hajn 09] I. Hajnsek, R. Scheiber, M. Keller, R. Horn, S. Lee, L. Ulander, A. Gustavsson, G. Sandberg, T. Le Toan, S. Tebaldini, A. Monti Guarnieri, and F. Rocca. "BIOSAR 2008: final report". Tech. Rep. 22052/08/NL/CT, European Space Agency, 2009.

[Hans 01] R. Hanssen. *Radar interferometry: data interpretation and error analysis*. Springer, 2001.

[Home 96] J. Homer, I. Longstaff, and G. Callaghan. "High resolution 3-D SAR via multi-baseline interferometry". In: *Proc. IGARSS*, pp. 796–798, May 1996.

[Huan 12] Y. Huang, L. Ferro-Famil, and A. Reigber. "Under-foliage object imaging using SAR tomography and polarimetric spectral estimators". *IEEE Trans. Geosci. Remote Sens.*, Vol. 50, No. 6, pp. 2213–2225, Jun. 2012.

[Huyg 90] C. Huygens. "Traité de la lumiére". 1690.

[Jagd 13] T. Jagdhuber, I. Hajnsek, A. Bronstert, and K. Papathanassiou. "Soil moisture estimation under low vegetation cover using a multi-angular polarimetric decomposition". *IEEE Trans. Geosci. Remote Sens.*, Vol. 51, No. 4, pp. 2201–2215, Apr. 2013.

[Jako 05] A. Jakobsson, F. Gini, and F. Lombardini. "Robust estimation of radar reflectivities in multibaseline InSAR". *IEEE Trans. Aerosp. Electron. Syst.*, Vol. 41, No. 2, pp. 751–758, Apr. 2005.

[Klau 60] J. Klauder, A. Price, S. Darlington, and W. Albersheim. "The theory and design of chirp radars". *The Bell System Technical Journal*, Vol. 39, No. 4, pp. 745–808, Jul. 1960.

[Kost 86] A. Kostinski and W. Boerner. "On foundations of radar polarimetry". *IEEE Trans. Antennas Propag.*, Vol. 34, No. 12, pp. 1395–1404, Dec. 1986.

[Krog 90] E. Krogager. "New decomposition of the radar target scattering matrix". *Electronics Letters*, Vol. 26, No. 18, pp. 1525–1527, Aug. 1990.

[Lee 09] J. S. Lee and E. Pottier. *Polarimetric radar imaging: from basics to applications*. *Optical Science and Engineering*, Taylor & Francis, 2009.

[Leit 73] E. Leith. "Range-azimuth-coupling aberrations in pulse-scanned imaging systems". *Journal of The Optical Society of America*, Vol. 63, No. 2, pp. 119–126, 1973.

[Libe 06] L. Liberti and N. Maculan. *Global optimization: from theory to implementation*. *Nonconvex Optimization and Its Applications*, Springer, 2006.

[Line 93] D. Linebarger, I. Sudborough, and I. Tollis. "Difference bases and sparse sensor arrays". *IEEE Trans. Inf. Theory*, Vol. 39, No. 2, pp. 716–721, Mar. 1993.

[Lomb 03] F. Lombardini and A. Reigber. "Adaptive spectral estimation for multibaseline SAR tomography with airborne L-band data". In: *Proc. IGARSS*, pp. 2014–2016, Jul. 2003.

[Lomb 08a] F. Lombardini and M. Pardini. "3-D SAR tomography: the multibaseline sector interpolation approach". *IEEE Geosci. Remote Sens. Lett.*, Vol. 5, No. 4, pp. 630–634, Oct. 2008.

[Lomb 08b] F. Lombardini and M. Pardini. "Sector matched interpolation for 3D SAR correlative interferometric imaging". Tech. Rep. Edizioni ETS, University of Pisa, Jul. 2008.

[Lomb 09a] F. Lombardini and M. Pardini. "Experiments of tomography-based SAR techniques with P-band polarimetric data". In: *Proc. of POLINSAR*, Jan. 2009.

[Lomb 09b] F. Lombardini, M. Pardini, G. Fornaro, F. Serafino, L. Verrazzani, and M. Costantini. "Linear and adaptive spaceborne three-dimensional SAR tomography: a comparison on real data". *IET Radar, Sonar & Navigation*, Vol. 3, No. 4, pp. 424–436, Jun. 2009.

[Lomb 12] F. Lombardini and M. Pardini. "Superresolution differential tomography: experiments on identification of multiple scatterers in spaceborne SAR data". *IEEE Trans. Geosci. Remote Sens.*, Vol. 50, No. 4, pp. 1117–1129, Apr. 2012.

[Lomb 13] F. Lombardini, F. Cai, and D. Pasculli. "Spaceborne 3-D SAR tomography for analyzing garbled urban scenarios: single-look superresolution advances and experiments". *IEEE J. Sel. Topics Appl. Earth Observ.*, Vol. 6, No. 2, pp. 960–968, Apr. 2013.

[Lomb 14] F. Lombardini and F. Cai. "Temporal decorrelation-robust SAR tomography". *IEEE Trans. Geosci. Remote Sens.*, Vol. 52, No. 9, pp. 5412–5421, Sep. 2014.

[Lomb 98a] F. Lombardini. "Optimum absolute phase retrieval in three-element SAR interferometer". *Electronics Letters*, Vol. 34, No. 15, pp. 1522–1524, Jul. 1998.

[Lomb 98b] F. Lombardini and H. Griffiths. "Effect of temporal decorrelation on 3D SAR imaging using multiple pass beamforming". In: *Proc. IEE-EUREL Meeting on Radar and Sonar Signal Processing*, pp. 34/1–34/4, Jul. 1998.

[Lore 05] R. Lorenz and S. Boyd. "Robust minimum variance beamforming". *IEEE Trans. Signal Process.*, Vol. 53, No. 5, pp. 1684–1696, May 2005.

[Lori 07] I. Loris, G. Nolet, I. Daubechies, and F. Dahlen. "Tomographic inversion using L1-norm regularization of wavelet coefficients". *Geophysical Journal of The Royal Astronomical Society*, Vol. 170, pp. 359–370, 2007.

[Lust 07] M. Lustig, D. Donoho, and J. Pauly. "Sparse MRI: the application of compressed sensing for rapid MR imaging". *Magnetic Resonance in Medicine*, Vol. 58, pp. 1182–1195, Dec. 2007.

[Mall 09] S. Mallat. *A wavelet tour of signal processing*. Academic Press, Burlington, 2009.

[Merc 09] J. Mercer. "Functions of positive and negative type, and their connection with the theory of integral equations". *Proceedings of The Royal Society A: Mathematical, Physical and Engineering Sciences*, Vol. 83, pp. 69–70, 1909.

[More 11] A. Moreira, G. Krieger, M. Younis, I. Hajnsek, K. Papathanassiou, M. Eineder, and F. De Zan. "Tandem-L: a mission proposal for monitoring dynamic earth processes". In: *Proc. IGARSS*, pp. 1385–1388, 2011.

[More 13] A. Moreira, P. Prats-Iraola, M. Younis, G. Krieger, I. Hajnsek, and K. Papathanassiou. "A tutorial on synthetic aperture radar". *IEEE Geosci. Remote Sens. Mag.*, Vol. 1, No. 1, pp. 6–43, 2013.

[Nann 07] M. Nannini and R. Scheiber. "Height dependent motion compensation and coregistration for airborne SAR tomography". In: *Proc. IGARSS*, pp. 5041–5044, Jul. 2007.

[Nann 09] M. Nannini, R. Scheiber, and A.Moreira. "Estimation of the minimum number of tracks for SAR tomography". *IEEE Trans. Geosci. Remote Sens.*, Vol. 47, pp. 531–543, Feb. 2009.

[Nann 10] M. Nannini, A. Reigber, and R. Scheiber. "A study on irregular baseline constellations in SAR tomography". In: *Proc. EUSAR*, pp. 1–4, Jun. 2010.

[Nann 11] M. Nannini, R. Scheiber, R. Horn, and A.Moreira. "First 3-D reconstructions of targets hidden beneath foliage by means of polarimetric SAR tomography". *IEEE Geosci. Remote Sens. Lett.*, Vol. PP, No. 99, pp. 1–5, Jul. 2011.

[Papa 01] K. Papathanassiou and S. Cloude. "Single-baseline polarimetric SAR interferometry". *IEEE Trans. Geosci. Remote Sens.*, Vol. 39, No. 11, pp. 2352–2363, Nov. 2001.

[Pard 08] M. Pardini, F. Lombardini, and F. Gini. "The hybrid Cramér-Rao bound on broadside DOA estimation of extended sources in presence of array errors". *IEEE Trans. Signal Process.*, Vol. 56, No. 4, pp. 1726–1730, Apr. 2008.

[Pasq 95] P. Pasquali, C. Prati, F. Rocca, M. Seymour, J. Fortuny, E. Ohlmer, and A. Sieber. "A 3-D SAR experiment with EMSL data". In: *Proc. IGARSS*, pp. 784–786, Jul. 1995.

[Pott 10] L. Potter, E. Ertin, J. Parker, and M. Çetin. "Sparsity and compressed sensing in radar imaging". *Proceedings of the IEEE*, Vol. 98, No. 6, pp. 1006–1020, Jun. 2010.

[Reig 00] A. Reigber and A. Moreira. "First demonstration of airborne SAR tomography using multibaseline L-band data". *IEEE Trans. Geosci. Remote Sens.*, Vol. 38, No. 5, pp. 2142–4152, Sep. 2000.

[Reig 13] A. Reigber, R. Scheiber, M. Jager, P. Prats-Iraola, I. Hajnsek, T. Jagdhuber, K. Papathanassiou, M. Nannini, E. Aguilera, S. Baumgartner, R. Horn, A. Nottensteiner, and A. Moreira. "Very-high-resolution airborne synthetic aperture radar imaging: signal processing and applications". *Proceedings of the IEEE*, Vol. 101, No. 3, pp. 759–783, Mar. 2013.

[Rude 08] M. Rudelson and R. Vershynin. "On sparse reconstruction from Fourier and Gaussian measurements". *Communications on Pure and Applied Mathematics*, Vol. 61, pp. 1025–1045, 2008.

[Sama 09] S. Samadi, M. Çetin, and M. Masnadi-Shirazi. "Multiple feature-enhanced synthetic aperture radar imaging". In: *SPIE Defense and Security Symposium, Algorithms for Synthetic Aperture Radar Imagery XVI*, pp. 1–10, Apr. 2009.

[Saue 11] S. Sauer, L. Ferro-Famil, A. Reigber, and E. Pottier. "Three-dimensional imaging and scattering mechanism estimation over urban scenes using dual-baseline polarimetric InSAR observations at L-band". *IEEE Trans. Geosci. Remote Sens.*, Vol. 49, No. 11, pp. 4616–4629, Jun. 2011.

[Schm 13] M. Schmitt and U. Stilla. "Compressive sensing based layover separation in airborne single-pass multi-baseline InSAR data". *IEEE Geosci. Remote Sens. Lett.*, Vol. 10, No. 2, pp. 313–317, 2013.

[Stoi 02] P. Stoica, Z. Wang, and J. Li. "Robust Capon beamforming". In: *Conference Record of the Thirty-Sixth Asilomar Conference on Signals, Systems and Computers, 2002*, pp. 876–880, 2002.

[Stoi 97] P. Stoica and R. Moses. *Introduction to spectral analysis*. Prentice Hall Upper Saddle River, NJ, 1997.

[Teba 09] S. Tebaldini. "Algebraic synthesis of forest scenarios from multibaseline PolInSAR data". *IEEE Trans. Geosci. Remote Sens.*, Vol. 47, No. 12, pp. 4132–4142, Dec. 2009.

[Teba 10a] S. Tebaldini. "Single and multipolarimetric SAR tomography of forested areas: a parametric approach". *IEEE Trans. Geosci. Remote Sens.*, Vol. 48, No. 5, pp. 2375–2387, May. 2010.

[Teba 10b] S. Tebaldini and A. M. Guarnieri. "On the role of phase stability in SAR multibaseline applications". *IEEE Trans. Geosci. Remote Sens.*, Vol. 48, pp. 2953–2966, Jul. 2010.

[Teba 10c] S. Tebaldini, M. M. d'Alessandro, A. Monti Guarnieri, and F. Rocca. "Polarimetric and structural properties of forest scenarios as imaged by longer wavelength SARs". In: *Proc. EUSAR*, pp. 3251–3254, Jul. 2010.

[Teba 12] S. Tebaldini and F. Rocca. "Multibaseline polarimetric SAR tomography of a boreal forest at P- and L-bands". *IEEE Trans. Geosci. Remote Sens.*, Vol. 50, No. 1, pp. 232–246, Jan. 2012.

[Tibs 05] R. Tibshirani, M. Saunders, S. Rosset, J. Zhu, and K. Knight. "Sparsity and smoothness via the fused lasso". *Journal of The Royal Statistical Society Series B-statistical Methodology*, Vol. 67, pp. 91–108, 2005.

[Toan 11] T. L. Toan, S. Quegan, M. Davidson, H. Balzter, P. Paillou, K. Papathanassiou, S. Plummer, F. Rocca, S. Saatchi, H. Shugart, and L. Ulander. "The BIOMASS mission: mapping global forest biomass to better understand the terrestrial carbon cycle". *Remote Sensing of Environment*, Vol. 115, No. 11, pp. 2850–2860, 2011.

[Treu 02] R. Treuhaft, G. Asner, B. Law, and S. van Tuyl. "Forest leaf area density profiles from the quantitative fusion of radar and hyperspectral data". *J. Geophys. Res.*, Vol. 107, pp. 4568–4580, 2002.

[Wood 06] I. Woodhouse. *Introduction to microwave remote sensing*. Taylor & Francis, 2006.

[Wu 11] J. Wu, F. Liu, L. Jiao, and X. Wang. "Compressive sensing SAR image reconstruction based on Bayesian framework and evolutionary computation". *IEEE Trans. Image Process.*, Vol. 20, No. 7, pp. 1904–1911, Jul. 2011.

[Yang 10] J. Yang, Y. Zhang, and W. Yin. "A fast alternating direction method for TVL1-L2 signal reconstruction from partial Fourier data". *IEEE J. Sel. Topics Signal Process.*, Vol. 4, No. 2, pp. 288–297, Apr. 2010.

[Zebk 92] H. Zebker and J. Villasenor. "Decorrelation in interferometric radar echoes". *IEEE Transactions on Geoscience and*, Vol. 30, No. 5, pp. 950–959, 1992.

[Zhu 10a] X. Zhu and R. Bamler. "Tomographic SAR inversion by L1-norm regularization – the compressive sensing approach". *IEEE Trans. Geosci. Remote Sens.*, Vol. 48, pp. 3839–3846, Oct. 2010.

[Zhu 10b] X. Zhu and R. Bamler. "Very high resolution spaceborne SAR tomography in urban environment". *IEEE Trans. Geosci. Remote Sens.*, Vol. 48, No. 12, pp. 4296–4308, Dec. 2010.

[Zhu 12] X. Zhu and R. Bamler. "Super-resolution power and robustness of compressive sensing for spectral estimation with application to spaceborne tomographic SAR". *IEEE Trans. Geosci. Remote Sens.*, Vol. 50, No. 1, pp. 247–258, Jan. 2012.